DUDLEY KNOX LIBRARY
NAVAL POSTGRADUATE SCHOOL
MONTEREY CA 93943-5101

Unclassified

Security Classification of this page

REPORT DOCUMENTATION PAGE

1a Report Security Classification Unclassified

1b Restrictive Markings

2a Security Classification Authority

2b Declassification/Downgrading Schedule

3 Distribution Availability of Report
Approved for public release; distribution is unlimited.

4 Performing Organization Report Number(s)

5 Monitoring Organization Report Number(s)

6a Name of Performing Organization
Naval Postgraduate School

6b Office Symbol *(If Applicable)* 39

6c Address *(city, state, and ZIP code)*
Monterey, CA 93943-5000

7a Name of Monitoring Organization
Naval Postgraduate School

7b Address *(city, state, and ZIP code)*
Monterey, CA 93943-5000

8a Name of Funding/Sponsoring Organization

8b Office Symbol *(If Applicable)*

8c Address *(city, state, and ZIP code)*

9 Procurement Instrument Identification Number

10 Source of Funding Numbers

Program Element Number	Project No	Task No	Work Unit Accession No

11 Title *(Include Security Classification)* EXPERIMENTAL VERIFICATION OF ATTITUDE CONTROL TECHNIQUES FOR FLEXIBLE SPACECRAFT SLEW MANEUVERS

12 Personal Author(s) Jeffrey A. Hailey

13a Type of Report
Engineer's Thesis

13b Time Covered
From To

14 Date of Report *(year, month,day)*
March 1992

15 Page Count
123

16 Supplementary Notation The views expressed in this thesis are those of the author and do not reflect the official policy or position of the Department of Defense or the U.S. Government.

17 Cosati Codes

Field	Group	Subgroup

18 Subject Terms *(continue on reverse if necessary and identify by block number)*
Attitude Control; Flexible Spacecraft; Experimental Verification

19 Abstract *(continue on reverse if necessary and identify by block number*

The experimental verification of attitude control designs for flexible spacecraft is essential for reliable operation in space. The Flexible Spacecraft Simulator (FSS) at the Naval Postgraduate School is designed to test a variety of control designs. The experimental setup simulates pitch axis motion of a flexible spacecraft consisting of a rigid central body and a flexible appendage connecting a reflector. The primary actuators are a reaction wheel and thrusters. Position information is obtained with a rotary variable differential transformer (RVDT) and rate information is obtained by a solid state rate sensor. Two analytical models are derived; one based on cantilever modes, the other based on system modes. Both are a result of linearized equations of motion which assume small flexible deflections and rates. Slew maneuvers are conducted using four separate controllers. They are proportional-derivative (PD), torque profiles, bang-bang and optimal controllers. Techniques for state estimation are explored for the optimal controller since the standard estimation methods prove to be unsatisfactory. The sinusoidal torque profile delivers the best performance overall with the PD a close second. Momentum wheel desaturation with thrusters and thruster slew maneuvers are also performed. In all cases, experimental results are in close agreement with analytical predictions.

20 Distribution/Availability of Abstract
☒ unclassified/unlimited ☐ same as report ☐ DTIC users

21 Abstract Security Classification
Unclassified

22a Name of Responsible Individual
Brij N. Agrawal

22b Telephone *(Include Area code)*
(408) 646-3338

22c Office Symbol
AA/Ag

DD FORM 1473, 84 MAR

83 APR edition may be used until exhausted

All other editions are obsolete

security classification of this page
Unclassified

Approved for public release; distribution is unliminted

Experimental Verification
of
Attitude Control Techniques
for
Flexible Spacecraft Slew Maneuvers

by

Jeffrey A. Hailey
Lieutenant, United States Navy
B.S. Physics, University of California at Davis, 1985
M.S. Astronautical Engineering, Naval Postgraduate School, 1991

Submitted in partial fulfillment
of the requirements for the degree of

ENGINEER OF AERONAUTICS AND ASTRONAUTICS

from the

NAVAL POSTGRADUATE SCHOOL
March 1992

ABSTRACT

The experimental verification of attitude control designs for flexible spacecraft is essential for reliable operation in space. The Flexible Spacecraft Simulator (FSS) at the Naval Postgraduate School is designed to test a variety of control designs. The experimental setup simulates pitch axis motion of a flexible spacecraft consisting of a rigid central body and a flexible appendage connecting a reflector. The primary actuators are a reaction wheel and thrusters. Angular position information is obtained with a rotary variable differential transformer (RVDT) and angular rate information is obtained by a solid state rate sensor. Two analytical models are derived: one based on cantilever modes, the other based on system modes. Both are the result of linearized equations of motion which assume small flexible displacements and rates. Slew maneuvers are conducted using four separate controllers. They are proportional-derivative (PD), torque profiles, bang-bang and optimal controllers. Techniques for state estimation are explored for the optimal controller since the standard estimation methods prove to be unsatisfactory. The sinusoidal torque profile delivers the best performance overall with the PD a close second. Momentum wheel desaturation with thrusters and thruster slew maneuvers are also performed. In all cases, experimental results are in close agreement with analytical predictions.

C.1

TABLE OF CONTENTS

I. INTRODUCTION 1

  A. MOTIVATION FOR RESEARCH 1

  B. SCOPE OF THESIS 1

II. EXPERIMENTAL SETUP 3

  A. SIMULATOR CONFIGURATION 3

III. ANALYTICAL MODEL 7

  A. EQUATIONS OF MOTION 7

  B. SYSTEM MODEL 13

  C. FINITE ELEMENT MODEL 16

IV. SLEW CONTROL 22

  A. PROPORTIONAL-DERIVATIVE CONTROL 22

    1. Formulation 22

    2. Implementation 23

  B. OPTIMAL CONTROL 29

    1. Formulation 29

    2. Implementation 30

  C. CLASSIC BANG-BANG CONTROL 39

    1. Formulation 39

    2. Implementation 39

  D. TORQUE SHAPING 44

    1. Sinusoidal 44

    2. Pseudo-Square 51

V. BUILDING AN ESTIMATOR 58

VI. SYSTEM MODEL SLEW MANEUVERS 67

DUDLEY KNOX LIBRARY
NAVAL POSTGRADUATE SCHOOl
MONTEREY CA 93943-5101

A. EIGENSTRUCTURE ASSIGNMENT (REGULATOR) 67
B. EIGENSTRUCTURE ASSIGNMENT (ESTIMATOR) 68
VII. THRUSTER ACTUATION 71
A. THRUSTER SYSTEM OVERVIEW 71
B. MOMENTUM WHEEL DESATURATION 73
C. SLEW CONTROL 77
VIII. CONCLUSIONS 82
A. RECOMMENDATIONS FOR FURTHER STUDY 84
APPENDIX A 87
APPENDIX B 94
APPENDIX C 97
APPENDIX D 109
REFERENCES 111
INITIAL DISTRIBUTION LIST 112

LIST OF FIGURES

Figure 1. Flexible Spacecraft Simulator Configuration 4

Figure 2. Flexible Spacecraft Simulator 5

Figure 3. Thruster System Configuration 6

Figure 4. Analytical Model 8

Figure 5. Node Locations 17

Figure 6. First Mode 18

Figure 7. Mode Two 18

Figure 8. Mode Three 19

Figure 9. Mode Four 19

Figure 10. Mode Five 20

Figure 11. Mode Six 20

Figure 12. PD Controller Block Diagram 24

Figures 13 and 14. PD Controller Response 25

Figure 15. Arm Deflection for a 30° Slew 26

Figure 16. Arm Deflection for a 60° Slew 26

Figure 17. Phase Plot for a 30° Slew 27

Figure 18. Phase Plot for a 60° Slew 28

Figure 19. LQG Controller Block Diagram 32

Figures 20 and 21. LQG Response 33

Figure 22. Arm Deflection for a 30° Slew 34

Figure 23. Arm Deflection for a 60° Slew 34

Figure 24. Reconstructed Positions 35

Figure 25. Reconstructed Rates 36

Figure 26. Phase Plot for a 30° Slew 37

Figure 27. Phase Plot for a 60° Slew 38

Figure 28. Bang-Bang Block Diagram.. 40

Figure 29 and 30. Bang-Bang Response 41

Figure 31. Arm Deflection for a 30° Slew.. 42

Figure 32. Arm Deflection for a 60° Slew.. 42

Figure 33. Phase Plot for a 30° Slew 43

Figure 34. Phase Plot for a 60° Slew 43

Figure 35. Sinusoidal Torque Profile Block Diagram.. 46

Figure 36. Reference Curves 47

Figures 37 and 38. Sinusoidal Torque Shape Response 48

Figure 39. Arm Deflection for a 30° Slew.. 49

Figure 40. Arm Deflection for a 60° Slew.. 49

Figure 41. Phase Plot for a 30° Slew 50

Figure 42. Phase Plot for a 60° Slew 50

Figure 43. Pseudo-Square Torque Profile Block Diagram 52

Figure 44. Reference Curves 53

Figures 45 and 46. Pseudo-Square Controller Response.. 54

Figure 47. Arm Deflection for a 30° Slew.. 55

Figure 48. Arm Deflection for a 60° Slew.. 55

Figure 49. Phase Plot for a 30° Slew 56

Figure 50. Phase Plot for a 60° Slew 57

Figure 51. Reconstructed Positions.. 61

Figure 52. Reconstructed Rates.. 62

Figure 53. Reconstructed Positions.. 63

Figure 54. Reconstructed Rates.. 64

Figures 55 and 56. Optimal Response.. 65

Figure 57. Arm Deflection for a 30° Slew.. 66

Figure 58. Arm Deflection for a 60° Slew 66
Figure 59. Thruster System Schematic 73
Figure 60. Momentum Dumping Block Diagram 75
Figure 61. 30° Slew Maneuver Followed by Momentum Dumping 76
Figure 62. Wheel Speed During Desaturation 76
Figure 63. Thruster Slew Block Diagram 79
Figures 64 and 65. Thruster Slew Response 80
Figure 66. Arm Deflection for a 30° Slew 81
Figure 67. Arm Deflection for a 60° Slew 81
Figure A1. Motor Controller Block Diagram 93
Figure C1. Modal Frequency Verification 109

ACKNOWLEDGEMENTS

Many people have contributed to the continuing success of this project. Some of the most notable efforts are presented here. Mr. Rafford Bailey, lab technician for the FSS, without whom the hardware design and assembly would have been impossible. Mr. Pat Hickey, lab and shop manager for the Department of Aeronautics and Astronautics, whose cooperation in expediting the manufacturing of parts is much appreciated. Mr. Paul Carey of the Naval Research Laboratories who provided the solenoid valves for the thrusters. LT R. Joseph Watkins, upon whose previous research this thesis is built. LCDR (Sel) Evan S. Jones who struggled with me to understand the AC-100 and Matrix$_X$ hardware/software interfacing. LT Christopher D. Sortun for his tutoring on the Bang-Bang controller and other non-linear subtleties. Professor John L. Junkins, George J. Eppright Chair Professor at Texas A&M University and Visiting Co-Chair of the Space Systems Academic Group at NPS, whose guidance was responsible for solving the estimator problem and for producing the eigenstructure assignment developement. Finally, Professor Brij N. Agrawal of the Department of Aeronautics and Astronautics at NPS, who obtained funding for the FSS and who is mostly responsible for the success of this project.

I. INTRODUCTION

A. MOTIVATION FOR RESEARCH

Analytical techniques in flexible structural dynamics and control are rapidly accumulating in the literature while relatively few experiments [References 1, 2, 3] exist for verification. This thesis develops a mathematical model for an actual system exhibiting the low frequency structural characteristics of a spacecraft structure. The model is developed by using rigid body coordinates for the central body and cantilever modal coordinates for the flexible body. Using this model, classical and modern control theory are applied within the constraints of the experimental hardware. The analytical simulation and experimental results are then compared to examine the accuracy and applicability of the analytical model.

B. SCOPE OF THESIS

Chapter II describes the experimental setup with its assumptions and constraints. Chapter III develops the equations of motion by Lagrangian dynamics using a hybrid coordinate system and establishes the two analytical models. These equations are linearized on the assumption of small displacements and rates. The finite element model for the cantilever modes is also presented for the first six modes.

Chapter IV derives the four controllers and compares the analytical predictions with experimental results. The PD controller uses gains derived from the rigid body model limiting the control bandwidth to one-half of the fundamental cantilever frequency. Two torque profiles are discussed. The optimal controller is presented here and again in Chapter V. Chapter V explores the problem of constructing an adequate estimator and develops an interesting solution. Chapter VI derives the eigenstructure assignment regulator and estimator which allows the designer to place poles for stability. This is only a preliminary developement and does not produce adequate results to date.

Chapter VII concerns thruster actuation including a system overview.

II. EXPERIMENTAL SETUP

A. SIMULATOR CONFIGURATION

The Flexible Spacecraft Simulator configuration is shown in Figure 1. It approximates the pitch axis motion of a three dimensional model used in a study conducted by INTELSAT (Reference 4). The Simulator at NPS has a central rigid body representing a spacecraft main body and a flexible appendage corresponding to a reflector supported by a flexible astromast. It is floated on a flat, smooth granite table to reduce friction and to simulate low-gravity operations in two dimensions since gravity acts perpendicular to all displacements and consequently does no work. The central body is attached to an I-beam above the table through an air-bearing which allows only rotational motion. The assemblage is actuated by a momentum wheel mounted on the main body. An RVDT and a rate-gyro provide the angular position and velocity of the central hub. The fundamental cantilever frequency of the flexible structure is 0.14 Hz.

Control laws are implemented using a VAX station 3100 in conjunction with an AC-100 controller manufactured by Integrated Systems, Inc. The System Build software associated with the AC-100 runs with MATRIX_X and allows the user to build control schemes with block diagrams similar to a flow chart. The computer translates these diagrams to C code which is subsequently loaded into the AC-100 for execution. Included in this process is the ability to create custom on-screen displays which allow the user real-time interaction with the controller while it is running. The AC-100 hardware consists of A to D and D to A converters providing many options for sensor and actuator connections. The Flexible Spacecraft Simulator is shown in Figure 2.

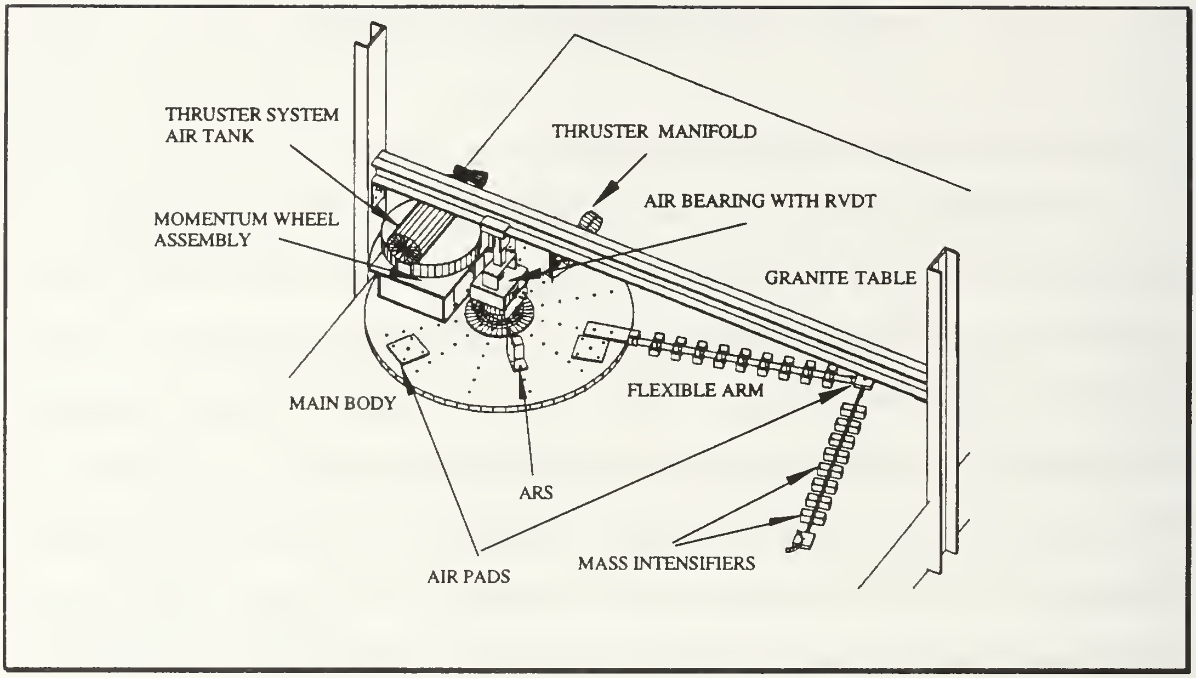
THRUSTER SYSTEM AIR TANK
THRUSTER MANIFOLD
AIR BEARING WITH RVDT
MOMENTUM WHEEL ASSEMBLY
GRANITE TABLE
FLEXIBLE ARM
MAIN BODY
ARS
AIR PADS
MASS INTENSIFIERS

Figure 1. Flexible Spacecraft Simulator Configuration

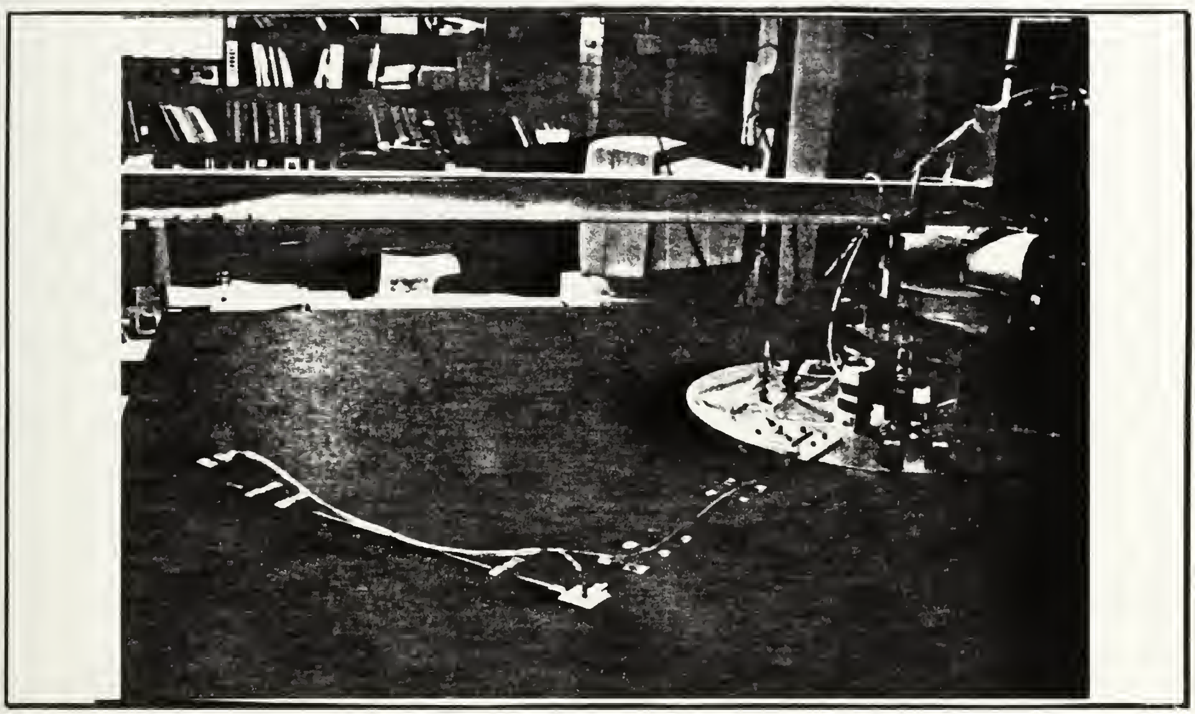

Figure 2. Flexible Spacecraft Simulator

A full description of the sensors, momentum wheel assembly and the AC-100 controller can be found in Reference 4. The thruster system is shown in Figure 3. It consists of a 13.3 cubic foot, 3000 psi supply tank connected to a 3000-200 psi pressure regulator with 3500 psi flexible hose. Pressure gauges are positioned on both sides of the regulator to monitor fluctuations. Two 250 psi, 0.0224 lbm/sec hydrazine solenoid valves obtained from the Naval Research Laboratory provide on/off thrust control. The system uses 200 psi dry air so thrust levels are less than those for hydrazine. The valve outlet is one-sixteenth inch diameter which provides 0.4178 lbf thrust. The solenoid valves are attached to a manifold in opposing positions.

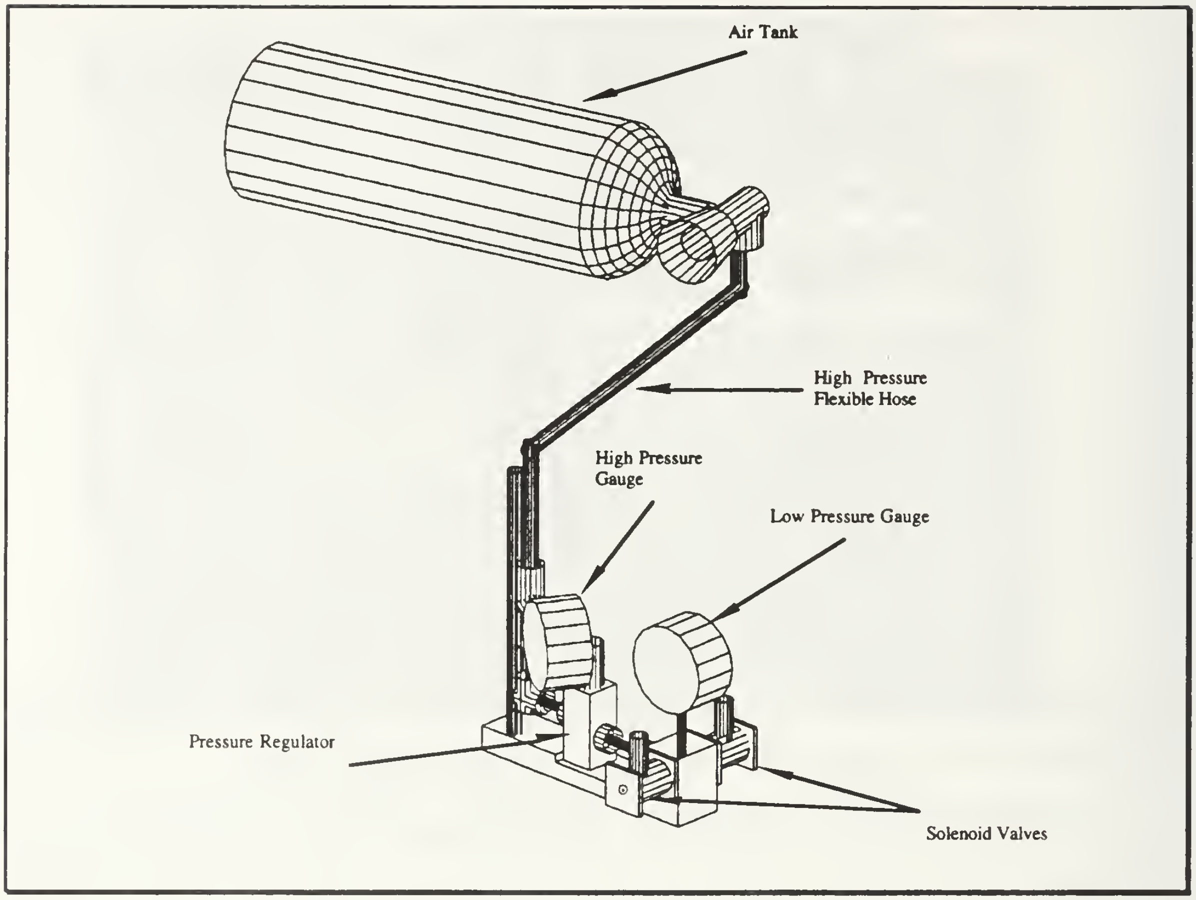
Air Tank
High Pressure Flexible Hose
High Pressure Gauge
Low Pressure Gauge
Pressure Regulator
Solenoid Valves

Figure 3. Thruster System Configuration

III. ANALYTICAL MODEL

A. EQUATIONS OF MOTION

The analytical model [Reference 5] is shown in Figure 4. It is comprised of a flexible structure attached to a rigid central body restricted to rotation only. The X, Y, Z axes are inertially fixed. The x, y, z axes are fixed with respect to the rigid body and are obtained through a rotation θ about the Z axis. The location of the wheel rotation axis is (x_o, y_o) and the coordinate system x_W, y_W rotates with the wheel. The equations of motion are derived by using a hybrid-coordinate system, rotational angle θ of the rigid body and cantilever modal coordinates of the flexible body. Lagrange's equations are used and require an expression for the kinetic energy, T.

$$T = \frac{1}{2}\int_R (\vec{V}_R \cdot \vec{V}_R)dm + \frac{1}{2}\int_F (\vec{V}_F \cdot \vec{V}_F)dm + \frac{1}{2}\int_W (\vec{V}_W \cdot \vec{V}_W)dm \tag{1}$$

where $\vec{V}_R$ = velocity of a particle on the rigid body

$\vec{V}_F$ = velocity of a particle on the flexible body

$\vec{V}_W$ = velocity of a particle on the momentum wheel

The velocities $\vec{V}_R$, $\vec{V}_W$ and $\vec{V}_F$ are given by

$$\vec{V}_R = \dot{\theta}\vec{k} \times \vec{r}_R \tag{2}$$

$$\vec{V}_F = \dot{\theta}\vec{k} \times \vec{r}_F + \dot{\vec{u}} + \dot{\theta}\vec{k} \times \vec{u} \tag{3}$$

$$\vec{V}_W = (\dot{\theta} + \dot{\theta}_W)\vec{k} \times \vec{r}_W + \dot{\theta}\vec{k} \times \vec{r}_o \tag{4}$$

where $\vec{r}_R$ = position vector of a particle on the rigid body

$\vec{r}_F$ = position vector of a particle on the flexible body

$\vec{r}_w$ = position vector of a particle on the momentum wheel

$\vec{u}$ = elastic deformation vector of a particle on the flexible body

$\vec{i}, \vec{j}, \vec{k}$ = unit vectors along axes x, y, z

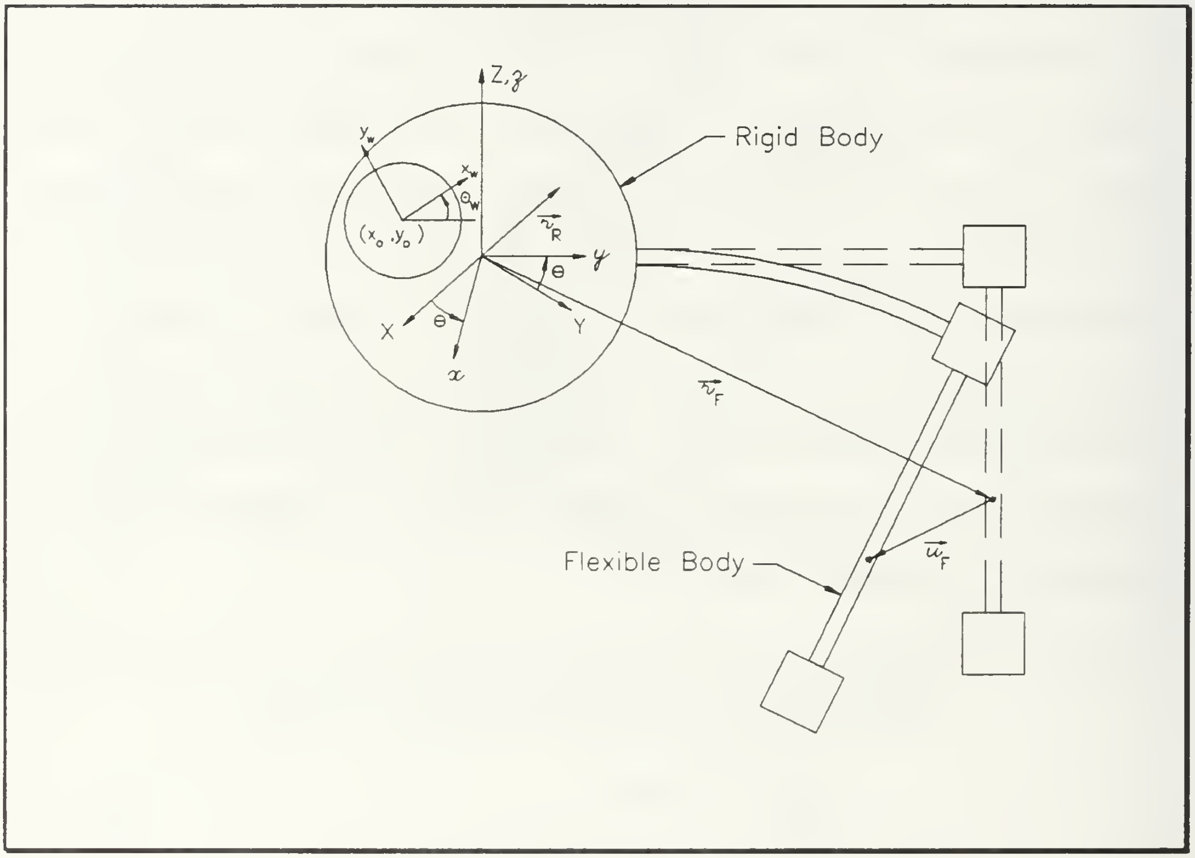
Z, z
Rigid Body
y_w
x_w
θ_w
(x_o, y_o)
$\vec{r}_R$
y
θ
X
θ
Y
x
$\vec{r}_F$
Flexible Body
$\vec{u}_F$

Figure 4. Analytical Model

Table 1. Numerical Values

Name	Symbol	Value	Units
Total MOI	I_{zz}^{01}	11.17	kg-m^2
Wheel MOI	I_w	0.0912	kg-m^2
Wheel mass	m_w	10.66	kg
Total mass	m_t	65.35	kg
Center of Wheel	$\lvert\vec{r}_o\rvert$	0.20	m

Substituting Equations (2), (3) and (4) into Equation (1) yields

$$
\begin{aligned}
T = {} & \frac{1}{2}\int_R \dot{\theta}^2(x_R^2 + y_R^2)dm + \frac{1}{2}\int_F \left[\dot{\theta}^2(x_F^2 + y_F^2) + (\dot{u}_x^2 + \dot{u}_y^2) + \dot{\theta}^2(u_x^2 + u_y^2)\right]dm \\
& + \frac{1}{2}\int_F \left[2\dot{\theta}(x_F\dot{u}_y - y_F\dot{u}_x) + 2\dot{\theta}^2(x_F u_x + y_F u_y) + 2\dot{\theta}(\dot{u}_y u_x - \dot{u}_x u_y)\right]dm \\
& + \frac{1}{2}\int_W \left[\dot{\theta}^2(x_o^2 + y_o^2) + \dot{\theta}^2(x_W^2 + y_W^2) + 2\dot{\theta}^2(x_o x_W + y_o y_W) + \dot{\theta}_W^2(x_W^2 + y_W^2)\right]dm \\
& + \frac{1}{2}\int_W \left[2\dot{\theta}\dot{\theta}_W(x_W^2 + y_W^2) + 2\dot{\theta}_W\dot{\theta}(x_o x_W + y_o y_W)\right]dm
\end{aligned}
\tag{5}
$$

The generalized coordinates used for the equations of motion will be θ, θ_W and u. Assuming the wheel is rotating about its center of mass eliminates terms with single powers of x_W and y_W. Assuming that $u, \dot{u}, \dot{\theta}$ are small, terms higher than second order resulting from any combination of $u, \dot{u}, \dot{\theta}$ can be ignored. This eliminates terms 4, 6 and 7 from Equation (5). Terms 8 and 9 represent the contribution of the wheel's inertia to the total inertia. Consequently, Equation (5) reduces to

$$
\begin{aligned}
T = {} & \frac{1}{2}I_{zz}\dot{\theta}^2 + \frac{1}{2}I_W\dot{\theta}_W^2 + \frac{1}{2}I_W\dot{\theta}\dot{\theta}_W + \frac{1}{2}\int_F (\dot{u}_x^2 + \dot{u}_y^2)dm \\
& + \dot{\theta}\int_F (x_F\dot{u}_y - y_F\dot{u}_x)dm
\end{aligned}
\tag{6}
$$

where

$$
\begin{aligned}
I_{zz} & = I_{zz}^R + I_{zz}^F + I_{zz}^W \\
& = \int_R (x_R^2 + y_R^2)dm + \int_F (x_F^2 + y_F^2)dm + \int_W (x_w^2 + y_w^2)dm \\
& \quad + m_w(x_o^2 + y_o^2)
\end{aligned}
\tag{7}
$$

The elastic deformation u is represented in terms of cantilever modal coordinates of the flexible body as

$$u_x = \sum_{i=1}^{n} \phi_i^x q_i(t)$$

$$u_y = \sum_{i=1}^{n} \phi_i^y q_i(t) \tag{8}$$

where for the i_{th} mode, $q_i(t)$ is the modal coordinate, ϕ_i^x is the component of the modal vector along the x axis, and ϕ_i^y is the component of the modal vector along the y axis. Substituting Equation (8) into Equation (6) gives

$$T = \frac{1}{2} I_{zz} \dot{\theta}^2 + \frac{1}{2} I_W \dot{\theta}_W^2 + I_W \dot{\theta} \dot{\theta}_W$$

$$+ \frac{1}{2} \int_F \left(\sum_{i=1}^{n} \sum_{j=1}^{n} \left[\phi_i^x \phi_j^x + \phi_i^y \phi_j^y \right] \dot{q}_i \dot{q}_j \right) dm + \dot{\theta} \int_F \left[x_F \sum_{i=1}^{n} \phi_i^y \dot{q}_i - y_F \sum_{i=1}^{n} \phi_i^x \dot{q}_i \right] dm \tag{9}$$

Normalizing the modal vectors to unity modal masses (mass normalizing) and using orthogonality of the modal vectors, Equation (9) is simplified to

$$T = \frac{1}{2} I_{zz} \dot{\theta}^2 + \frac{1}{2} I_W \dot{\theta}_W^2 + I_W \dot{\theta} \dot{\theta}_W + \frac{1}{2} \sum_{i=1}^{n} \dot{q}_i^2 + \dot{\theta} \sum_{i=1}^{n} D_i \dot{q}_i \tag{10}$$

where

$$D_i = \int_F (x_F \phi_i^y - y_F \phi_i^x) dm$$

= rigid elastic coupling.

The potential energy of the flexible body due to elastic stiffness in terms of modal coordinates is given by

$$V = \frac{1}{2}\sum_{i=1}^{n} \omega_i^2 q_i^2 \tag{11}$$

where ω_i is the is the natural frequency of the i_{th} mode.

The work done in the system is

$$\delta W = T_t\delta(\theta + \theta_W) - T_t\delta\theta + T_D\delta\theta \tag{12}$$

$$= T_t\delta\theta_W + T_D\delta\theta$$

where T_D = external torque on the main body

$T_t = T_M + T_F$ = torque acting on the wheel and the reaction torque torque on the main body

The Lagrange's equation is

$$\frac{d}{dt}\left(\frac{\partial L}{\partial \dot{\mu}_i}\right) - \frac{\partial L}{\partial \mu_i} = Q_i \tag{13}$$

where $L = T - V$, μ_i is the generalized coordinate and Q_i is the generalized force. The generalized coordinates for the system are θ, θ_W, q_i, ..., q_n. The torque Tt is applied to the rigid body. Therefore,

$$Q_\theta = T_D \tag{14}$$

Substituting Equations (10), (11) and (14) into Equation (13), the equations of motion of the system are

$$I_{zz}\ddot{\theta} + \sum_{i=1}^{n} D_i\ddot{q}_i + I_w\ddot{\theta}_w = T_D$$

$$\ddot{q}_i + \omega_i^2 q_i + D_i\ddot{\theta} = 0 \tag{15}$$

Let $I_w\ddot{\theta}_w = I_w\dot{\Omega} = -T_c$ (16)

where $\dot{\Omega}$ = spin rate of the wheel with respect to the central body

Assuming modal damping for the cantilever modes, the equations of motion become

$$I_{zz}\ddot{\theta} + \sum_{i=1}^{n} D_i\ddot{q}_i = T_M = T_D + T_C$$

$$\ddot{q}_i + 2\xi_i\omega_i\dot{q}_i + \omega_i^2 q_i + D_i\ddot{\theta} = 0 \qquad (17)$$

A state space representation of the system equations is

$$\begin{aligned}\dot{X} &= [A]X + [B]U\\ Y &= [C]X + [D]U\end{aligned} \qquad (18)$$

where $X = \left[\theta,\ q_1, \cdots, q_n,\ \dot{\theta},\ \dot{q}_1, \cdots, \dot{q}_N\right]^T$

$Y = \left[\theta,\ \dot{\theta}\right]^T$

$U = T_t$

$D = 0$

$$[A] = \frac{1}{I_{zz}^0}\begin{bmatrix} 0 & 0 & \cdots & 0 & I_{zz}^0 & 0 & \cdots & 0 \\ 0 & 0 & \cdots & 0 & 0 & I_{zz}^0 & \cdots & 0 \\ \vdots & \vdots & & \vdots & \vdots & \vdots & & \vdots \\ 0 & F_1 & \cdots & F_n & 0 & H_1 & \cdots & H_n \\ 0 & -G_1 & \cdots & -D_iF_n & 0 & J_1 & \cdots & D_1H_n \\ \vdots & \vdots & & \vdots & \vdots & \vdots & & \vdots \\ 0 & -D_nF_1 & \cdots & -G_n & 0 & -D_nH_1 & \cdots & -J_n \end{bmatrix} \qquad (19)$$

where

$$I_{zz}^0 = I_{zz} - \sum_{i=1}^{n} (D_i)^2$$

$$F_i = D_i\omega_i^2$$

$$G_i = \omega_i^2 I_{zz}^0 + D_iF_i \qquad (20)$$

$$H_i = 2\xi_i\omega_i D_i$$

$$J_i = 2\xi_i\omega_i I_{zz}^0 + D_i H_i$$

$$[C] = \begin{bmatrix} 1 & 0 & \cdots & 0 & 0 & 0 & \cdots & 0 \\ 0 & 0 & \cdots & 0 & 1 & 0 & \cdots & 0 \end{bmatrix} \tag{21}$$

B. SYSTEM MODEL

The system model approach begins with the linearized, undamped equations of motion (Equation 15). Instead of directly forming the states and the state space model of Equations (18) through (21), Equation (15) is expressed as a second order partitioned system.

$$\left[\begin{array}{c|c} I_{zz} & D^T \\ \hline D & I \end{array}\right] \begin{Bmatrix} \ddot{\theta} \\ \ddot{q} \end{Bmatrix} + \left[\begin{array}{c|c} 0 & 0 \\ \hline 0 & \lambda \end{array}\right] \begin{Bmatrix} \theta \\ q \end{Bmatrix} = \begin{Bmatrix} T_t \\ -- \\ 0 \end{Bmatrix} \tag{22}$$

where $\lambda = \begin{bmatrix} \ddots & & \\ & \omega^2 & \\ & & \ddots \end{bmatrix}$ and $D = \begin{Bmatrix} D_1 \\ D_2 \\ D_3 \\ D_4 \\ D_5 \\ D_6 \end{Bmatrix}$ (23)

The matrix coefficient of acceleration will be called M and the matrix coefficient of position will be called K. The vector D is defined by Equation (10) and represents the rigid elastic coupling. The matrix λ is a diagonal matrix of the cantilever natural frequencies squared. M and K are both 7X7 matrices. The lower right partition of M is actually the modal matrix for the cantilever (flexible) equation and it is normalized to unity in the finite element program. The system approach is to normalize M to decouple the two equations. First, the coordinates are mapped into system modal space

$$\begin{Bmatrix} \theta \\ q \end{Bmatrix} = \begin{bmatrix} & & \\ & \Phi & \\ & & \end{bmatrix} \begin{Bmatrix} \eta \end{Bmatrix} \tag{24}$$

Equation (22) now takes the form

$$[M][\Phi]\{\ddot{\eta}\} + [K][\Phi]\{\eta\} = \begin{Bmatrix} T_t \\ 0 \end{Bmatrix} \tag{25}$$

Pre-multiplying Equation (25) by Φ^{-1} gives

$$[\Phi]^{-1}[M][\Phi]\{\ddot{\eta}\} + [\Phi]^{-1}[K][\Phi]\{\eta\} = [\Phi]^{-1}\begin{Bmatrix} T_t \\ 0 \end{Bmatrix} \tag{26}$$

For proper normalization, we require that

$$\begin{aligned} \Phi^{-1}M\Phi &= I \\ \Phi^{-1}K\Phi &= \Lambda \end{aligned} \tag{27}$$

where Λ is the diagonal matrix of system natural frequencies. The modal matrix Φ may be obtained by first solving the associated eigenvalue problem

$$\lambda M\varphi = K\varphi \tag{28}$$

whose solution yields eigenvectors of the form

$$\varphi^{-1}M\varphi = \begin{bmatrix} \ddots & & \\ & C & \\ & & \ddots \end{bmatrix} \tag{29}$$

The matrix C is diagonal with constant elements. If we normalize C so that

$$C^{-\frac{1}{2}} C \, C^{-\frac{1}{2}} = I \tag{30}$$

then we can identify the modal eigenvectors as

$$\Phi = \varphi \, C^{-\frac{1}{2}} \tag{31}$$

Now that the system modal natural frequencies and system modal matrix have been found, Equation (22) is decoupled and the state space representation of Equation (18) can be used. The state vector, X, is now represented by the system modal coordinates and their derivatives. The state space representation is

$$\begin{Bmatrix} \dot{\eta} \\ \ddot{\eta} \end{Bmatrix} = [A] \begin{Bmatrix} \eta \\ \dot{\eta} \end{Bmatrix} + \begin{Bmatrix} B \end{Bmatrix} u \tag{32}$$

The A matrix is simply written as

$$[A] = \left[\begin{array}{c|c} 0 & I \\ \hline -\Lambda & -2\xi\omega \end{array} \right] \tag{33}$$

where

$$\xi\omega = \begin{bmatrix} \xi_1\omega_1 & \cdots & 0 \\ \vdots & \ddots & \vdots \\ 0 & \cdots & \xi_6\omega_6 \end{bmatrix} \tag{34}$$

This term represents system damping and is assumed to be proportional. It will be determined experimentally and added to the model. The A matrix is 14X14 and is much simpler than the one of Equation (19).

The B matrix is given by

$$\begin{Bmatrix} B \end{Bmatrix} = \begin{Bmatrix} 0 \\ -- \\ \Phi^{-1} T_M \end{Bmatrix} \tag{35}$$

where

$$T_M = \begin{Bmatrix} T_M \\ 0 \\ 0 \\ 0 \\ 0 \\ 0 \end{Bmatrix} \qquad (36)$$

Appendix C contains the numerical values for the A and B matrices. Appendix D contains verification of the system modal frequencies.

C. FINITE ELEMENT MODEL

A finite element analysis was done to determine cantilever frequencies and mode shapes for the flexible appendage using the PAL2 software. Figure 5 shows the locations of the 20 nodes on the undeformed arm. Node one is the base point which is connected to the main body. Consequently, it is assumed to be fixed. The other 19 nodes are constrained to x-y plane deflections only and rotation about the z-axis. Figures 6 through 11 show th resulting mode shapes. The modal frequencies are given in Table 2. The 0.14 Hz fundamental frequency has been experimentally verified.

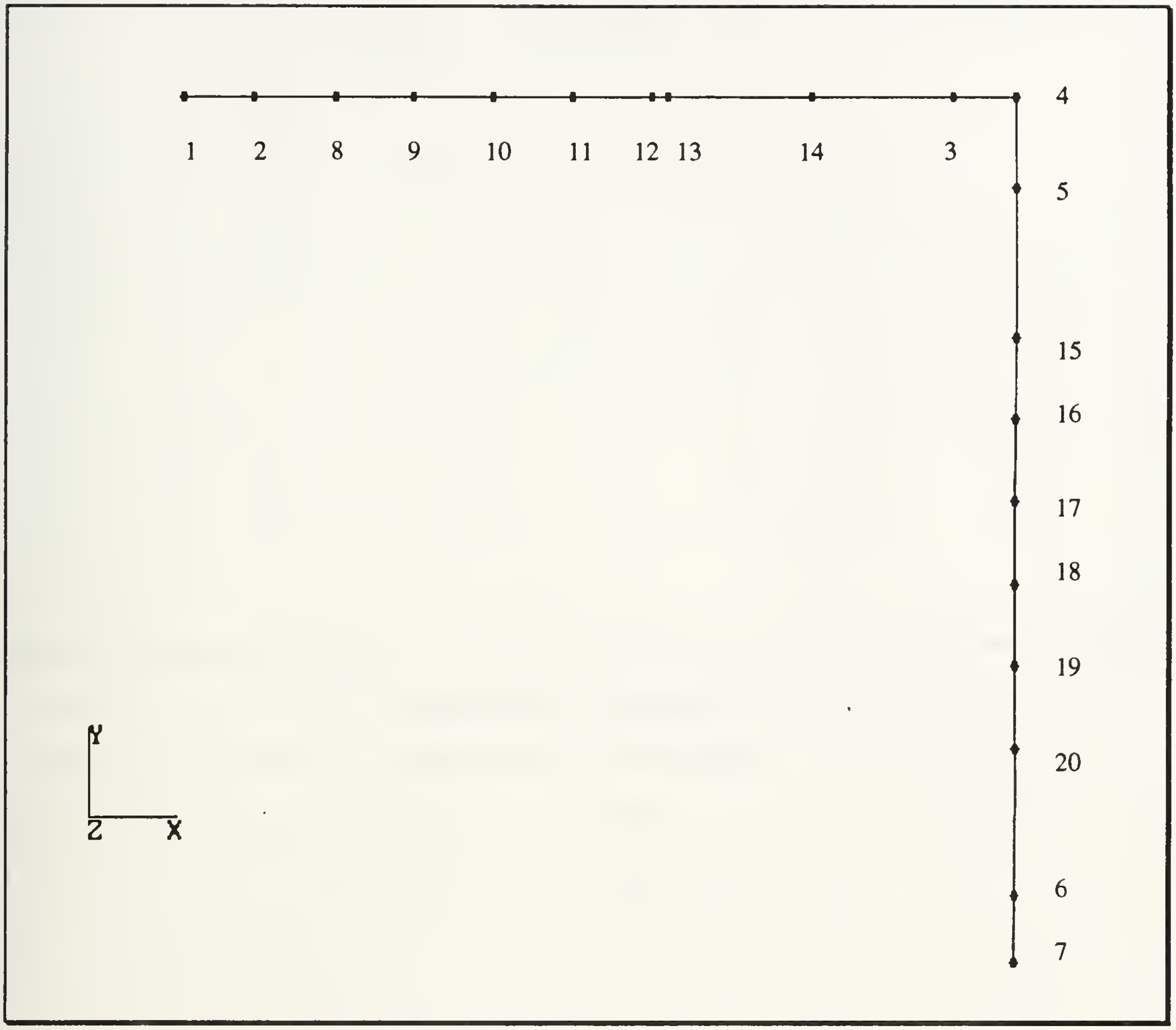
4
1
2
8
9
10
11
12
13
14
3
5
15
16
17
18
19
20
6
7
Y
Z
X

Figure 5. Node Locations

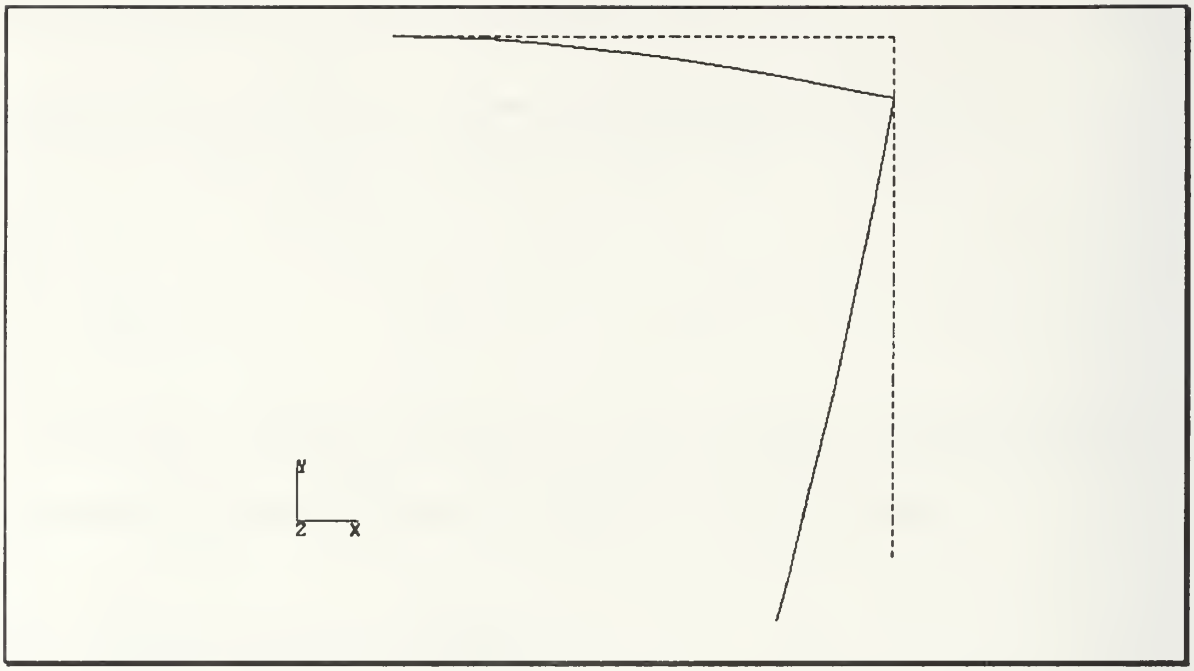

Figure 6. First Mode

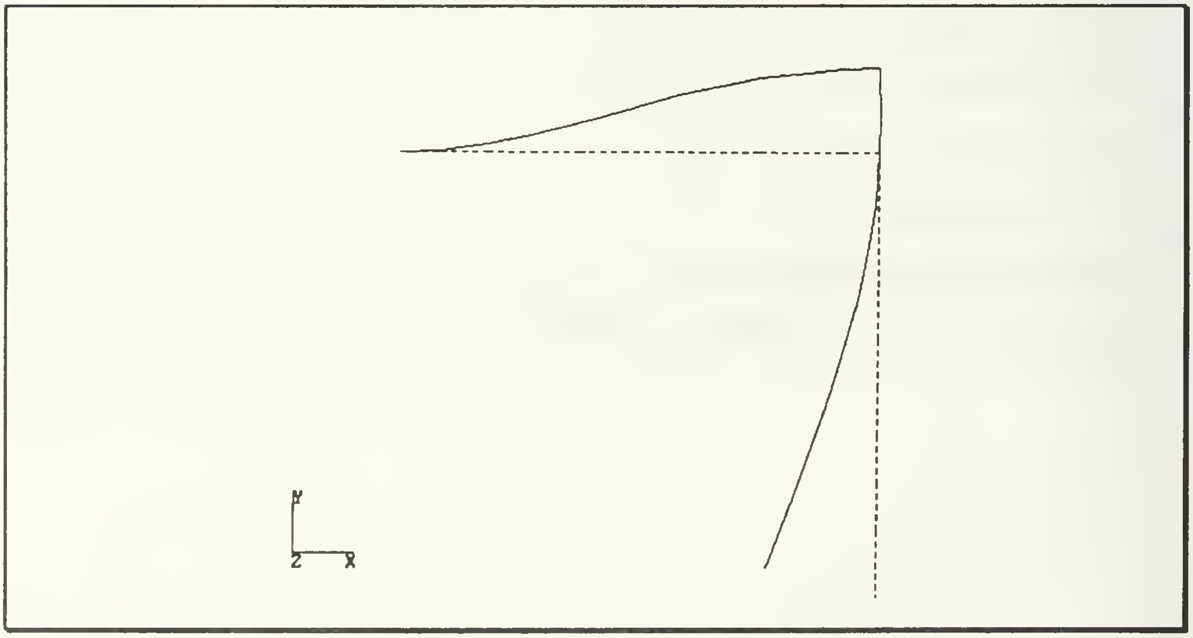

Figure 7. Mode Two

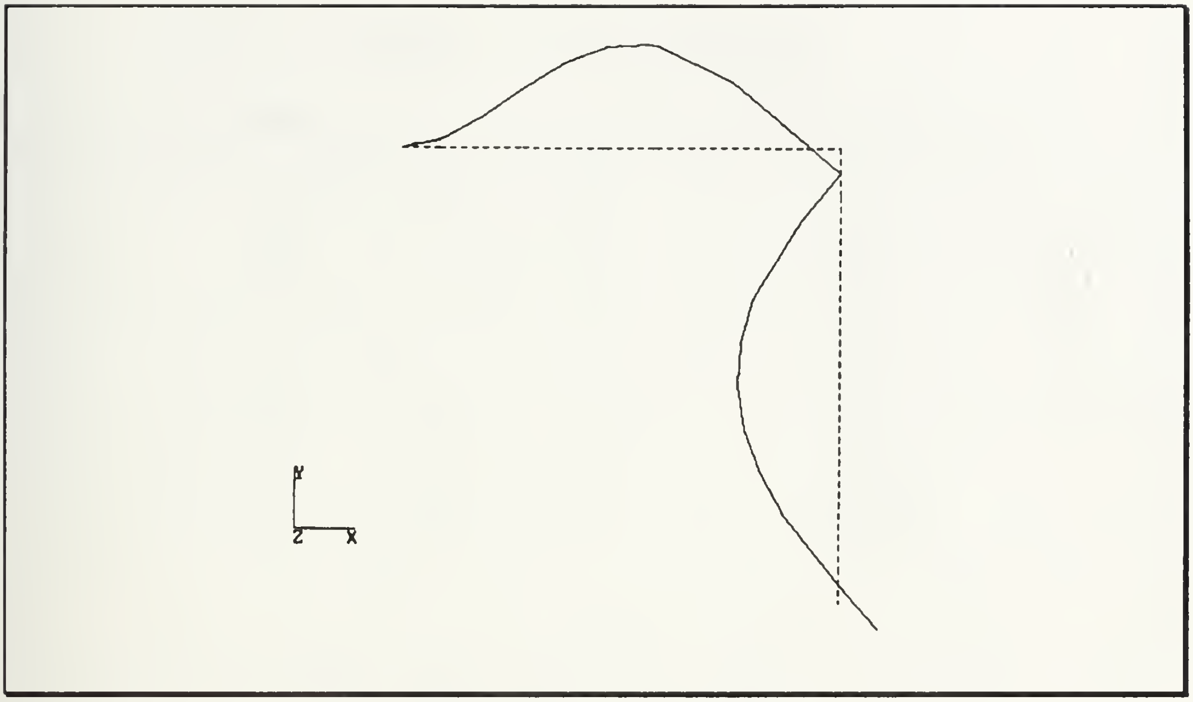

Figure 8. Mode Three

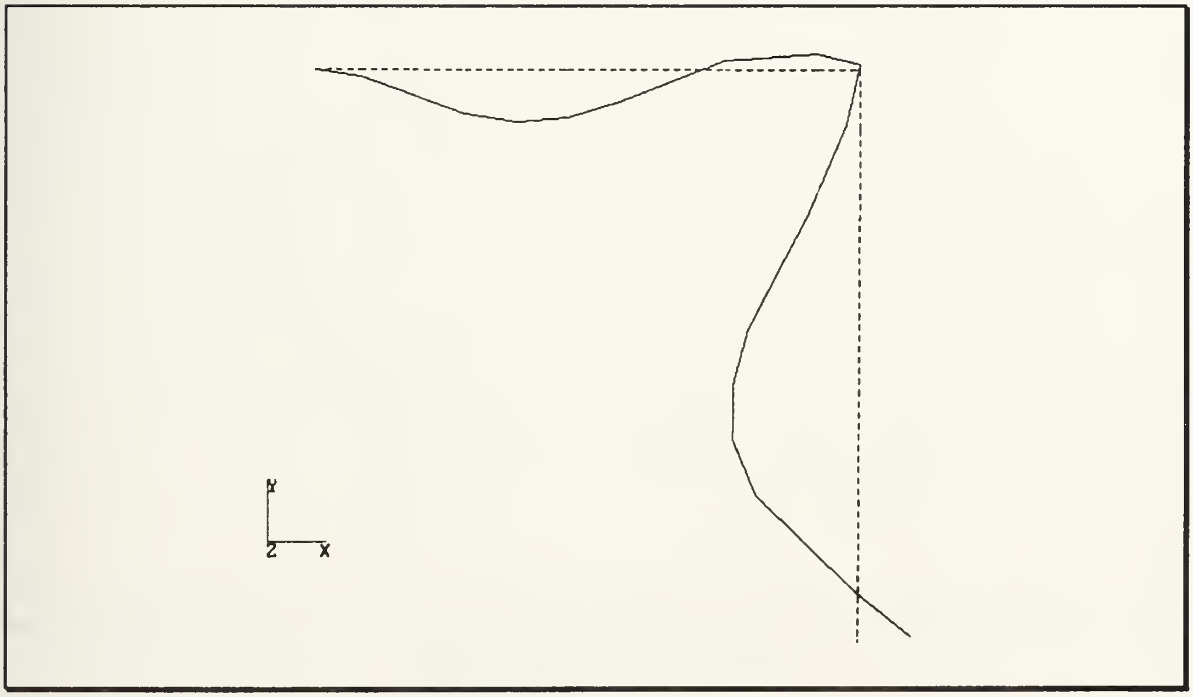

Figure 9. Mode Four

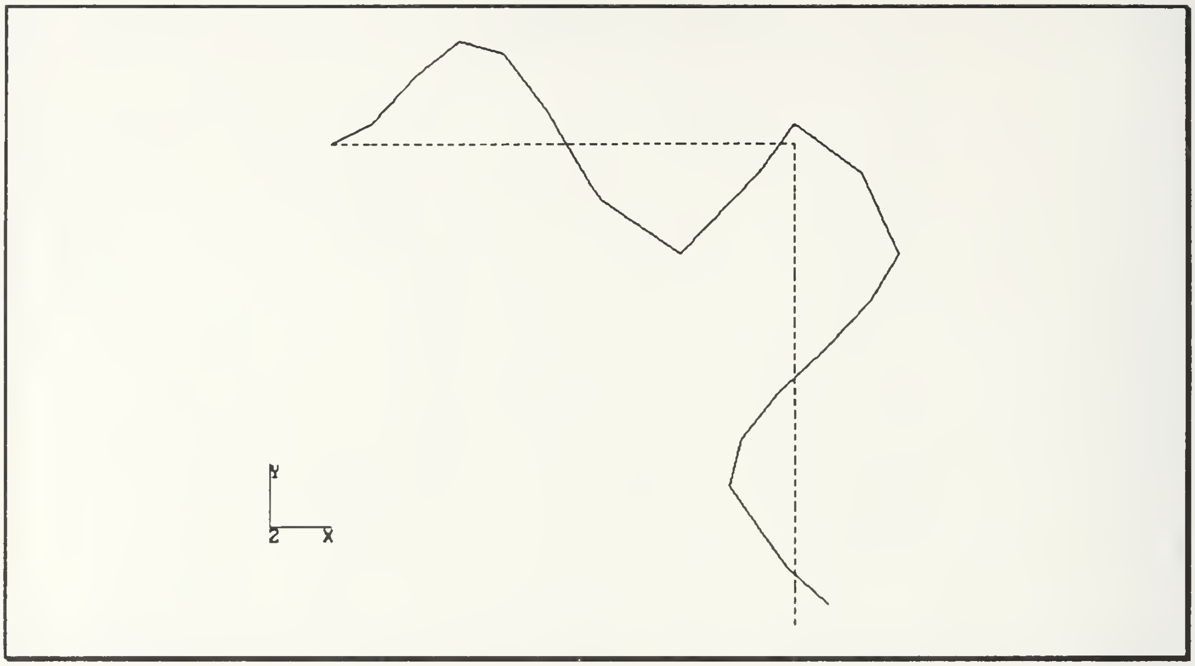

Figure 10. Mode Five

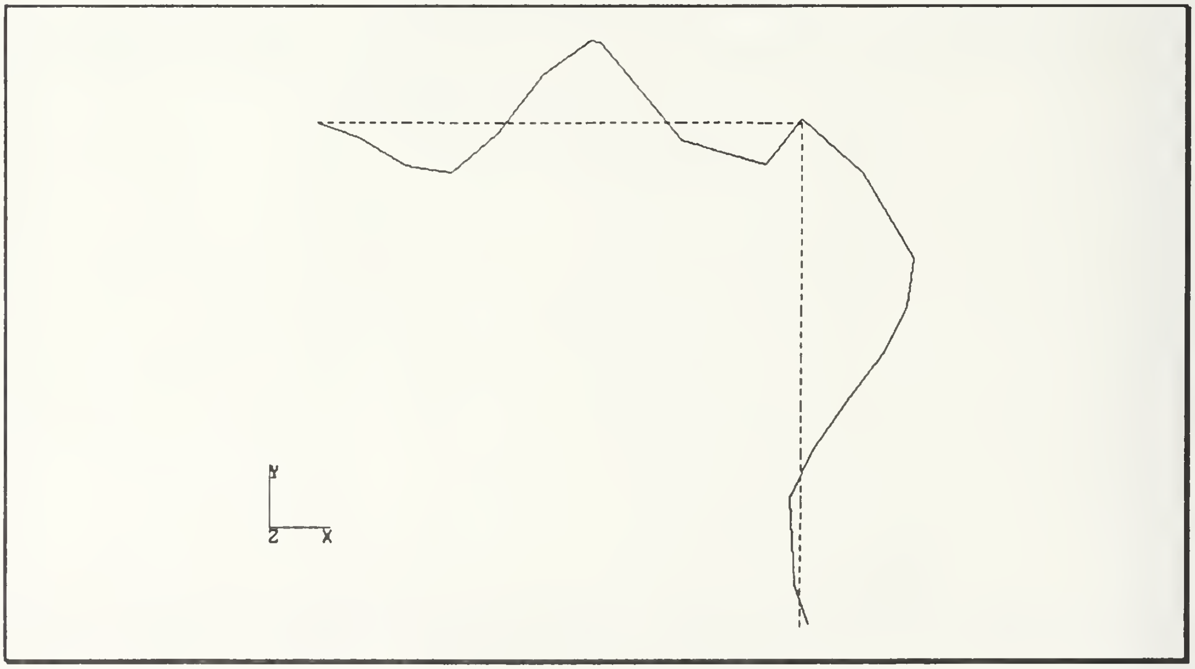

Figure 11. Mode Six

Table 2. Modal Frequencies

Mode	Frequency (Hz)
1	0.139
2	0.420
3	2.463
4	4.295
5	6.860
6	12.820

IV. SLEW CONTROL

A. PROPORTIONAL-DERIVATIVE CONTROL

Analytical simulations are performed using the first six cantilever modes of the flexible appendage. This causes X in Equation (18) to be a 14 state vector. The modal characteristics, natural frequencies and mode shapes are determined using the PAL2 finite element analysis program. For all the modes, modal damping has been experimentally determined to be 0.4 percent critical damping. Strain gauges are used to evaluate the modal damping.

1. Formulation

The classical technique of proportional derivative control is used by feeding back the central body angular position and angular rate. The control torque T_c is given by

$$T_c = -k(\theta_e + \tau\dot{\theta}) \tag{37}$$

where θ_e = angular error of the rigid body = $\theta - \theta_{ref}$

$\dot{\theta}$ = angular rate of the body

k = gain for the control

τ = time constant

The equation for the reaction wheel is

$$I_W\dot{\Omega} = -T_c \tag{38}$$

A variable cable induced spring torque affects the nominal angular position of the experimental setup. Assuming this torque to be constant during the maneuver,

$$T_t = -k(\theta_e + \tau\dot{\theta}) + T_D \tag{39}$$

2. Implementation

The MATRIX_x block diagram for this simulation is shown in Figure 12. The analytical simulation and experimental results are plotted together in Figures 13 and 14 for a 30° and a 60° slew. The dashed lines represent experimental data and the solid lines represent analytical prediction. There is a steady state error given by

$$\theta_{ss} = \frac{T_D}{k} \tag{40}$$

The control gains are determined with the classical pole placement analysis for a rigid body. The controller natural frequency is limited to less than half the fundamental frequency of the flexible appendage and the damping ratio is set to 0.9. The classical characteristic equation for the rigid $\frac{1}{s^2}$ plant is

$$s^2 + 2\xi\omega_n s + \omega_n^2 = 0 \tag{41}$$

ω_n = controller natural frequency = 0.06 Hz

ξ = damping ratio

From this the poles of the rigid system can be determined leading to the rigid body gains using MATRIX_x.

$k = 1.3985$ N-m/rad

$k\tau = 6.6773$ N-m-s/rad

The steady state position error is caused by a spring torque in the cabling to the motor. The cable spring torque is evaluated by observing the reaction wheel speed change after the assemblage has reached a steady state. The experimental steady state position error can be used to check the spring torque calculation with Equation (40). Figure 16 is the analytical arm deflection over time for a 30° slew. Figure 17 shows the arm motion for a 60° slew. The plots are adjusted to fix the base point for better comparison.

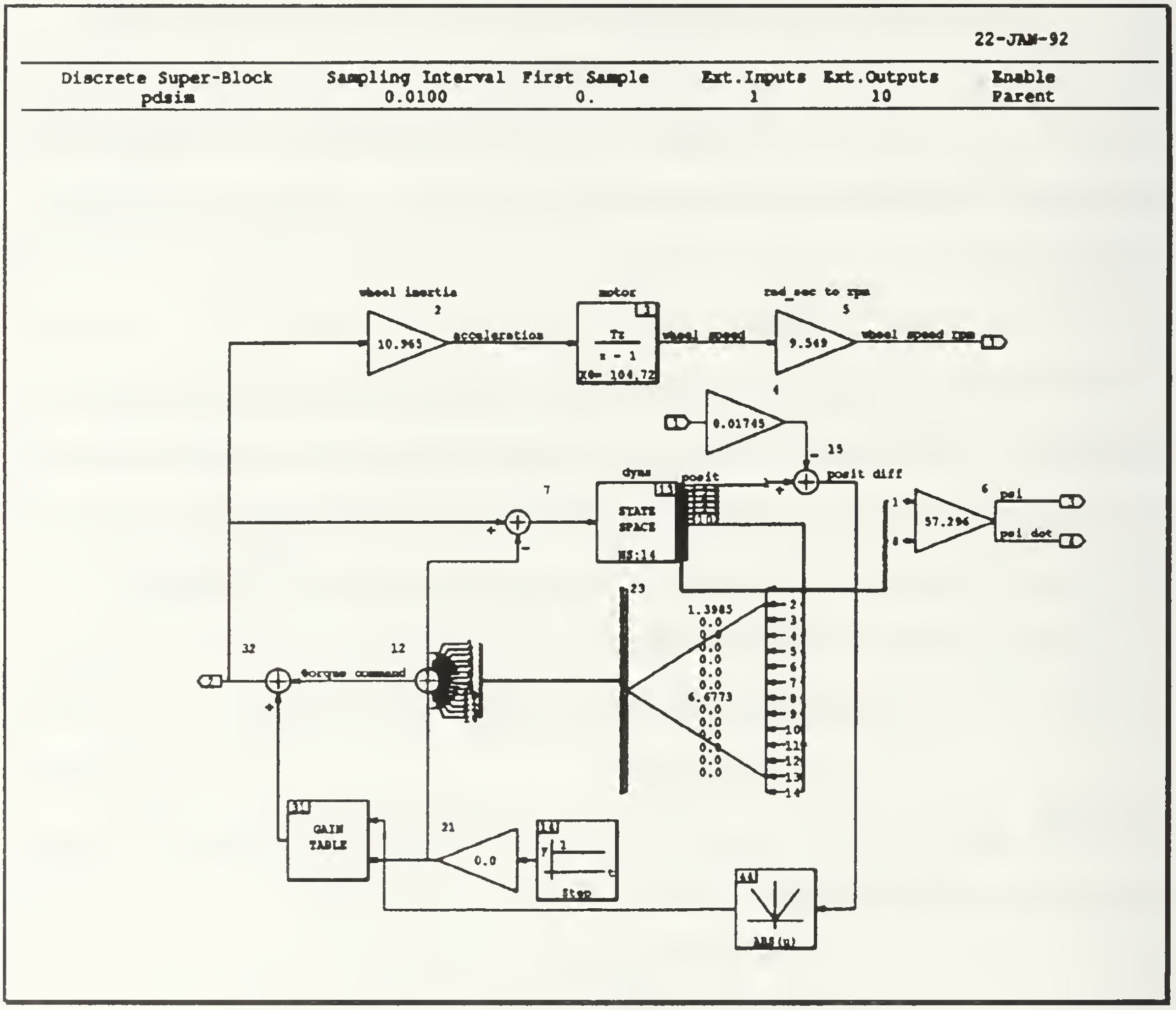

22-JAN-92

Discrete Super-Block	Sampling Interval	First Sample	Ext.Inputs	Ext.Outputs	Enable
pdsim	0.0100	0.	1	10	Parent

wheel inertia
2
10.965
acceleration
motor
Tz
z - 1
X0= 104.72
wheel speed
rad_sec to rpm
5
9.549
wheel speed rpm
4
0.01745
15
posit diff
dyns
posit
7
STATE
SPACE
NS:14
6
57.296
psi
psi dot
23
1.3985
0.0
0.0
0.0
0.0
0.0
0.0
6.6773
0.0
0.0
0.0
0.0
0.0
0.0
2
3
4
5
6
7
8
9
10
11
12
13
14
32
12
torque command
GAIN
TABLE
21
0.0
Step
ABS(u)

Figure 12. PD Controller Block Diagram

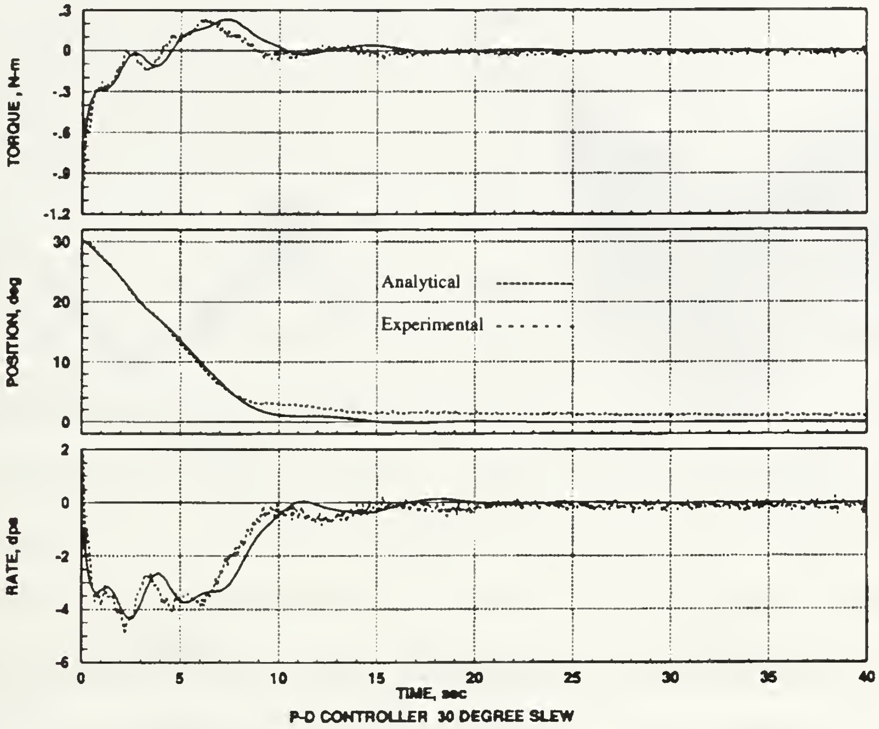

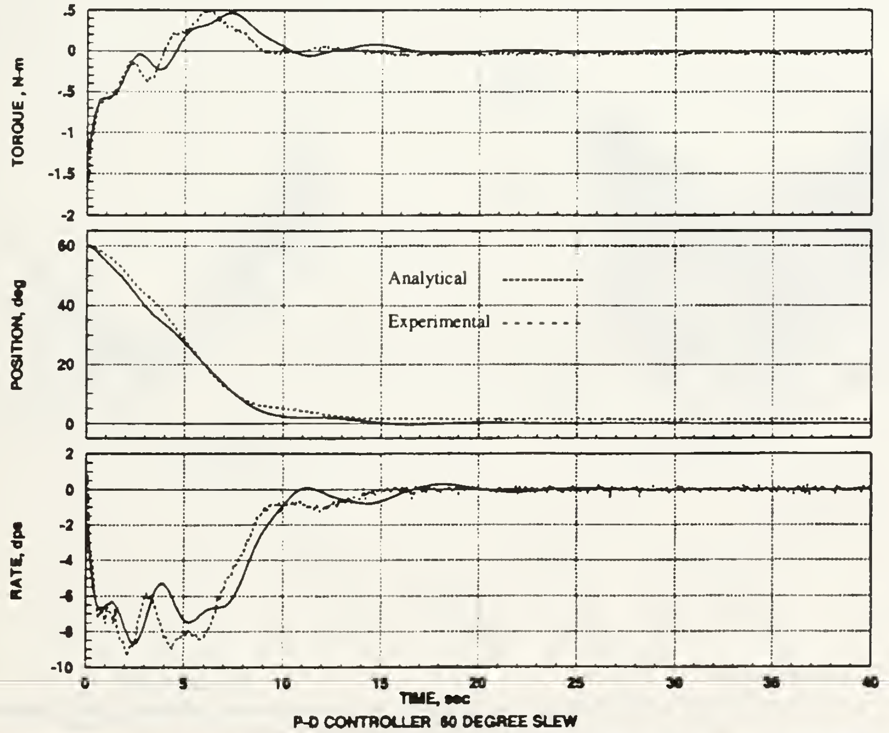

Figures 13 and 14. PD Controller Response

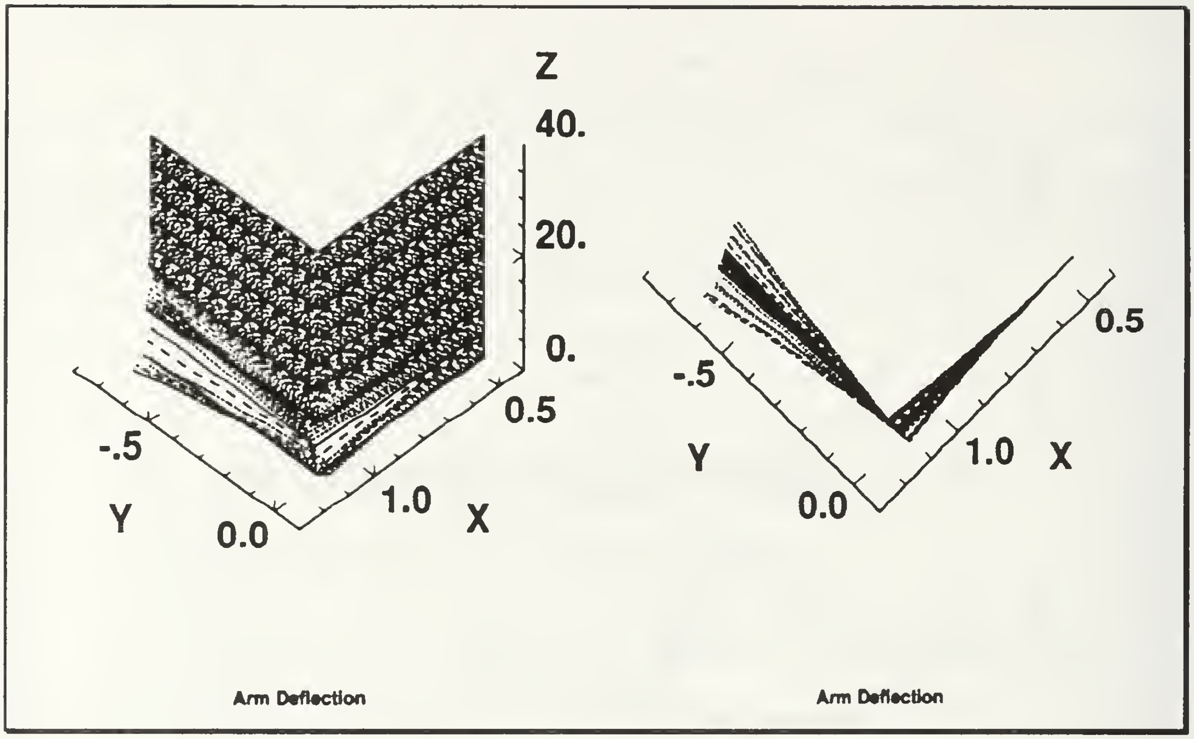

Figure 15. Arm Deflection for a 30° Slew

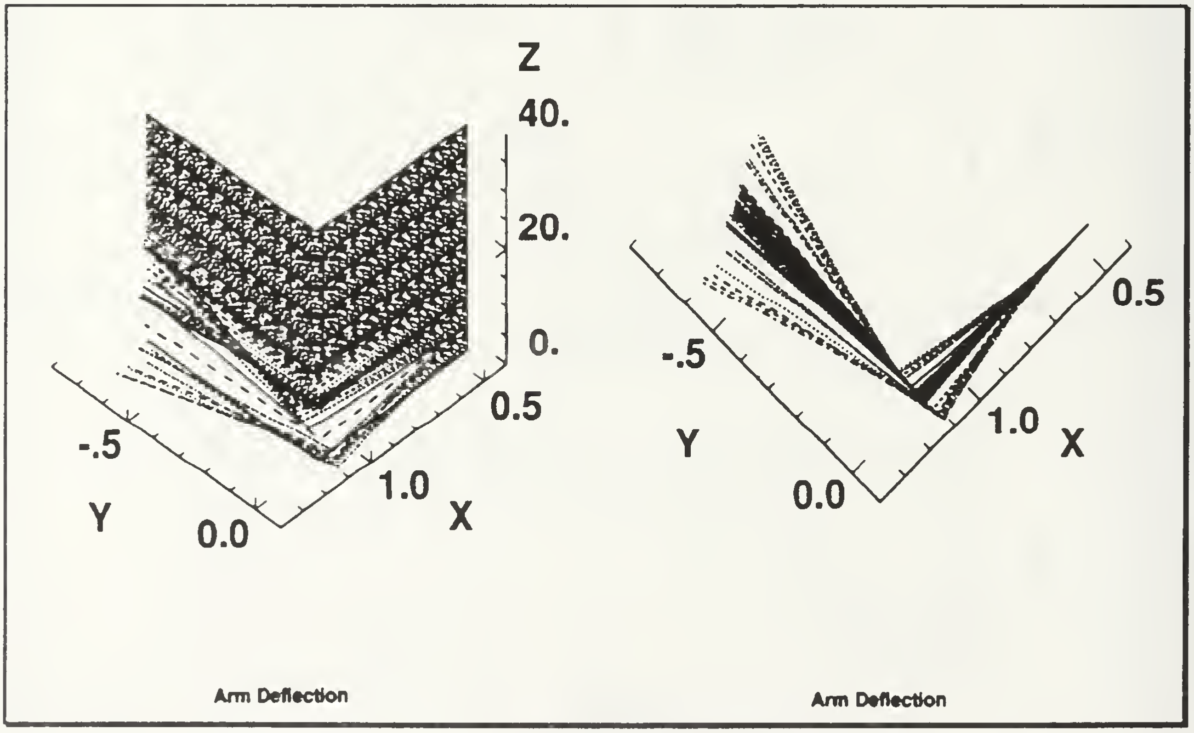

Figure 16. Arm Deflection for a 60° Slew

Looking at the motion in the phase plane gives further insight (Figures 17 and 18). The trajectory deviates significantly from the minimum time parabolic path. It is easy to see that the PD scheme defeats itself by inducing large initial oscillations that must be dealt with as the slew maneuver is performed. This slows the controller response which reduces its performance. Figures 13 and 14 show a substantial control effort when the controller is turned on. This equates to an initial impulse followed by compensating control torques which is undesirable since the initial torque causes large fluctuations in the flexible appendage. The PD controller is also in contradiction to our linear assumptions of small displacements and rates. The initial positive angular rate is a result of anomalies in the AC-100/MATRIX_X output interface. It does not interfere with the analysis of the control system.

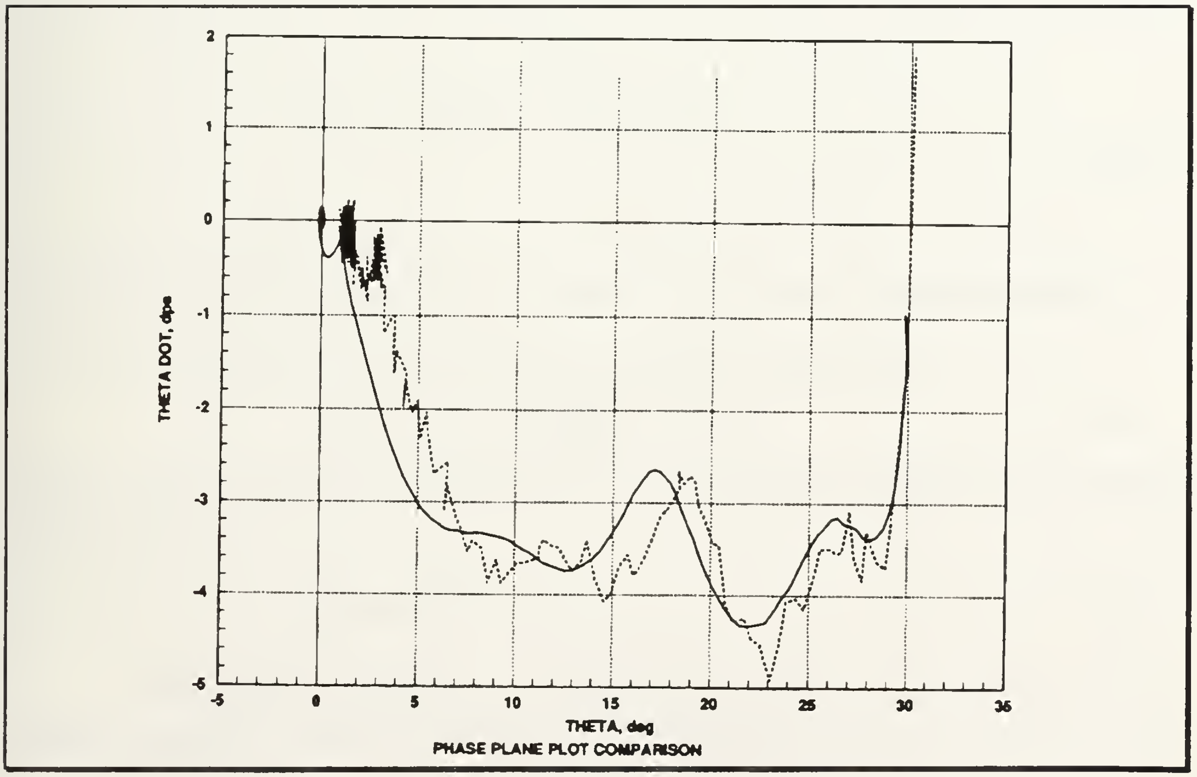

Figure 17. Phase Plot for a 30° Slew

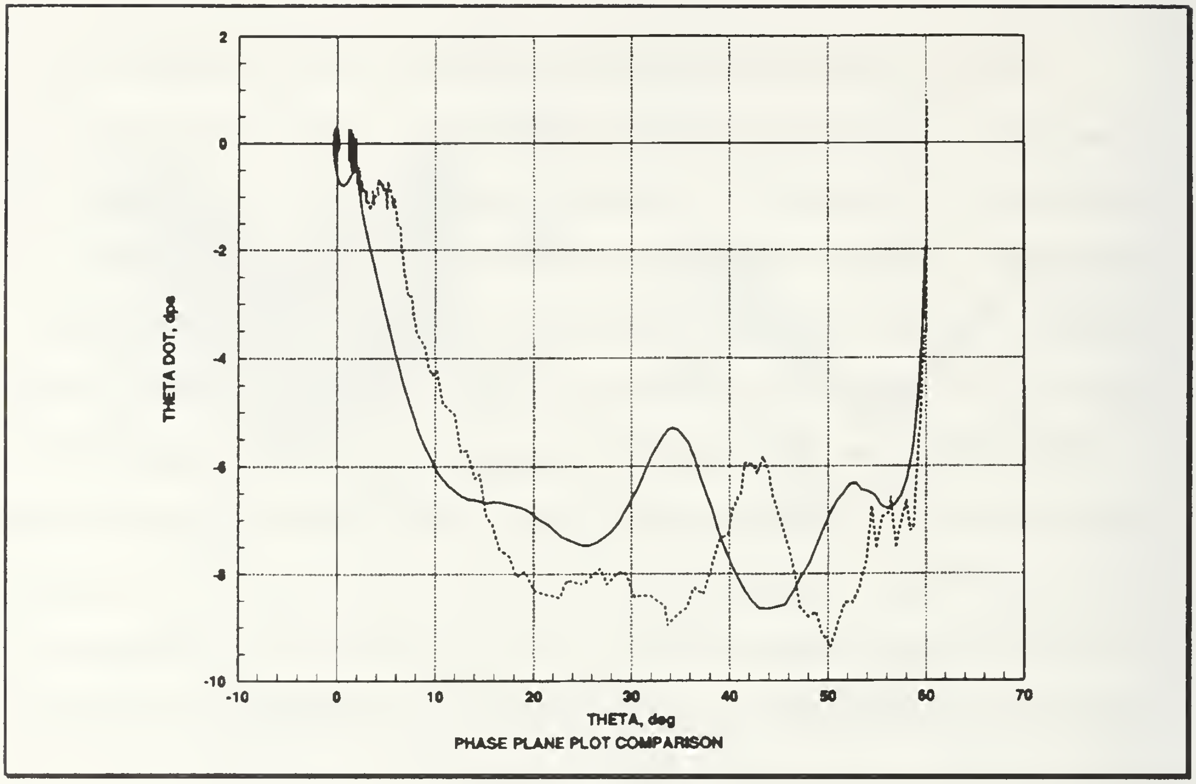

Figure 18. Phase Plot for a 60° Slew

B. OPTIMAL CONTROL

Using rigid body gains in the feedback control loop is too basic and does not produce the optimum slew maneuver. The ultimate goal of this research is to slew as quickly as possible while suppressing the flexible motion as much as possible. By using a linear-quadratic-gaussian (LQG) compensator we can determine feedback gains based on the rigid and flexible dynamics of the system. The LQG compensator is composed of a linear regulator and a Kalman filter estimator making the estimator more robust in the presence of sensor noise. The regulator design assumes full-state feedback. Feeding back all of the states should yield an improvement over classical PD control.

1. Formulation

The optimal gains are calculated by minimizing the cost function [Reference 7]

$$\text{cost} = \int_0^\infty \left(x^T R_{xx} x + u^T R_{uu} u\right) dt \tag{42}$$

where R_{xx} is the state weighting matrix and R_{uu} is the input weighting matrix. To determine the gains, we must first solve the Ricatti equation for $\overline{P}$

$$0 = \overline{P}A + A^T\overline{P} - \overline{P}BR_{uu}^{-1}B^T\overline{P} + R_{xx} \tag{43}$$

where A and B are the system dynamic and control input matrices. The optimal regulator gain is

$$K_R = R_{uu}^{-1}B^T\overline{P} \tag{44}$$

The Kalman filter gains are determined in a similar manner using the duality principle. The state and input weighting matrices, R_{xx} and R_{uu}, are replaced by the state and observation noise intensities, Q_{xx} and Q_{yy}. The linear time-invariant system is

$$\begin{aligned} \dot{x} &= Ax + Bu + Fw \\ y &= Cx + Du + v \end{aligned} \tag{45}$$

where F = the input disturbance matrix

w = the input disturbance

v = the measurement noise

The observation noise intensities are related by the correlation matrices

$$\begin{aligned} E\left(v(t)v^T(\tau)\right) &= Q_{yy}\delta(t - \tau) \\ E\left(Fw(t)v^T(\tau)\right) &= Q_{xy}\delta(t - \tau) \end{aligned} \tag{46}$$

where E is the expected value operator and δ is the delta function. The system is assumed to be driven by only white noise with zero mean value.

2. Implementation

A random disturbance of 0.1 N-m amplitude is assumed so that

$$Q_{xx} = B(0.1)B^T \tag{47}$$

Q_{yy} is a 2X2 matrix with diagonal elements corresponding to noise from the RVDT and the angular rate sensor respectively. These have been experimentally determined as

$$Q_{yy} = \begin{bmatrix} 1E\text{-}7 & 0 \\ 0 & 5E\text{-}6 \end{bmatrix} \tag{48}$$

The off-diagonal elements represent cross-correlation of the sensors noises which are assumed to be zero.

The Kalman filter gains are computed by again solving the Ricatti equation (Equation 42) and applying Equation (43). The gains are now represented in a 14X2 matrix since the inputs to the Kalman filter are the two sensed states, angular position and angular rate.

The estimator is now synthesized using the A, B and C matrices of the dynamic system and the estimator gain, K_E.

$$SOBS = \left[\begin{array}{c|c|c} A - K_E C & -B & K_E \\ \hline C & 0 & 0 \end{array}\right] \tag{49}$$

where SOBS is the estimator system matrix. The estimated states are then fed to the regulator and result in a commanded torque. The block diagram for the system is given in Figure 19.

To obtain numerical values for the estimator and regulator gains, the input and state weighting matrices must be determined. R_{xx} is a 14X14 diagonal matrix assuming that none of the states are cross-correlated. Each term on the diagonal corresponds to a state. The body position and body rate (states 1 and 8) are of primary importance and receive a value of one. The first and second modal coordinates and rates (states 2,3,9 and 10) are also of interest and receive weights of 0.5. The remainder of the states are weighted at 0.1. R_{uu} is a scalar since torque is the only system input and is set at 7 in order to prevent excessive oscillations. Figures 20 and 21 show the analytical and experimental results for a 30° and a 60° slew. The torque prediction is nearly perfect while the position and rate respond faster than predicted. The flexible appendage deformation is illustrated in Figures 22 and 23.

Comparing the estimated states with the modeled states (Figures 24 and 25), it is apparent that problems exist in the state reconstruction. The time required for the estimated states to approach the modeled ones exceeds 25 seconds which is unsatisfactory for real-time control. The body position and rate are the exceptions but those states are the ones fed into the estimator so fast reconstruction is expected. The lack of any sensor information from the flexible nodes severely inhibits the accurate and timely flexible state reconstruction. As a result, the regulator gains are amplifying the errors in the state reconstruction which produces a non-optimal control torque shifting the control bandwidth to the right.

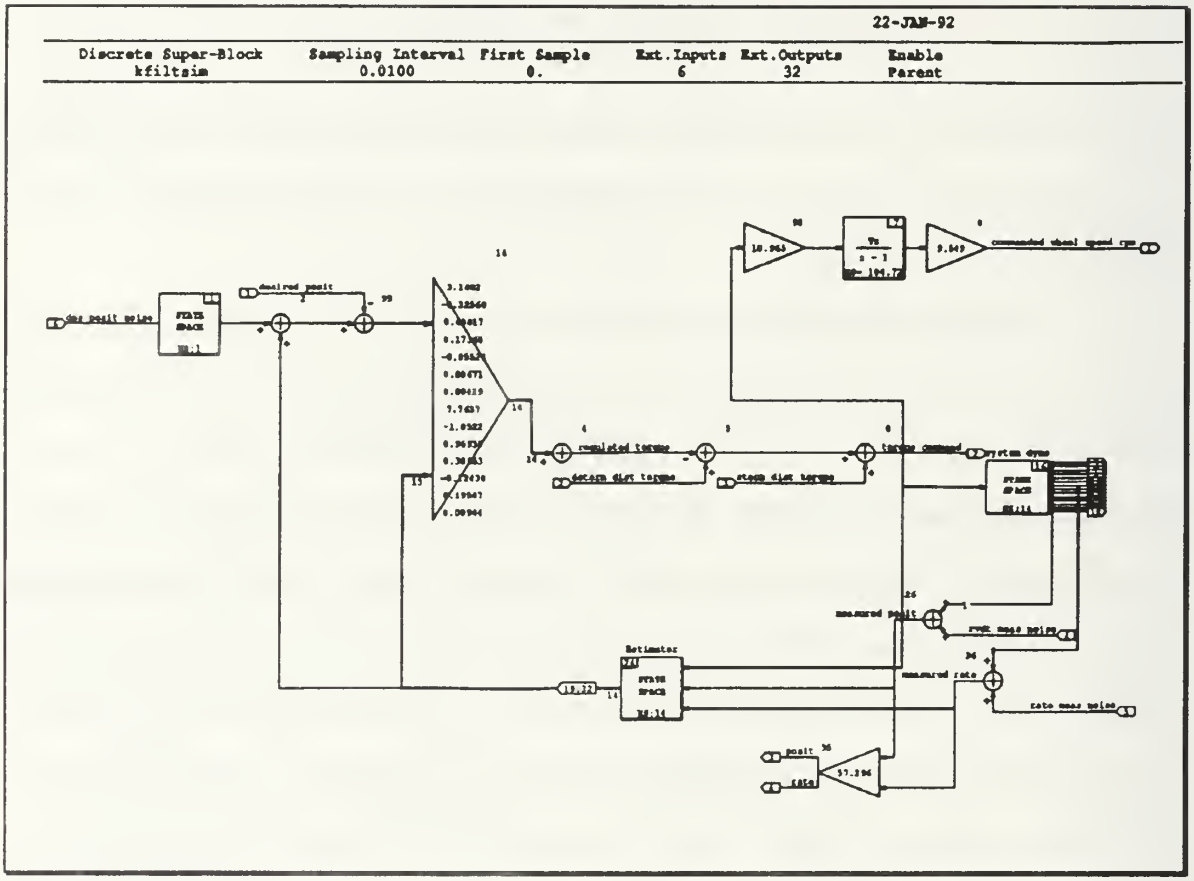
22-JAN-92
Discrete Super-Block
kfiltsim
Sampling Interval
0.0100
First Sample
0.
Ext.Inputs
6
Ext.Outputs
32
Enable
Parent
des posit noise
STATE SPACE
desired posit
3.1682
0.17
0.00671
0.00419
7.7637
-1.0322
0.19947
0.00944
14
15
regulated torque
determ dist torque
stoch dist torque
torque command
system dyns
STATE SPACE
10.965
9.849
commanded wheel speed rpm
measured posit
measured rate
rate meas noise
Estimator
STATE SPACE
19.22
posit
rate
57.296

Figure 19. LQG Controller Block Diagram

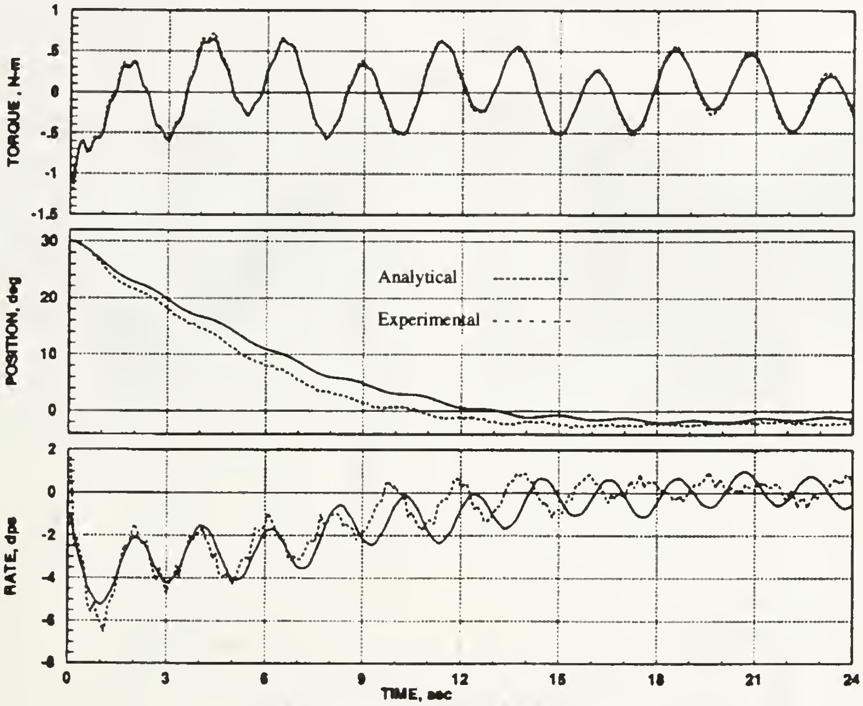

OPTIMAL CONTROLLER 30 DEGREE SLEW

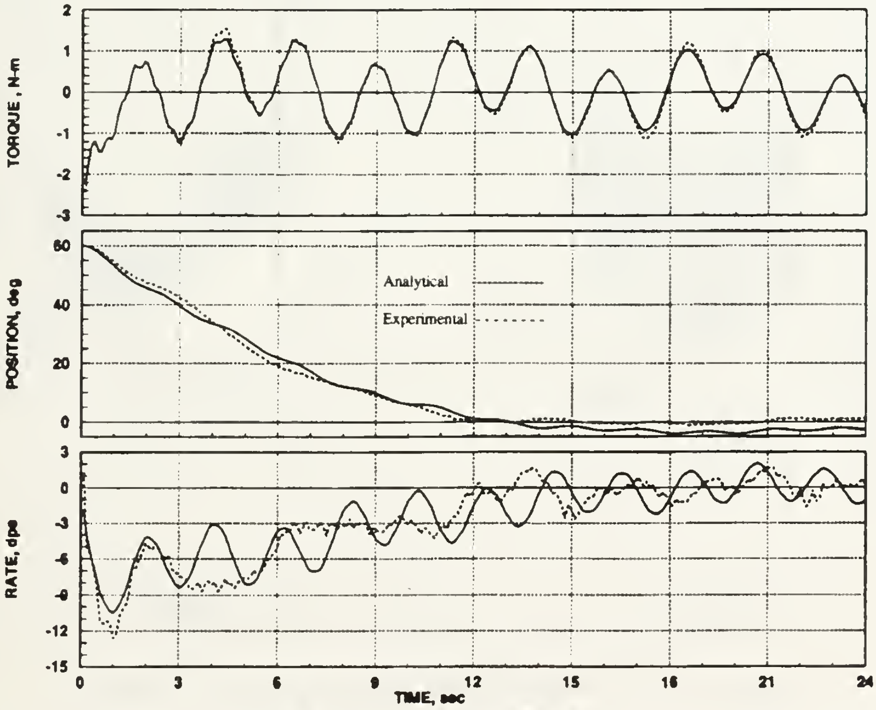

OPTIMAL CONTROLLER 60 DEGREE SLEW

Figures 20 and 21. LQG Response

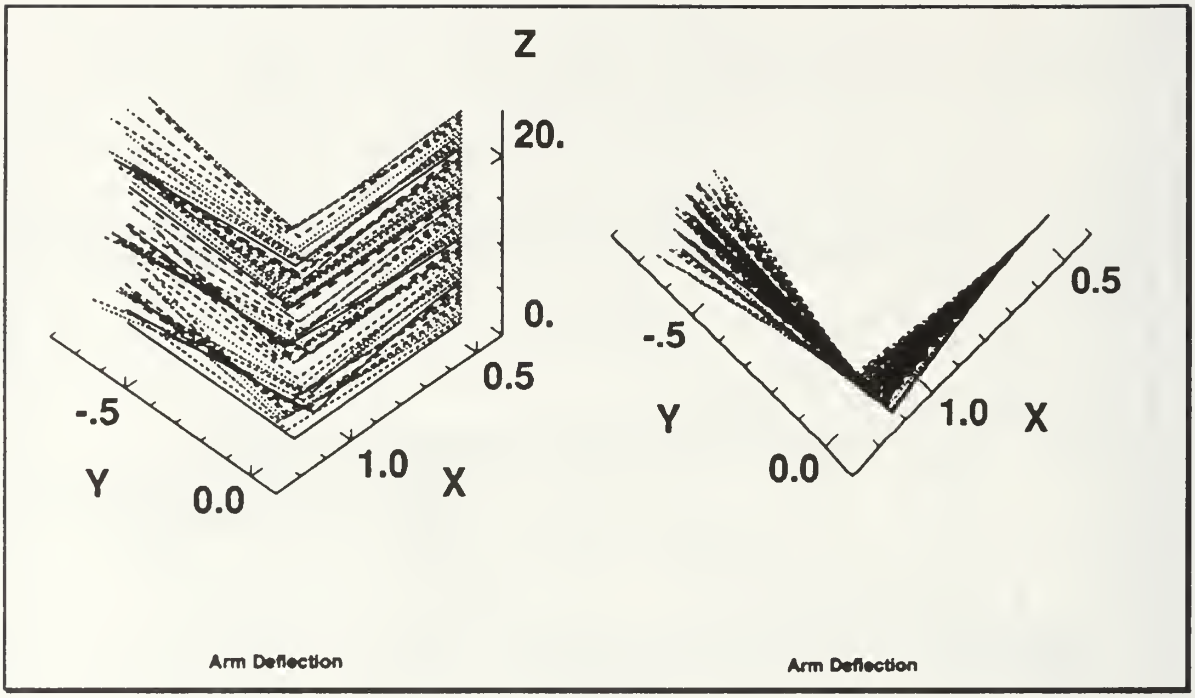

Figure 22. Arm Deflection for a 30° Slew

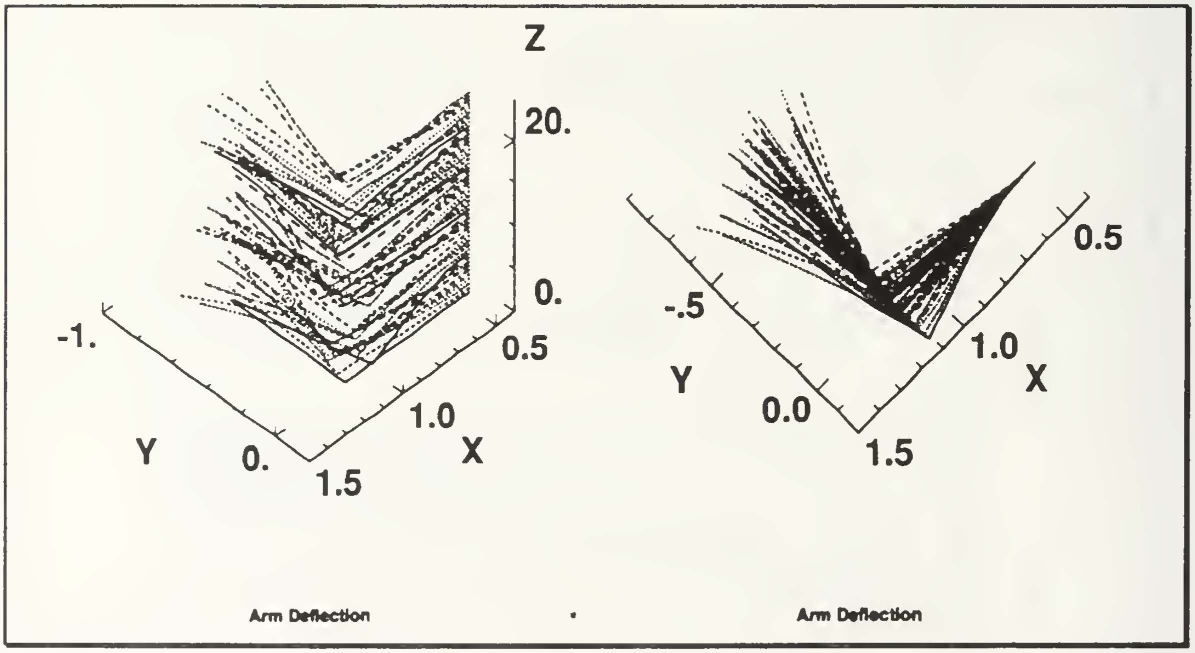

Figure 23. Arm Deflection for a 60° Slew

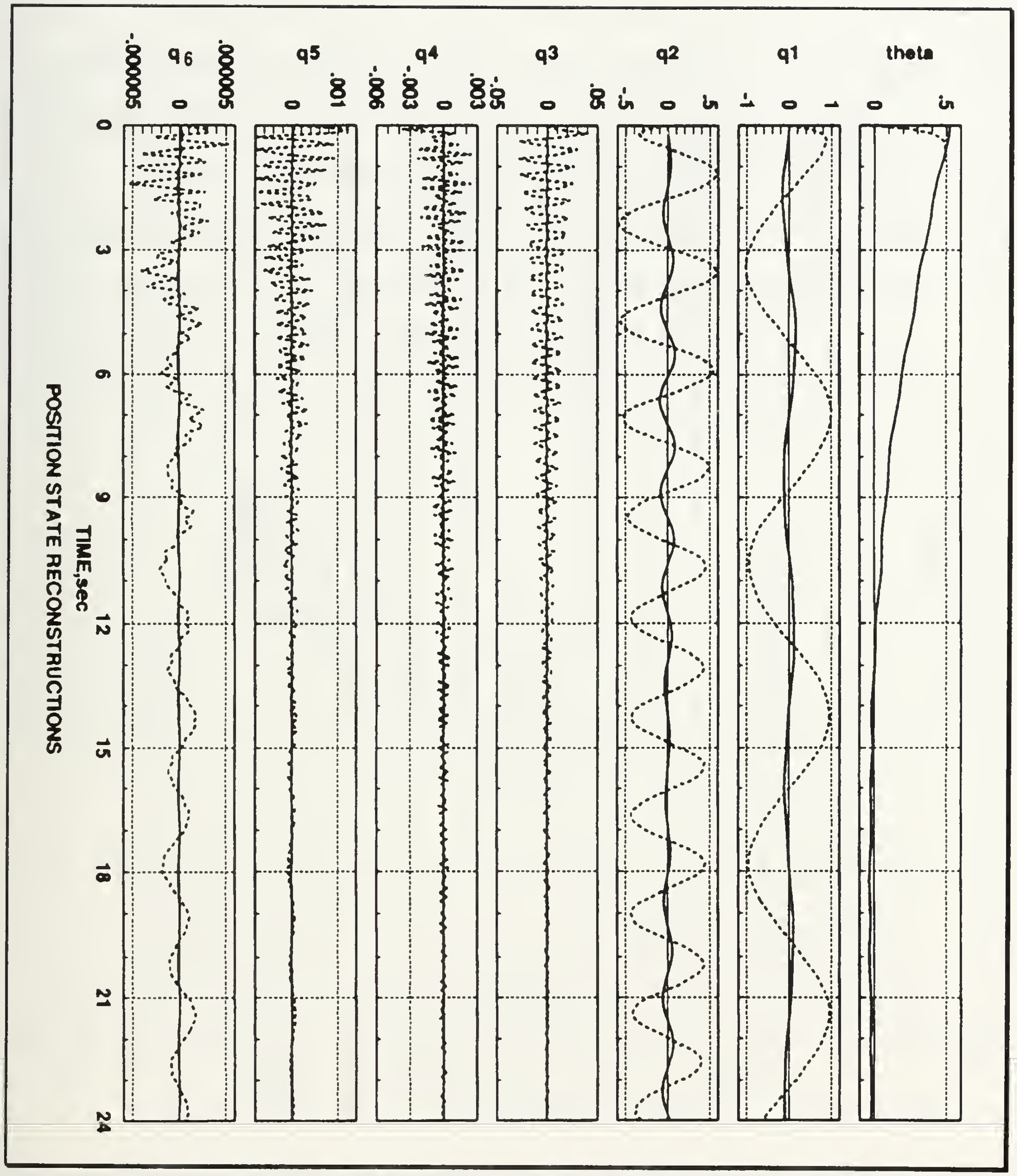

Figure 24. Reconstructed Positions

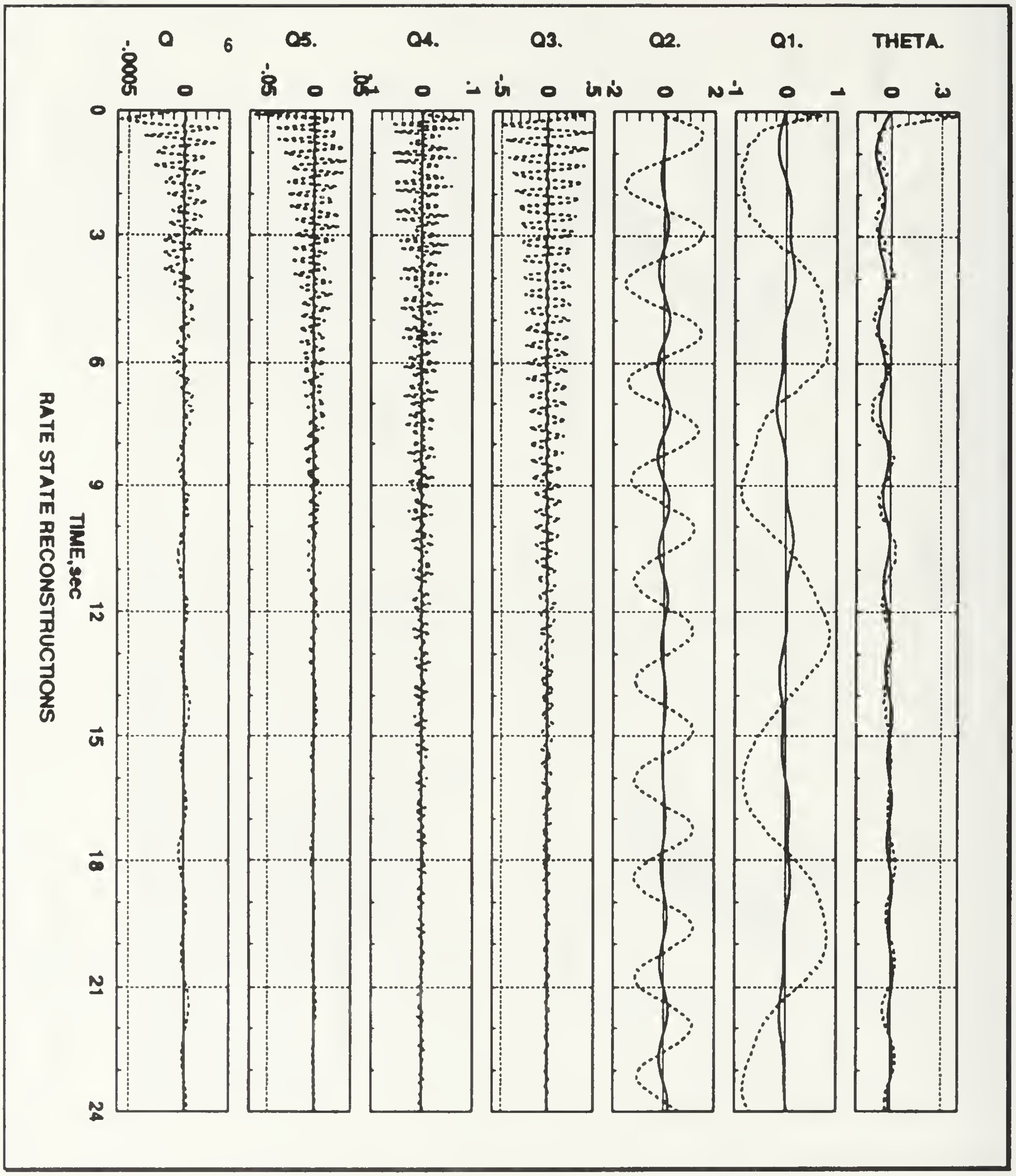

Figure 25. Reconstructed Rates

The phase plane motion is shown in Figures 26 and 27. Poor state reconstruction accounts for the undesirable phase space motion. By adjusting Q_{xx} and R_{uu}, the trajectories can be manipulated so that the control bandwidth is below the fundamental frequency of the flexible appendage so as not to stimulate the flexible modes.

Achieving adequate state reconstruction is difficult (if not impossible) at this point without at least one flexible state available. An overhead camera system developed by Stan Schneider at Real-Time Innovations, Inc.,will be used to obtain position and rate for one or more nodes in the future.

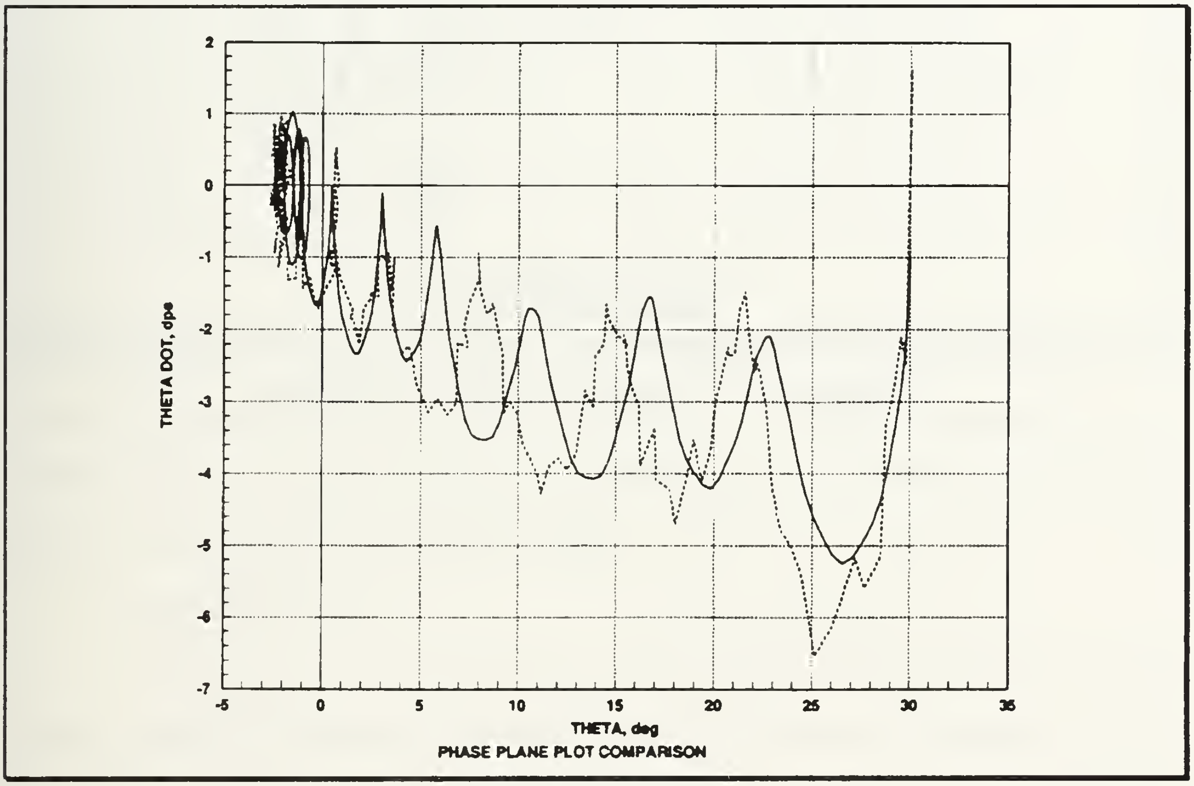

Figure 26. Phase Plot for a 30° Slew

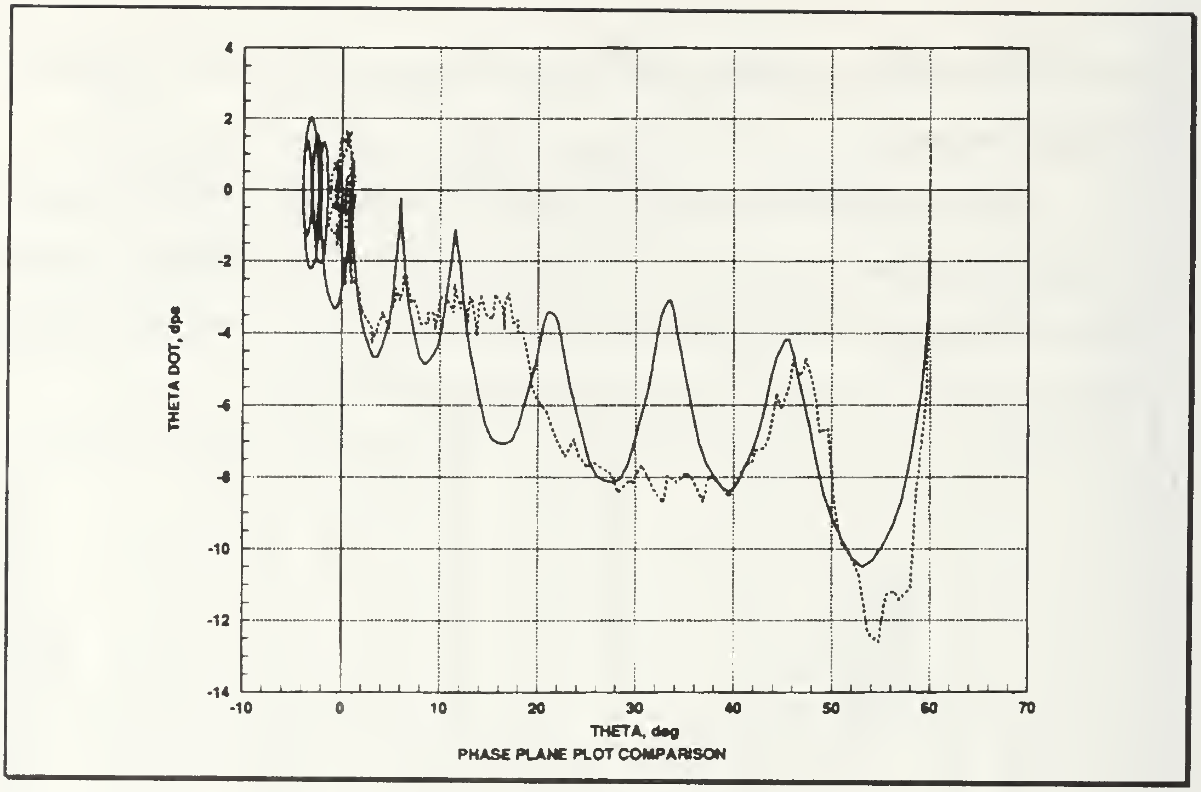

Figure 27. Phase Plot for a 60° Slew

C. CLASSIC BANG-BANG CONTROL

1. Formulation

The drawbacks of the PD controller lead to the investigation of other techniques. One is the classical Bang-Bang controller which gives the minimum time maneuver for a rigid body. It employs the well known position plus rate feedback law

$$u = -N \operatorname{sgn}[S] \qquad (50)$$

$$S = \theta + \frac{\dot{\theta}|\dot{\theta}|}{2N}$$

N = constant saturation torque

to apply torques to the rigid body. From an initial point in the phase plane, the rigid body trajectories theoretically follow parabolas into the origin producing a minimum time maneuver for the given saturation level. When flexibility is added to the system the behavior changes.

2. Implementation

Figure 28 is the block diagram for the system. The experimental results exhibit an even greater level of chatter than was analytically predicted (Figures 29 and 30). The position and rate trajectories are in good agreement despite the chatter and the inability of the system to keep up with the rapid switching. The torque level chosen for these results is 0.3 N-m. This shows the tradeoff that must be considered in the Bang-Bang scheme. The torque level must be high enough to complete the maneuver in a reasonable amount of time while being low enough to avoid unreasonable oscillations in the flexible appendage. Figures 29 and 30 indicate that the torque required to be comparable with the PD slew time induces unacceptable oscillations in the arm which tend to resonate when the desired position is reached. Figures 31 and 32 also show undo arm oscillations for this torque level. A lower torque level (0.2 N-m) reduces these oscillations significantly. However, the maneuver time is in excess of 20 seconds for a 30° slew which is much slower than the PD slew time.

Figures 33 and 34 show the comparison between the analytical and the experimental results in the phase plane for a fixed rotational inertia subject to the same saturation level. It is apparent that the trajectory behavior is altered and the maneuver takes more time. As the saturation level is raised the controller bandwidth increases driving the flexible modes to a greater extent. To overcome this a torque shaping model can be used. This process is described in the next section.

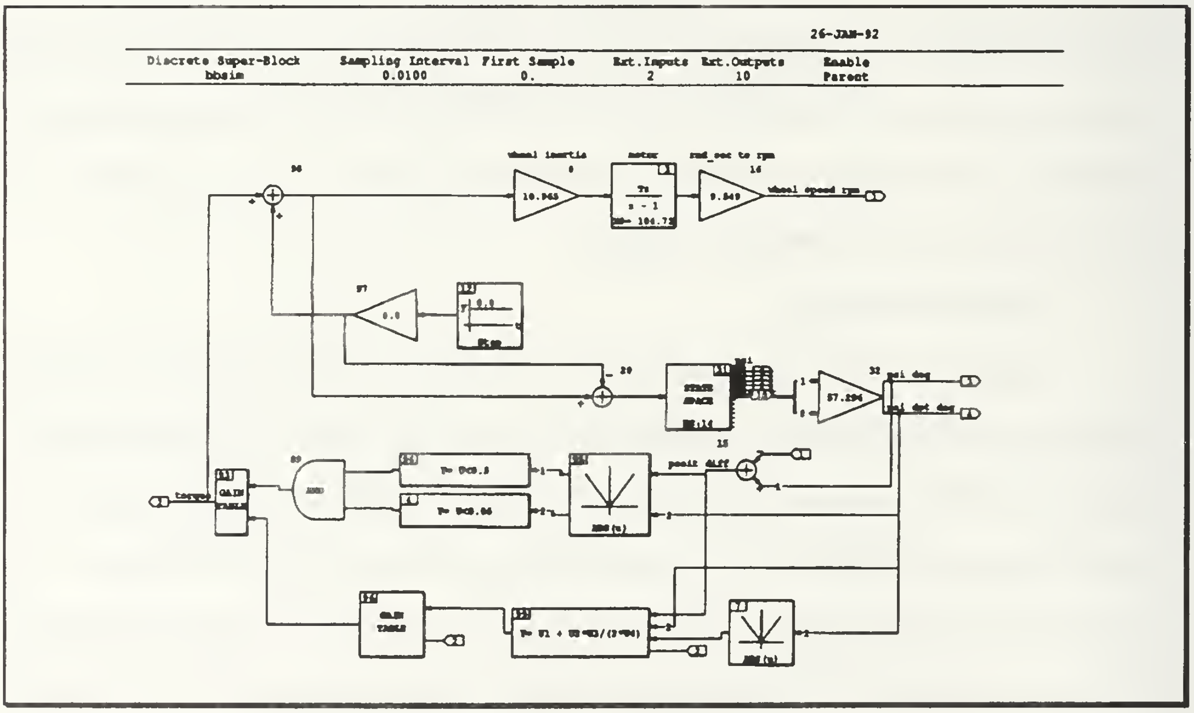
26-JAN-92
Discrete Super-Block
bbsim
Sampling Interval
0.0100
First Sample
0.
Ext.Inputs
2
Ext.Outputs
10
Enable
Parent
wheel inertia
motor
rad_sec to rpm
wheel speed rpm
torque
GAIN TABLE
STATE SPACE
57.296
psi deg
psi dot deg
posit diff

Figure 28. Bang-Bang Block Diagram

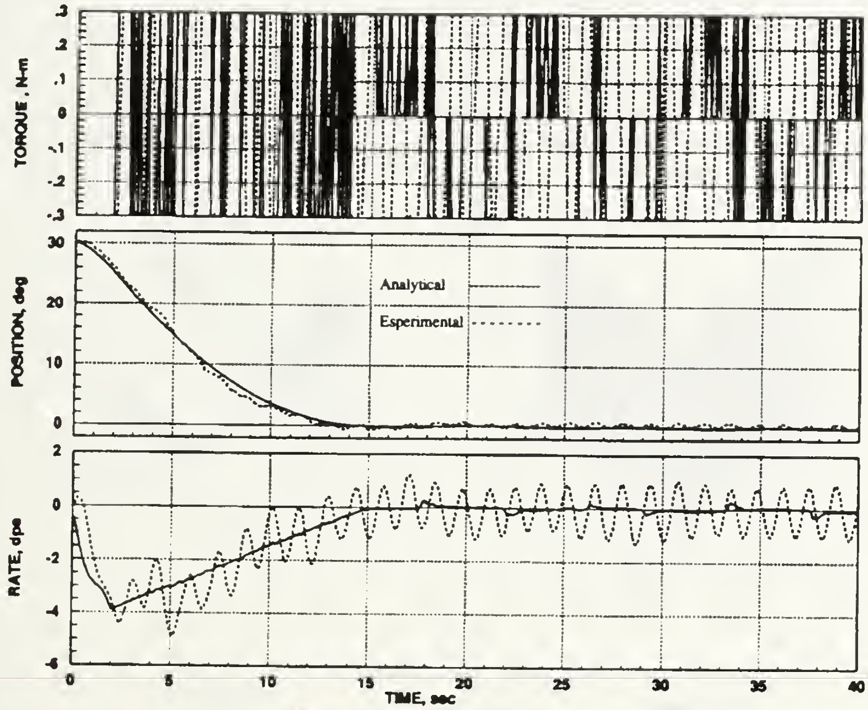

BANG-BANG 30 DEGREE SLEW

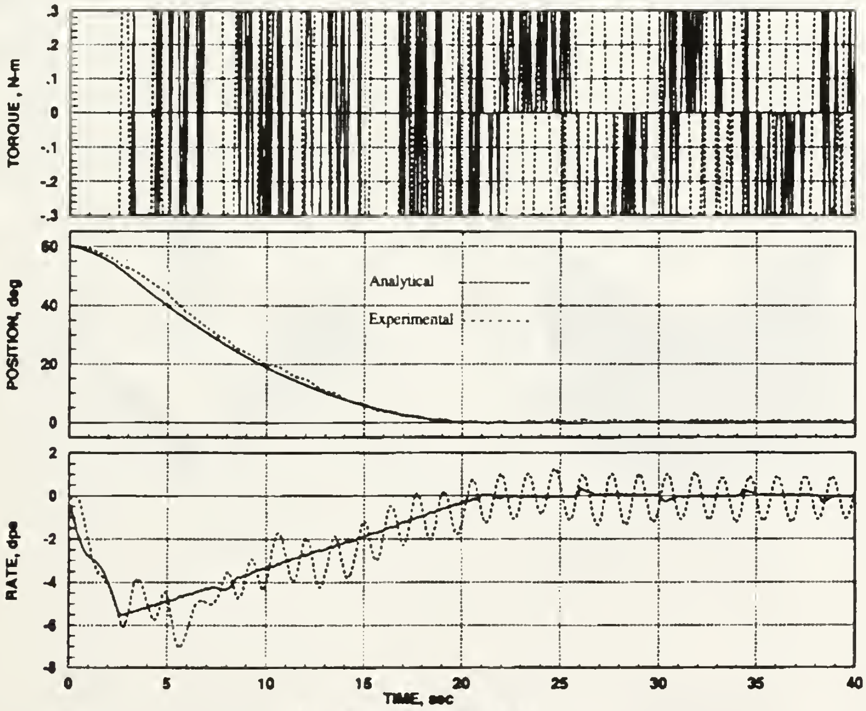

BANG-BANG 60 DEGREE SLEW

Figure 29 and 30. Bang-Bang Response

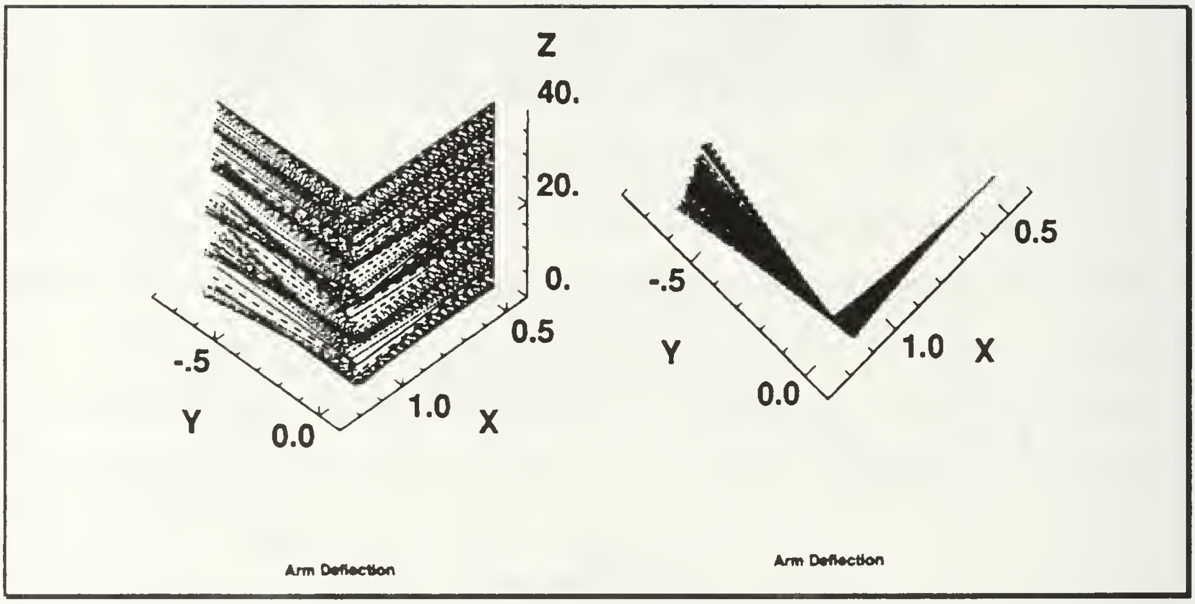

Figure 31. Arm Deflection for a 30° Slew

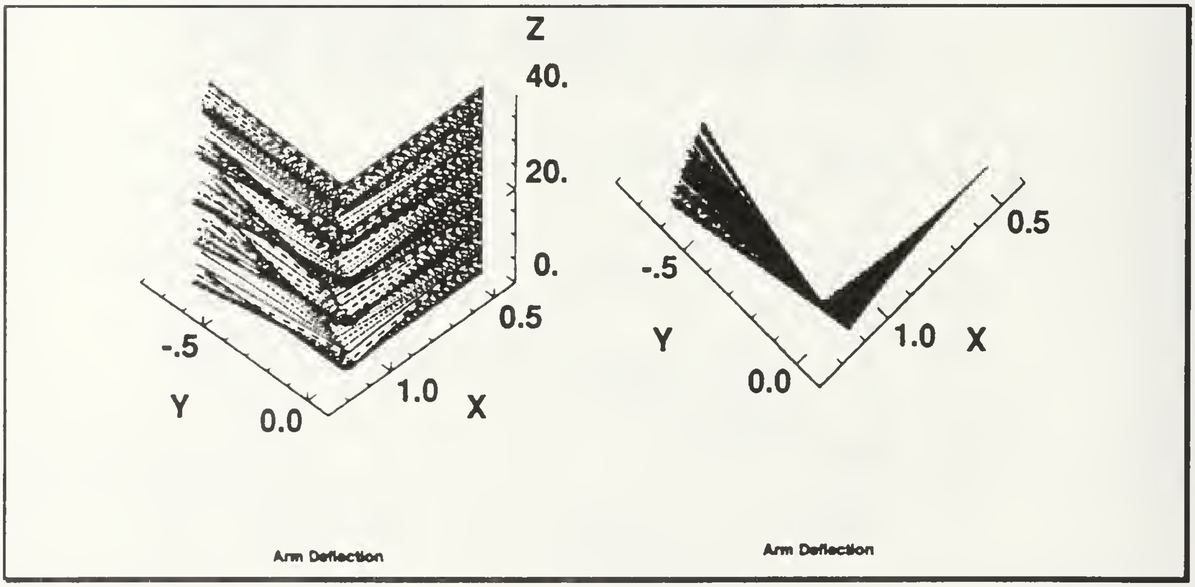

Figure 32. Arm Deflection for a 60° Slew

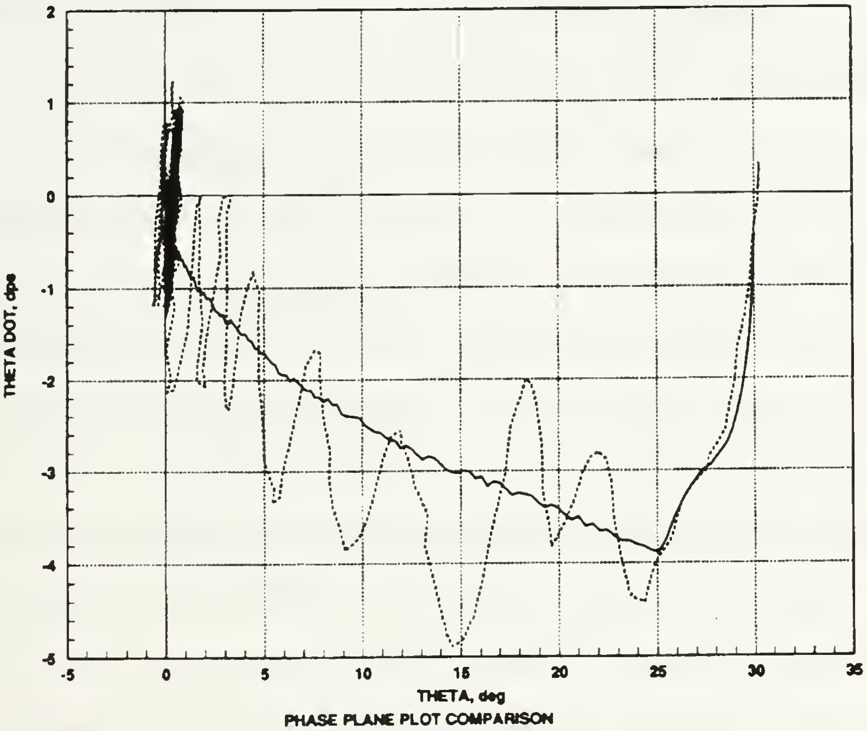

Figure 33. Phase Plot for a 30° Slew

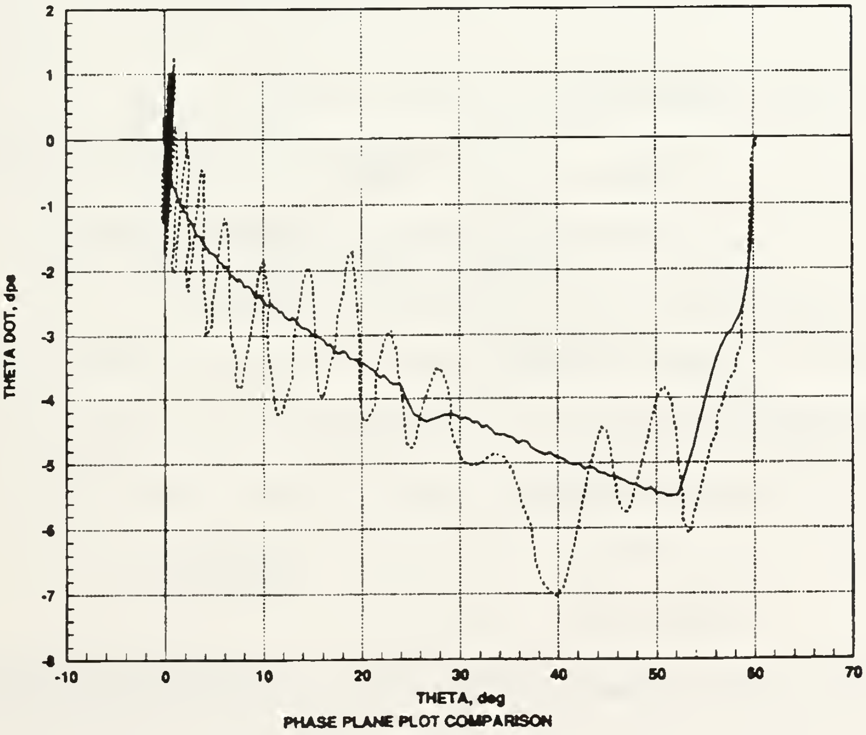

Figure 34. Phase Plot for a 60° Slew

D. TORQUE SHAPING

1. Sinusoidal

The initial control effort required in the PD scheme imparts an unacceptable jolt to the system. To counter this, we need to smooth out the transition from the pre-control steady-state to the initial torque command. Also, the PD controller employs large angle maneuvers with significant angular rate changes. This is not consistent with the assumptions made in our linear model. One method used to address these problems was introduced in Reference 2 Instead of controlling the position difference and angular rate to zero, the torque shaping technique builds reference position and rate trajectories which produce pre-designed torque profiles. To smooth out the initial spike in the PD control effort, we want to model a sinusoidal torque that is smooth and continuous. The block diagram is given in Figure 35.

$$T_c = A\sin\frac{2\pi t}{P} \qquad (51)$$

where A = Peak amplitude of the control effort

P = Desired slew time (period of the sinusoid)

The control torque relates to the wheel and body torques as

$$I_W\dot{\Omega} = -T_c = I^0_{zz}\ddot{\theta} \qquad (52)$$

and the feedback control law is

$$u = -k(\theta_e + \tau\dot{\theta}_e) \qquad (53)$$

$$\theta_e = \theta - \theta_{ref}$$

$$\dot{\theta}_e = \dot{\theta} - \dot{\theta}_{ref}$$

The reference curves must be in terms of the body position and rate since these are the only states being sensed. They are derived by putting Equation (52) in terms of the body's acceleration and performing successive integrations.

$$\ddot{\theta} = -\frac{A}{I^0_{zz}}\sin\frac{2\pi t}{P} \tag{54}$$

$$\dot{\theta} = \frac{AP}{2\pi I^0_{zz}}\left[\cos\frac{2\pi t}{P} - 1\right] \tag{55}$$

$$\theta = \frac{AP}{2\pi I^0_{zz}}\left[\frac{P}{2\pi}\sin\frac{2\pi t}{P} - t\right] \tag{56}$$

Applying the boundary conditions $\theta = \Delta\theta$ at t=0 and $\theta = 0$ at t=10 for a ten second slewing time and differentiating successively, the reference position and rate are

$$\theta_{ref} = \Delta\theta\left[1 + \frac{1}{P}\left(\frac{P}{2\pi}\sin\frac{2\pi t}{P} - t\right)\right] \tag{57}$$

$$\dot{\theta}_{ref} = \frac{\Delta\theta}{P}\left[\cos\frac{2\pi t}{P} - 1\right] \tag{58}$$

where $\Delta\theta$ = Difference between current and desired position

The body acceleration is given by

$$\ddot{\theta}_{ref} = -\frac{2\pi\Delta\theta}{P^2}\sin\frac{2\pi t}{P} = -\frac{A}{I^0_{zz}}\sin\frac{2\pi t}{P} \tag{59}$$

The reference curves are shown in Figure 36. By manipulating Equation (44), we can examine the tradeoffs between control effort and slewing time with respect to slew angle. The amplitude of the control effort is

$$A = \frac{2\pi I^0_{zz}\Delta\theta}{P^2} \tag{60}$$

and the slew time is given by

$$P = \sqrt{\frac{2\pi\Delta\theta}{A}} \tag{61}$$

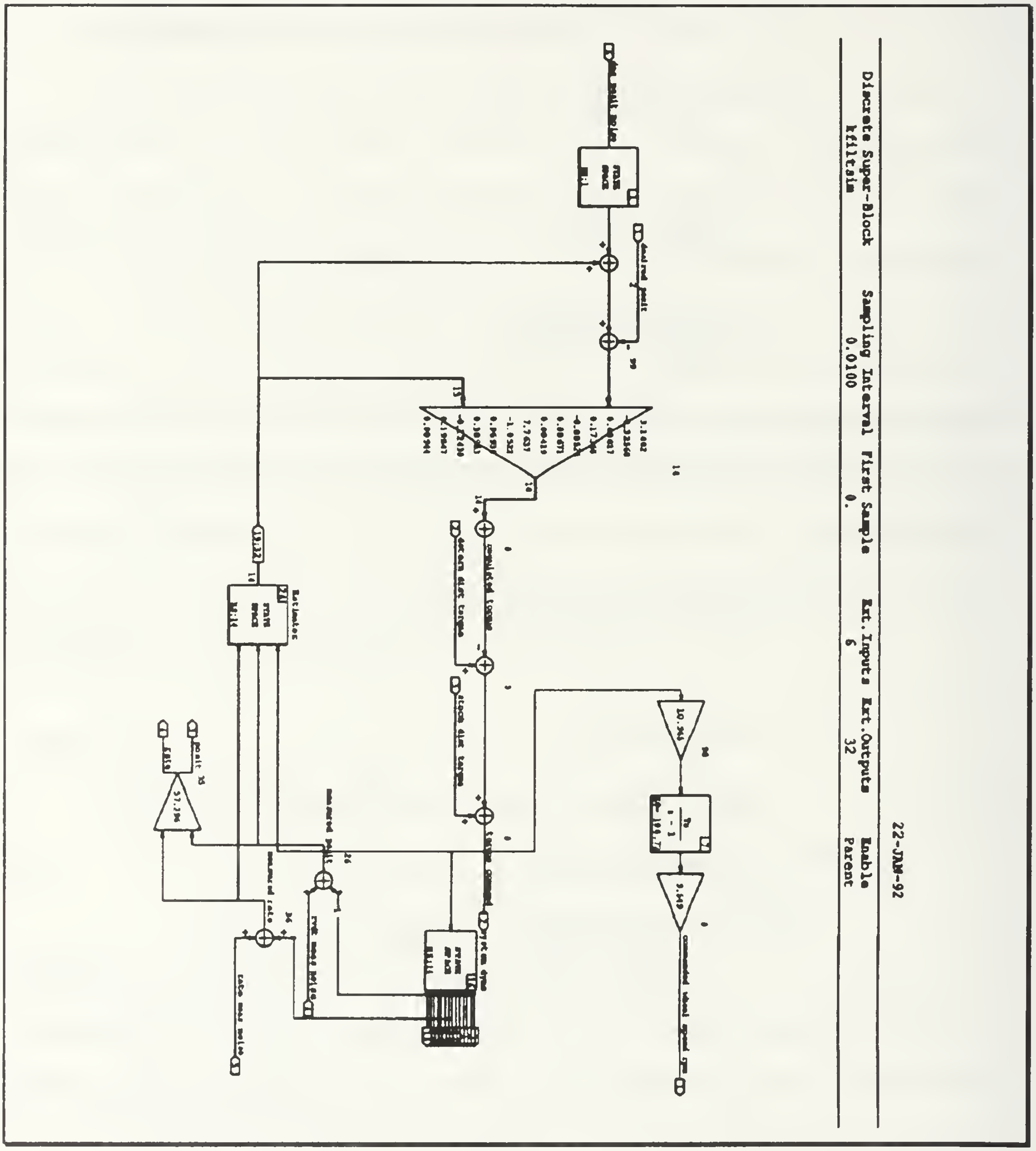
Discrete Super-Block
kfiltsim
Sampling Interval
0.0100
First Sample
0.
Ext. Inputs
6
Ext. Outputs
32
Enable
Parent
22-JAN-92
desired posit
Estimator
STATE SPACE
computed torque
torque command
measured posit
measured rate
rate meas noise
57.296
commanded wheel speed

Figure 35. Sinusoidal Torque Profile Block Diagram

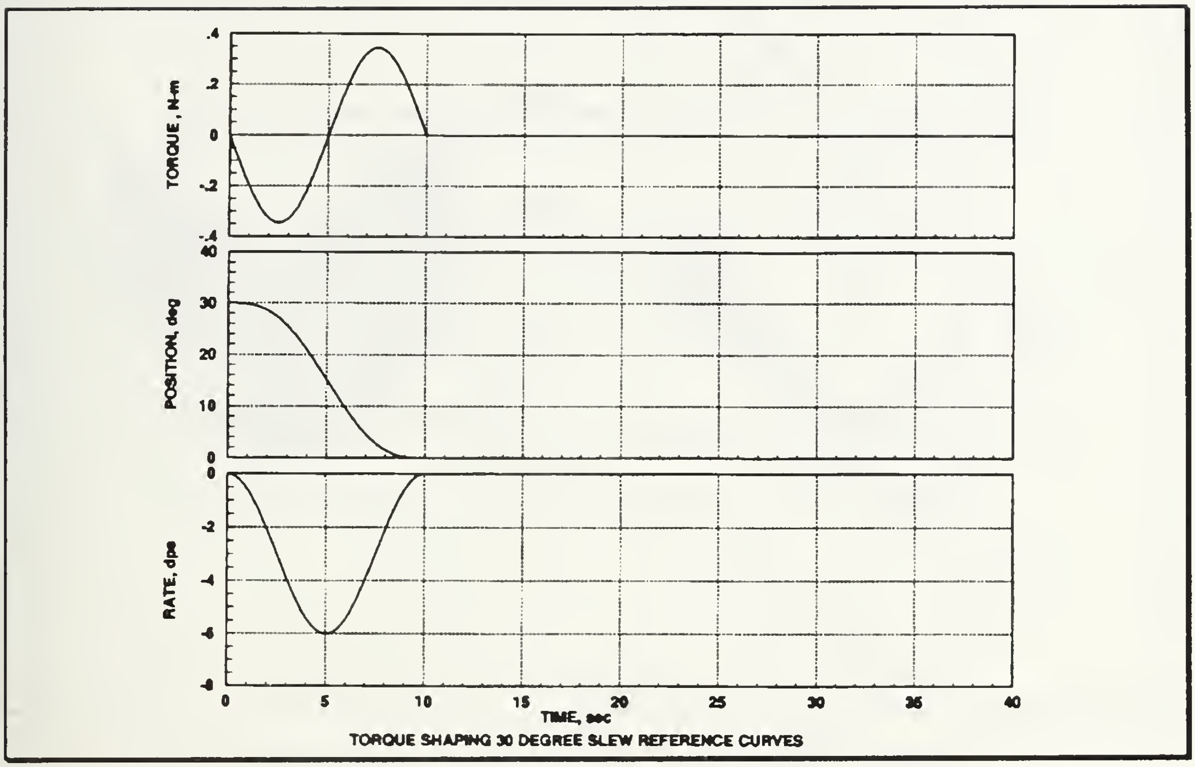

Figure 36. Reference Curves

By pre-determining the shape and amplitude of the control effort, the slew time required for a rigid body can be determined. By implementing these reference curves into our flexible model, an analytical prediction can be developed to approximate the ensuing motion. Figures 37 and 38 compare the predicted motion and the experimental results using the same gains determined in the PD control law during a 30° and 60° slew. Figures 39 and 40 are the arm deflections for the same events. Notice the deflection is slightly less than that of the PD controller for the same slew angle while the time required to complete the maneuver is almost the same.

So far, the PD and the Sinusoidal Torque Shaping schemes seem to do the job equally as well with neither showing a clear advantage over the other. Figures 41 and 42 show the phase plane motion for the Torque Shape controller. The curve is very similar to those observed for rigid body systems where the minimum time curve is a parabola. Comparing these to Figures 17 and 18 shows

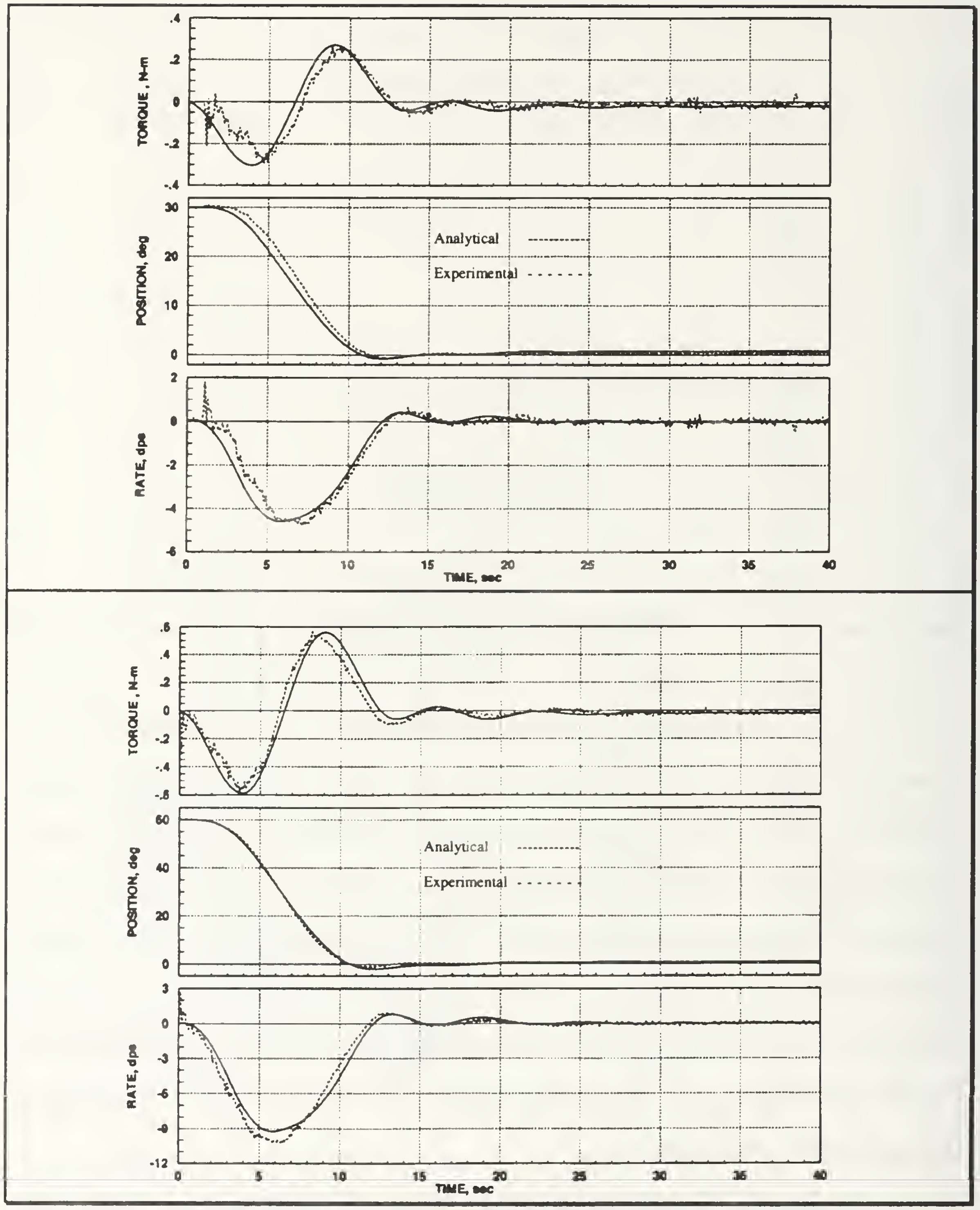

Figures 37 and 38. Sinusoidal Torque Shape Response

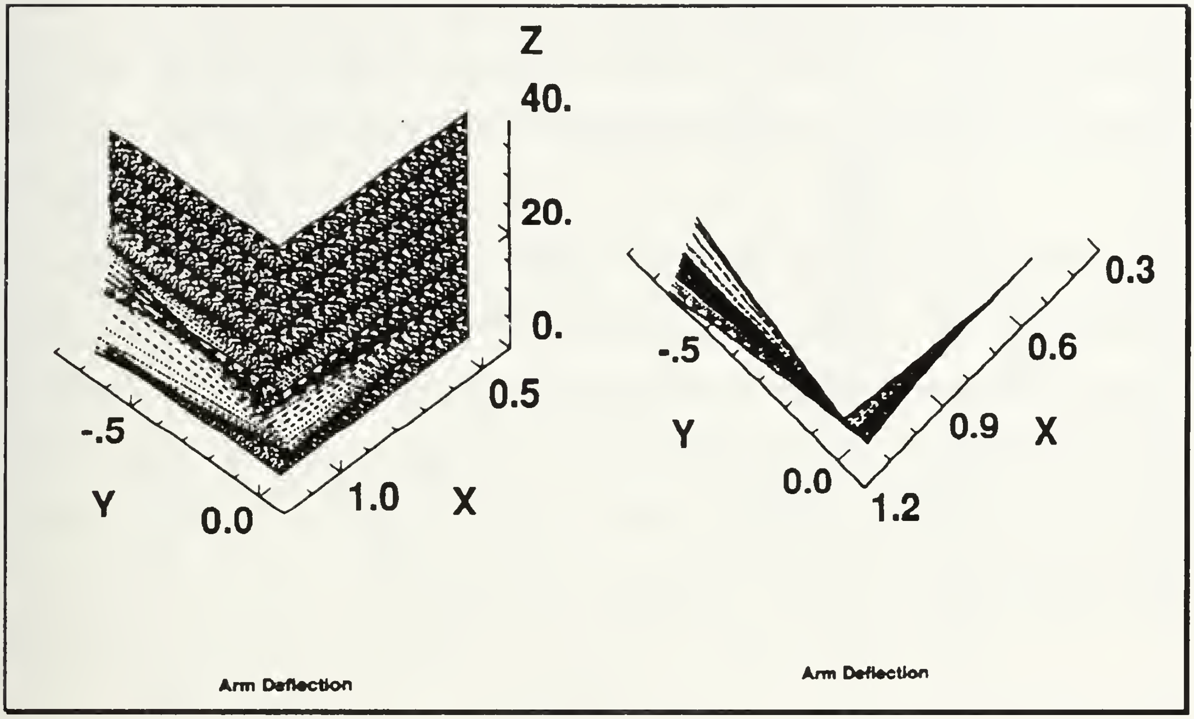

Figure 39. Arm Deflection for a 30° Slew

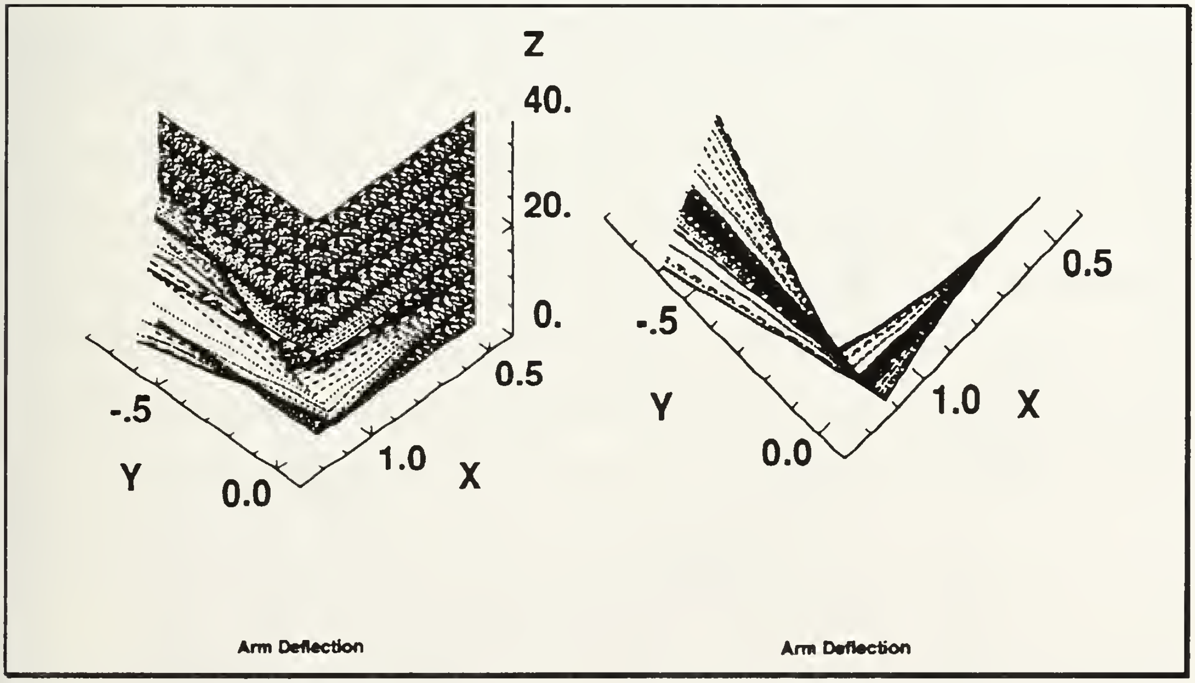

Figure 40. Arm Deflection for a 60° Slew

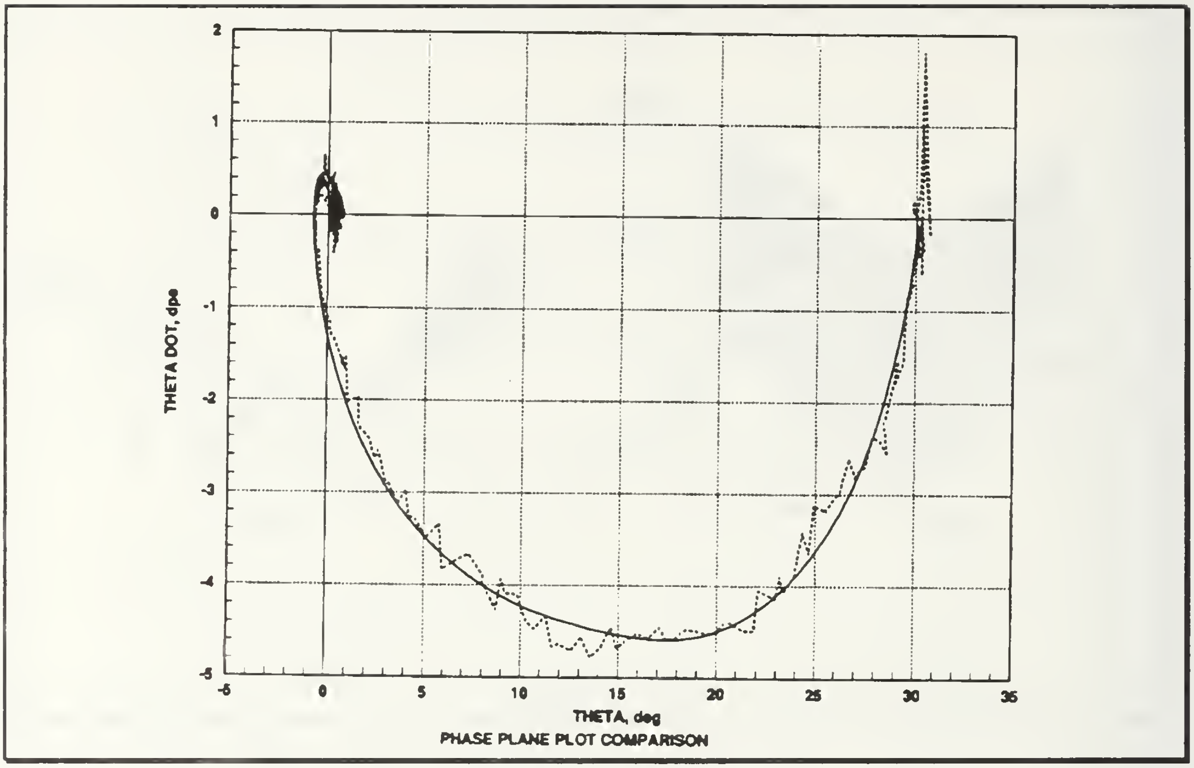

Figure 41. Phase Plot for a 30° Slew

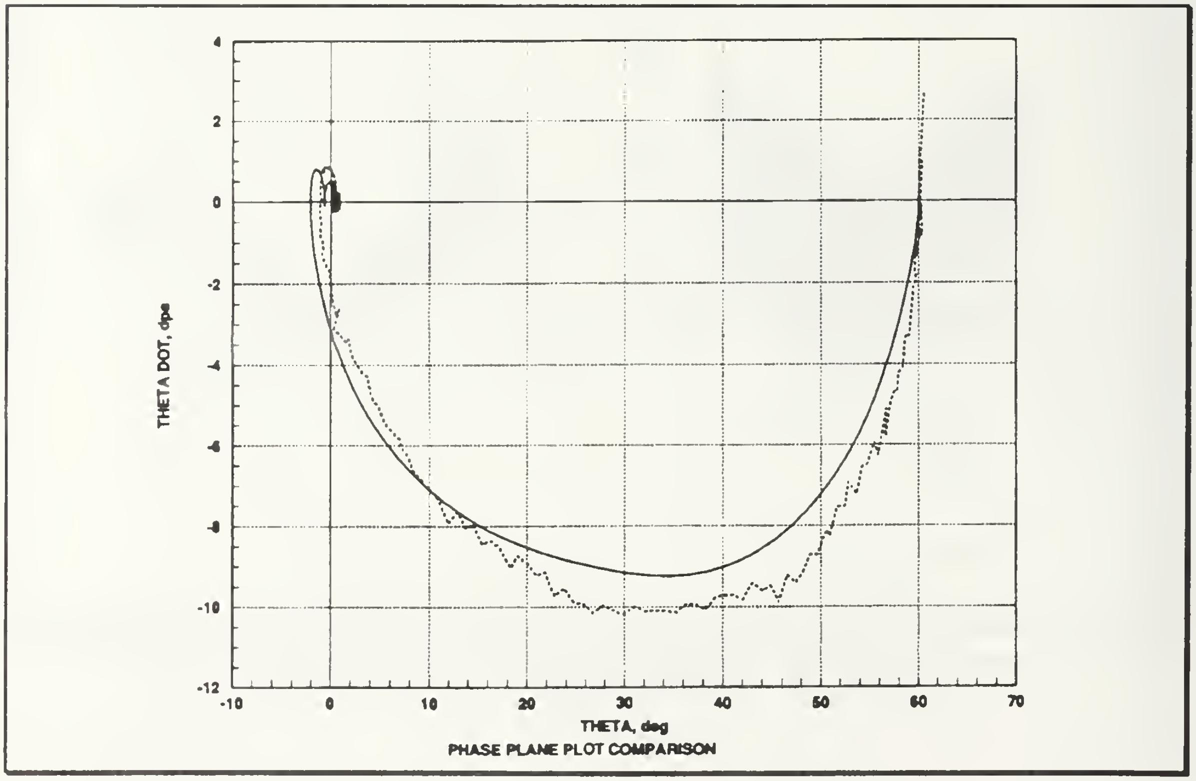

Figure 42. Phase Plot for a 60° Slew

the clear flexible interaction associated with the PD controller. This results from the large initial control effort and subsequent efforts to alleviate the ensuing disturbances to the system.

Using the torque shaping instead of the PD, we gain two clear advantages. First, the initial torque command is significantly reduced. The peak torque required in the PD controller is close to three times that required for the torque shaped case. Second, the position and rate differences used by the controller remain small so that the linear model derived earlier is justified. The PD controller uses large angle feedback which contradicts the small deflection assumption used in our model.

2. Pseudo-Square

The classical Bang-Bang scheme has two major flaws. First, when applied to the flexible model, it switches frequently. This causes many discontinuities resulting in the chattering evident from previous results. Second, the rise time associated with the maneuver cannot be realized by the reaction wheel. Reference 2 describes a scheme for conducting near minimum time maneuvers by rounding off the corners of the Bang-Bang square wave torque and following this modified profile. This gives the wheel time to respond to the commanded torque assuming a realistic rise time is set. The resulting maneuver is a near-minimum-time slew which does not over-excite the flexible modes. The block diagram for the system is shown in Figure 46.

The torque shaping is accomplished by combining sections of a sine wave with horizontal line sections. The sine function has a period of four times the specified rise time. The general control law is

$$u = -u_{max}\, f(t_r,t,P) = I_{zz}^{0}\ddot{\theta} \tag{62}$$

where u_{max} = maximum desired torque level

t_r = specified rise time

The function $f(t_r,t,P)$ is given by

$$f = \left\{ \begin{array}{ll} \sin \dfrac{\pi t}{2t_r} & 0 \le t \le t_r \\ 1 & t_r \le t \le \dfrac{P}{2} - t_r \\ \sin \dfrac{\pi\left(t - \dfrac{P}{2} - 2t_r\right)}{2t_r} & \dfrac{P}{2} - t_r \le t \le \dfrac{P}{2} + t_r \\ -1 & \dfrac{P}{2} + t_r \le t \le P - t_r \\ \sin \dfrac{\pi(t - P + 4t_r)}{2t_r} & P - t_r \le t \le P \end{array} \right\} \qquad (63).$$

The resulting torque model is shown in Figure 44 for a 30° slew. Successive integration yields the angular position and angular rate reference curves also in Figure 44.

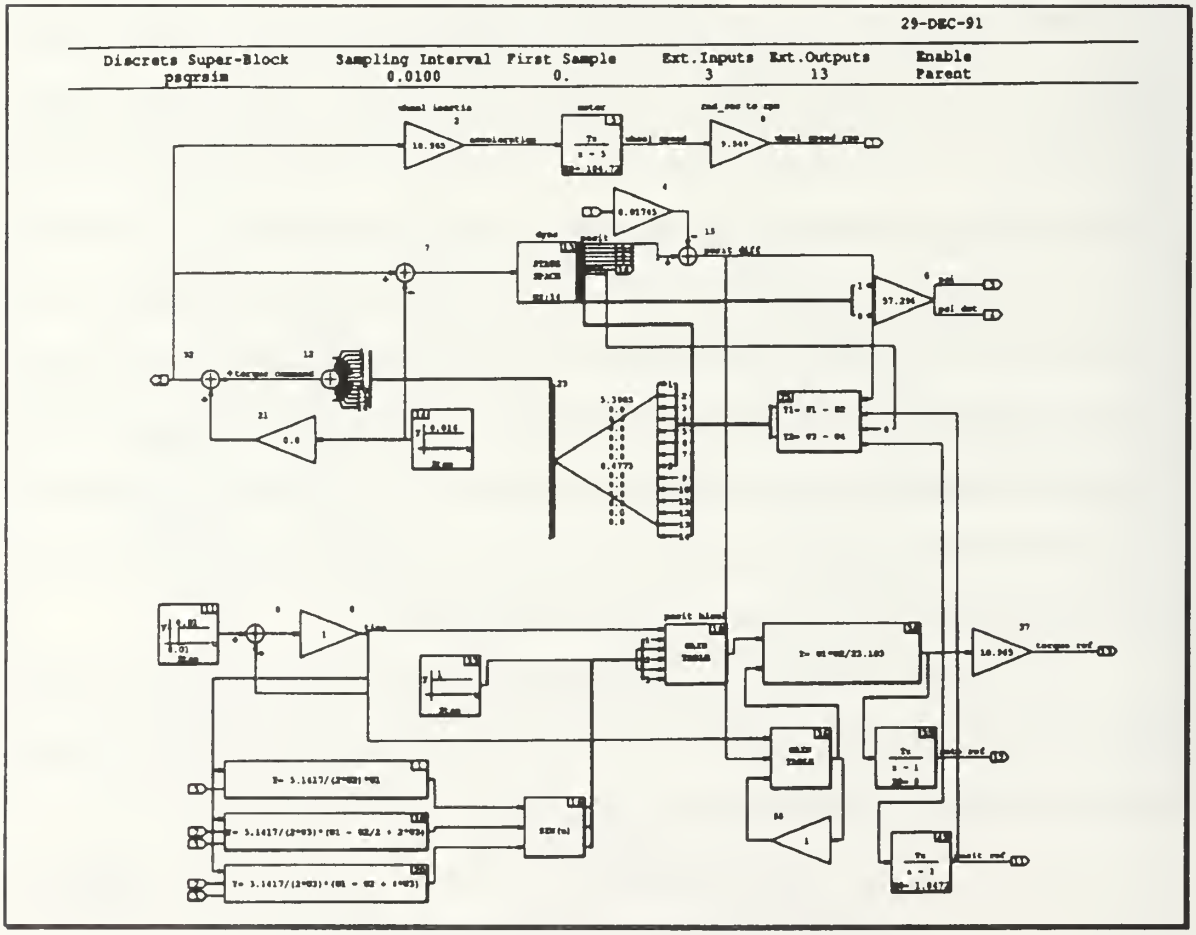
29-DEC-91
Discrete Super-Block
psqrsim
Sampling Interval
0.0100
First Sample
0.
Ext.Inputs
3
Ext.Outputs
13
Enable
Parent
10.965
9.549
0.01745
57.296
0.0
5.3985
0.4775
1
10.965

Figure 43. Pseudo-Square Torque Profile Block Diagram

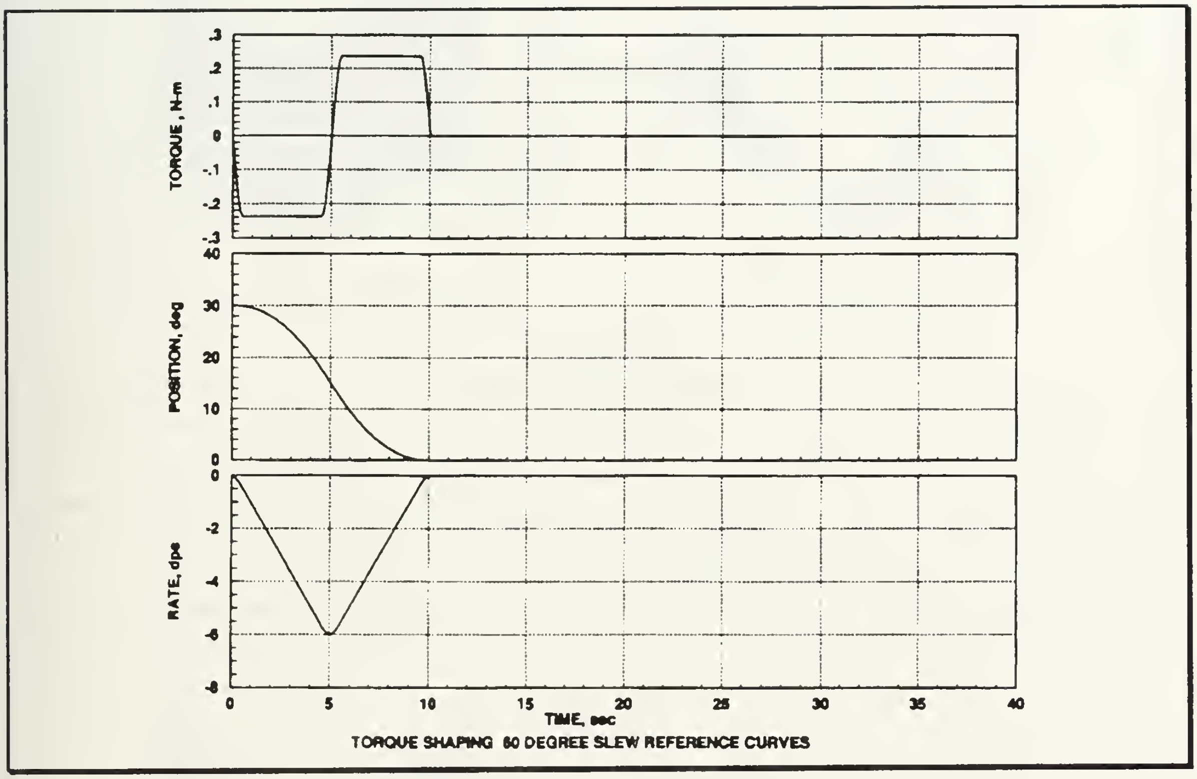

Figure 44. Reference Curves

Applying these as references for the flexible assemblage and using the same feedback gains determined for the PD controller gives the results shown in Figures 45 and 46 for a 30° and a 60° slew respectively. Comparing these with the Bang-Bang results indicates that although the Bang-Bang controller completes the maneuver sooner than the Torque Shaping, it induces oscillations in the appendage while attempting to maintain nominal control at the desired position. The actuator is working very hard in all parts of the maneuver compared to the

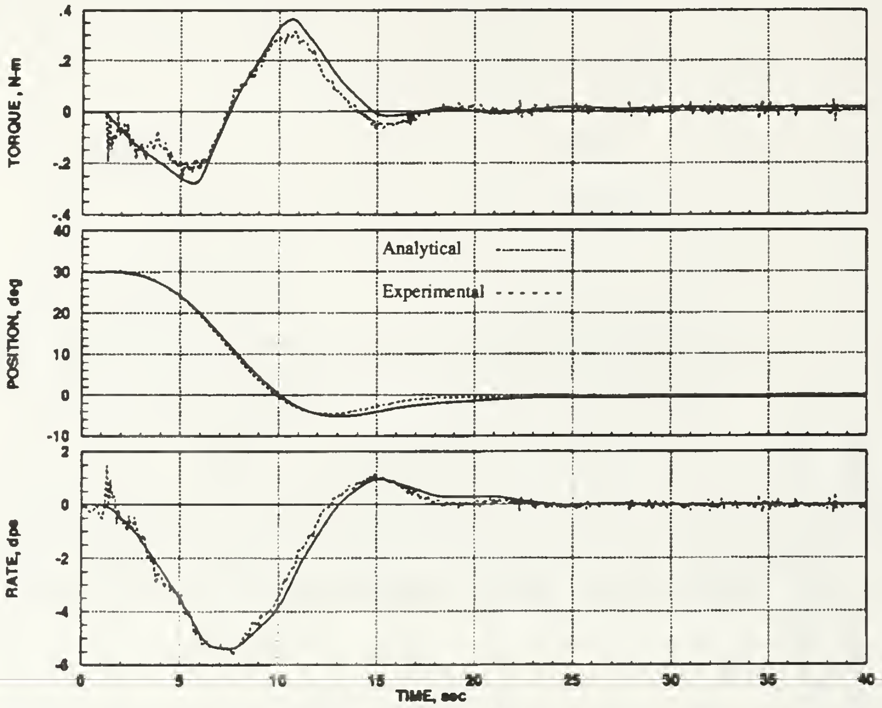

TORQUE SHAPING 30 DEGREE SLEW

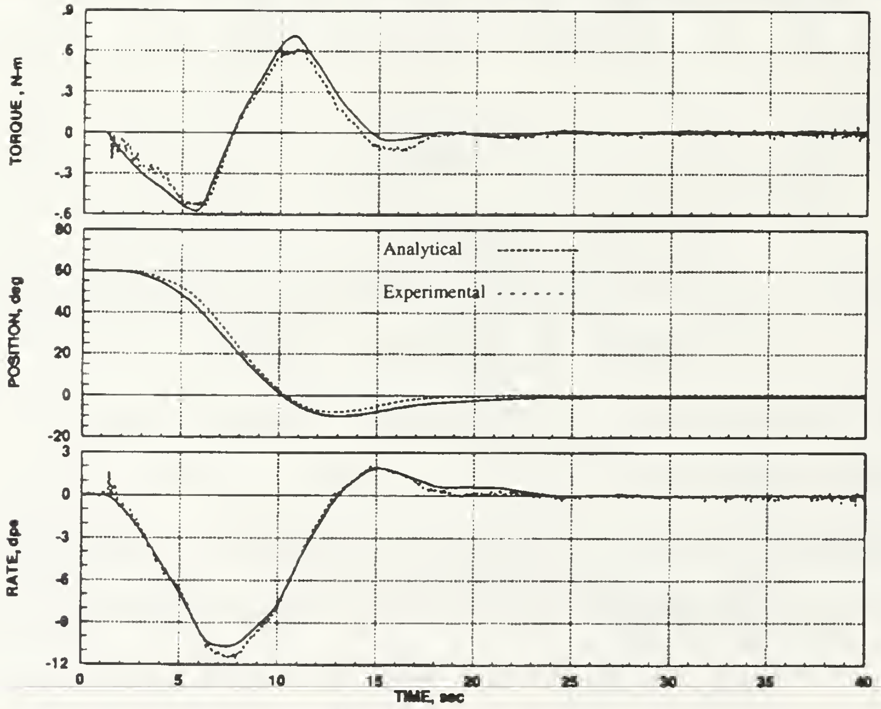

TORQUE SHAPING 60 DEGREE SLEW

Figures 45 and 46. Pseudo-Square Controller Response energy required for the Torque Shape controller. Figures 47 and 48 show the arm deflections for the same events.

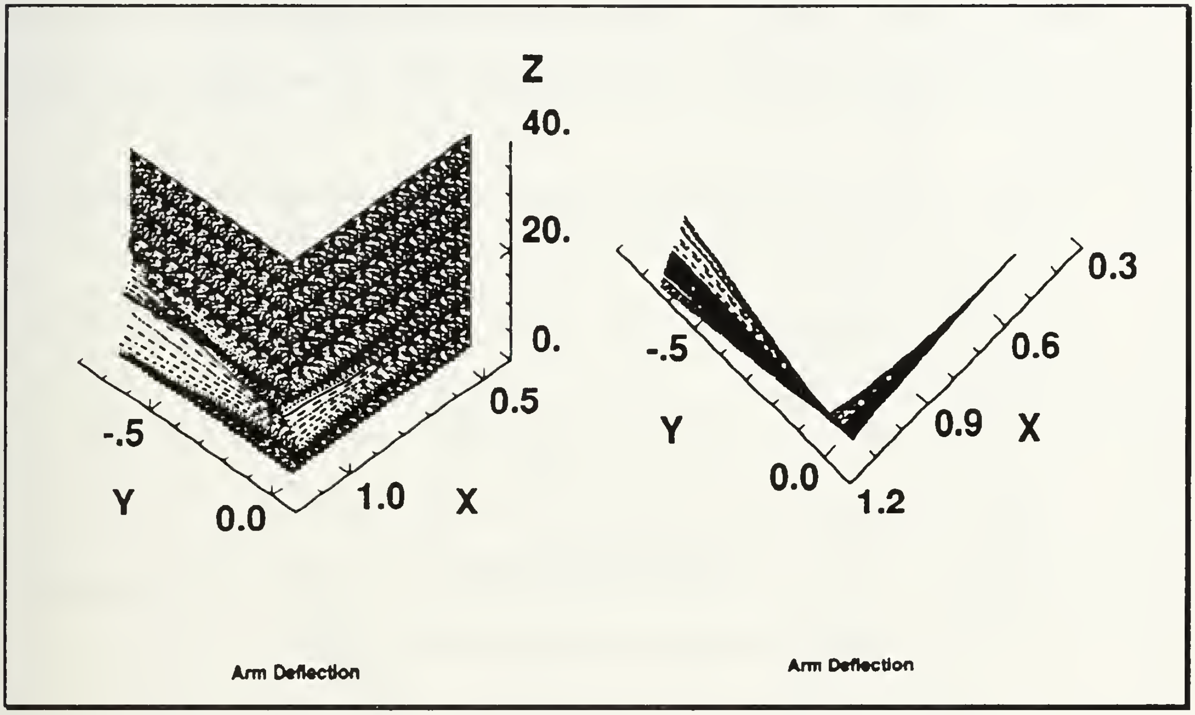

Figure 47. Arm Deflection for a 30° Slew

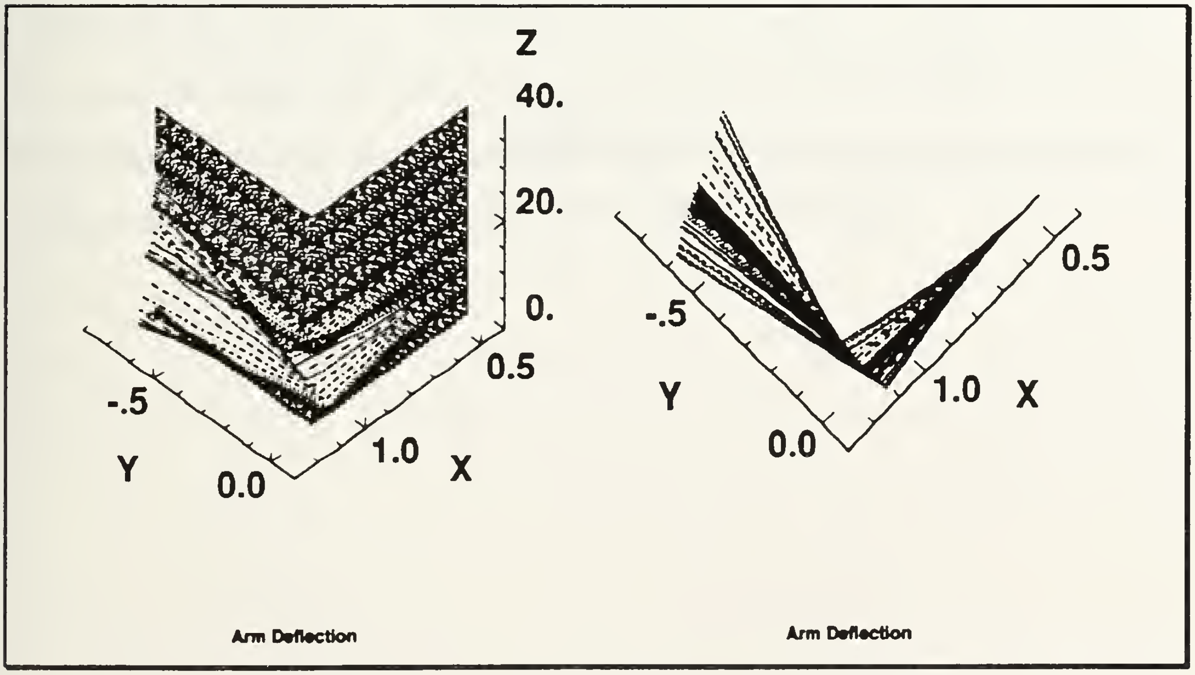

Figure 48. Arm Deflection for a 60° Slew

Figures 49 and 50 show the phase plots for the Torque Shape controller. They are very similar to those observed in the Sinusoidal model with considerably more overshoot. Experimental results agree with analytical predictions quite well and show a clear advantage over the oscillating Bang-Bang behavior.

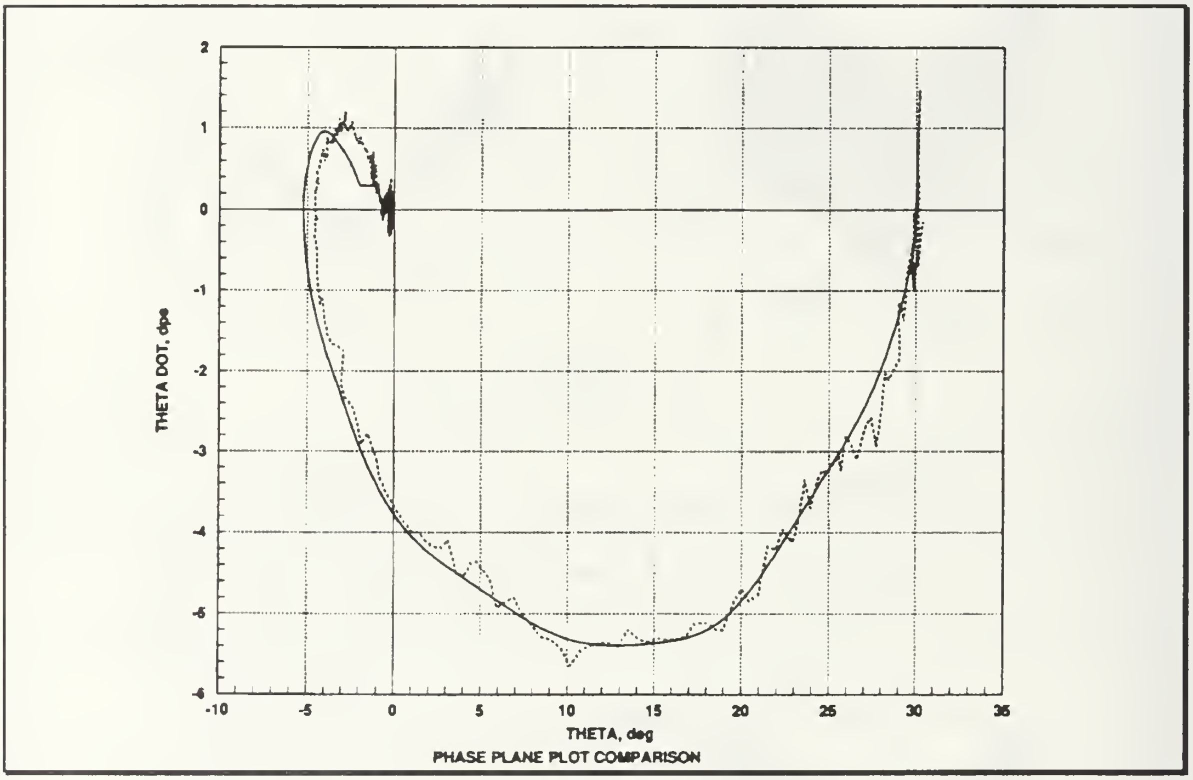

Figure 49. Phase Plot for a 30° Slew

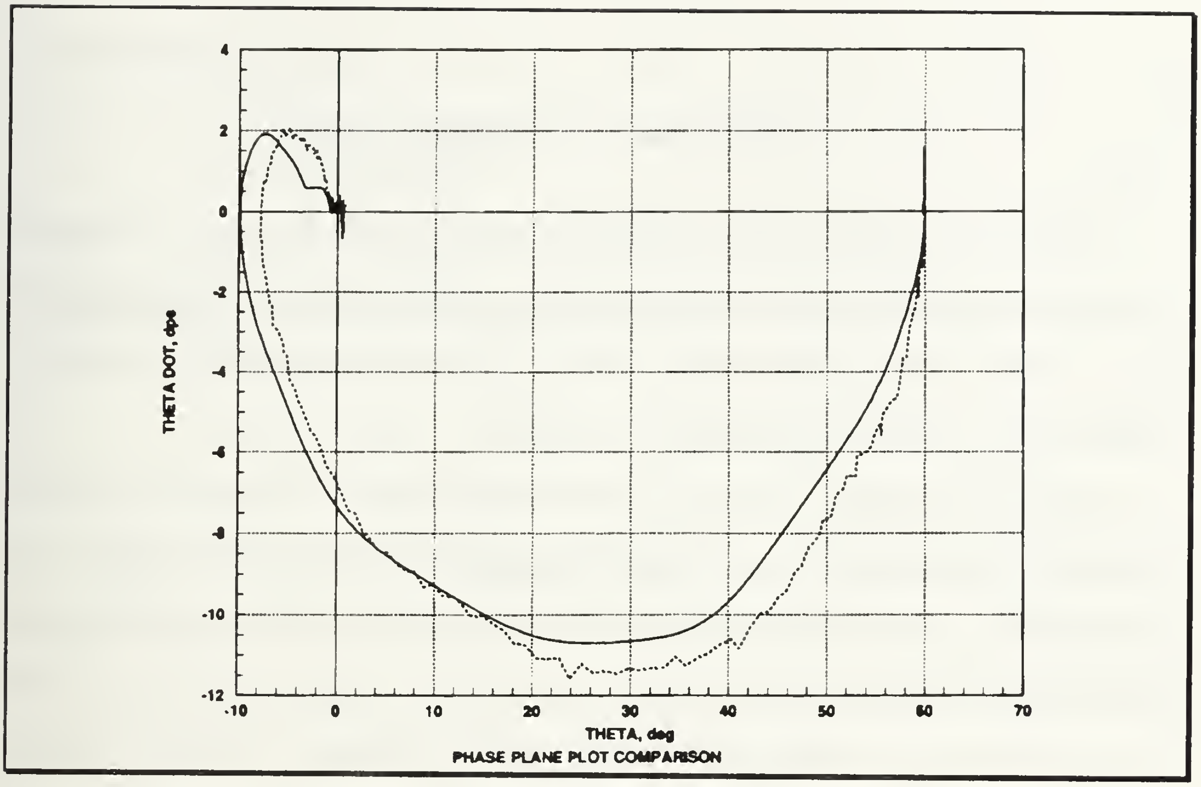

Figure 50. Phase Plot for a 60° Slew

By following position and rate trajectories, the control system is able to accomplish the slew maneuver without inducing severe transients to the momentum wheel. Also, the controller does not chatter or switch frequently. The actual torque path followed is significantly smoother than the modeled torque because the feedback gains are small. Introducing optimal gains may improve the system's performance.

V. BUILDING AN ESTIMATOR

Most of the modern control schemes require full state feedback. Normally this does not present much of a problem since estimated states can be derived from available sensor information. With the Flexible Spacecraft Simulator, however, none of the flexible modes are available.

Both of the dynamic models are derived from rigid body motion combined with flexible vibration. The fourteen states contain the rigid body position and rate as well as the six flexible displacements and velocities. These raw states are mapped into different spaces for each model using modal matrices. Of the fourteen states, only two are available for direct feedback. The other twelve must be estimated by some means for the controllers which require full state feedback. No direct modal information is available since the two sensed states are the rigid body ones. Consequently, the only information available about the flexible motion is contained in the analytical model which is known to be imperfect.

The most obvious method to construct the states is the Kalman estimator. The results of using this method are given in Chapter IV section B which proves it to be inadequate for real time control. Applying loop transfer recovery only improves the rigid body state reconstruction. Another approach is to use the Kalman estimator with a smarter choice of weighting matrices. The Kalman state equation is

$$\dot{\hat{\underline{x}}} = (A + BG)\hat{\underline{x}} + KC\underline{e} \tag{64}$$

where $\underline{x}$ = true states

$$\hat{\underline{x}} = \text{ estimated states} = \underline{x} + \underline{e} \tag{65}$$

The system dynamics are

$$\begin{aligned}\dot{\underline{x}} &= A\,\underline{x} + B\,\underline{u} \\ \underline{u} &= G\,\hat{\underline{x}} = G\,\underline{x} + G\,\underline{e}\end{aligned} \tag{66}$$

Substituting Equations (64) and (66) into the derivative of Equation (65) gives

$$\dot{\underline{e}} = (A + KC)\underline{e} \tag{67}$$

This is the basis of the Separation Principle which allows one to build the Optimal Regulator by assuming that full state feedback is already available. In effect, the estimator and the regulator are built separately and without knowledge of each other. However, Equation (66) can be written as

$$\dot{\underline{x}} = (A + BG)\,\underline{x} + BG\,\underline{e} \tag{68}$$

This says that the "actual" system dynamics are perturbed by the estimation error, $\underline{e}$. This perturbation is compounded by the REGULATOR gains, G, which leads to a curious conclusion. Although the regulator and the estimator may be considered separately, the dynamics of the system are altered by the regulator gains acting on the estimation error. To build an estimator that will best return the "actual" dynamics, one might minimize the second term in Equation (68) using a linear quadratic approach

$$J = \int \underline{e}^T G^T B^T B G \underline{e}\, dt \tag{69}$$

A weighting matrix can be identified from Equation (69) that corresponds to the Q_{xx} matrix used in the Matrix_X version of the Riccati equation solver. Q_{xx} is the state noise intensity. From Equation (69)

$$Q_{xx} = G^T B^T B G \tag{70}$$

The results of using Equation (70) in the Kalman estimator are shown in Figures 51 and 52. There is considerable improvement in the reconstruction of the first two flexible modes and their associated velocities over those attained in Chapter IV.

Looking at Figures 51 and 52 one can see that the last four modes have time constants that will play havoc on the dynamic system when fed back. If the regulator is modified so that the gains corresponding to these states are set to zero, the feedback controller will be reduced from 14th order to 6th order.

$$G' = [\ g1\ g2\ g3\ 0\ 0\ 0\ 0\ g8\ g9\ g10\ 0\ 0\ 0\ 0] \tag{71}$$

Substituting the new 6th order regulator gains (Equation 71) into Equation (70) and recalculating the estimator gains yields the estimated states shown in Figures 53 and 54. In effect, this procedure gives the closed loop estimation for states corresponding to the first three modes and the open loop estimation for the rest of the states. The sensor noise weighting matrix Q_{yy} remains the same as in Chapter IV. The analytical and experimental results for a 30° and a 60° slew are shown in Figures 55 and 56. Comparing these results to Figures 20 and 21 of Chapter IV, one can see a significant improvement. The arm deflections are shown in Figures 57 and 58 and are slightly larger than those of Chapter IV.

The faster slew time and larger arm deflections are caused by a reduced weighting on the input ($R_{uu} = 5$ instead of $R_{uu} = 7$ in Chapter IV).

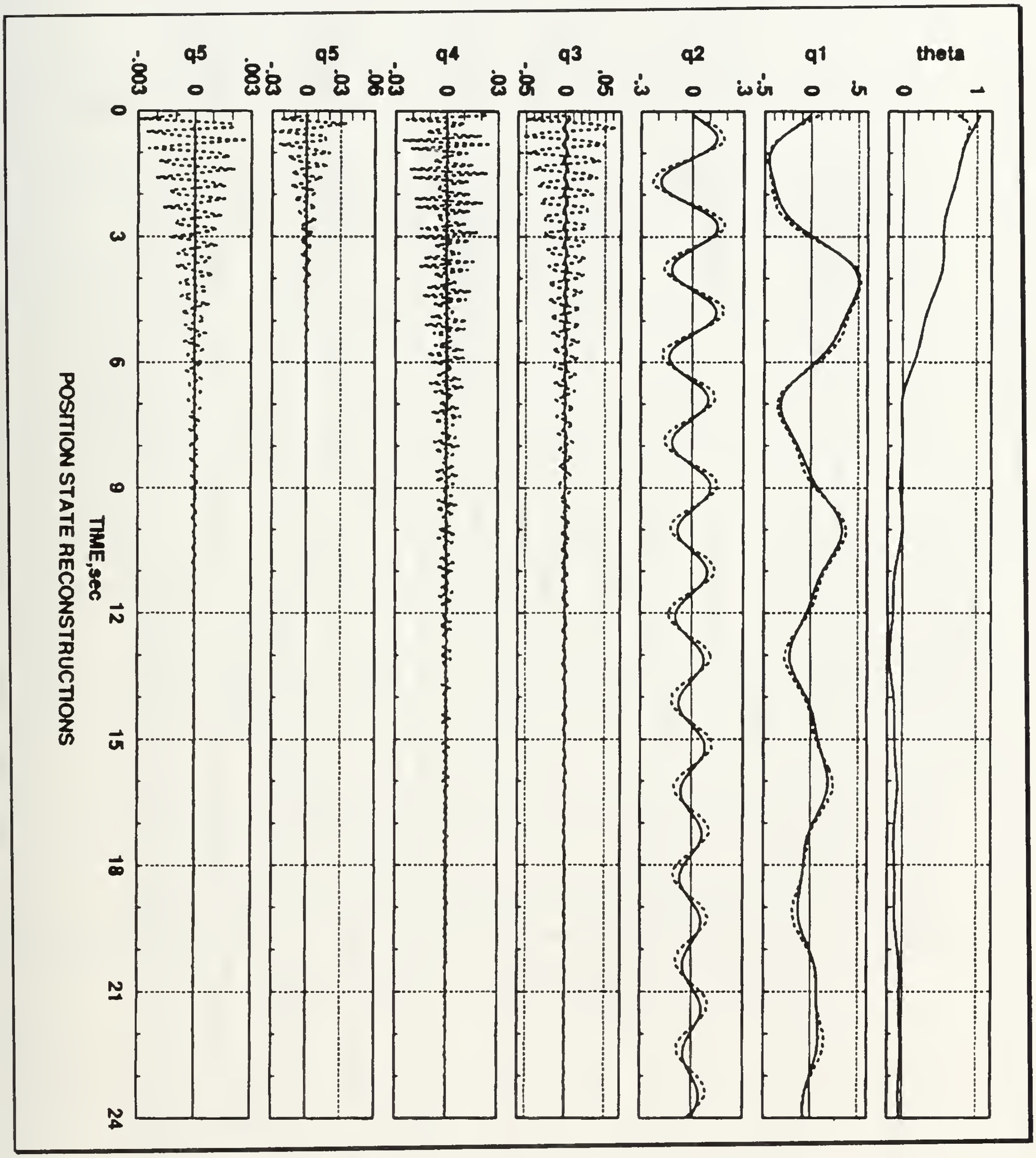

Figure 51. Reconstructed Positions

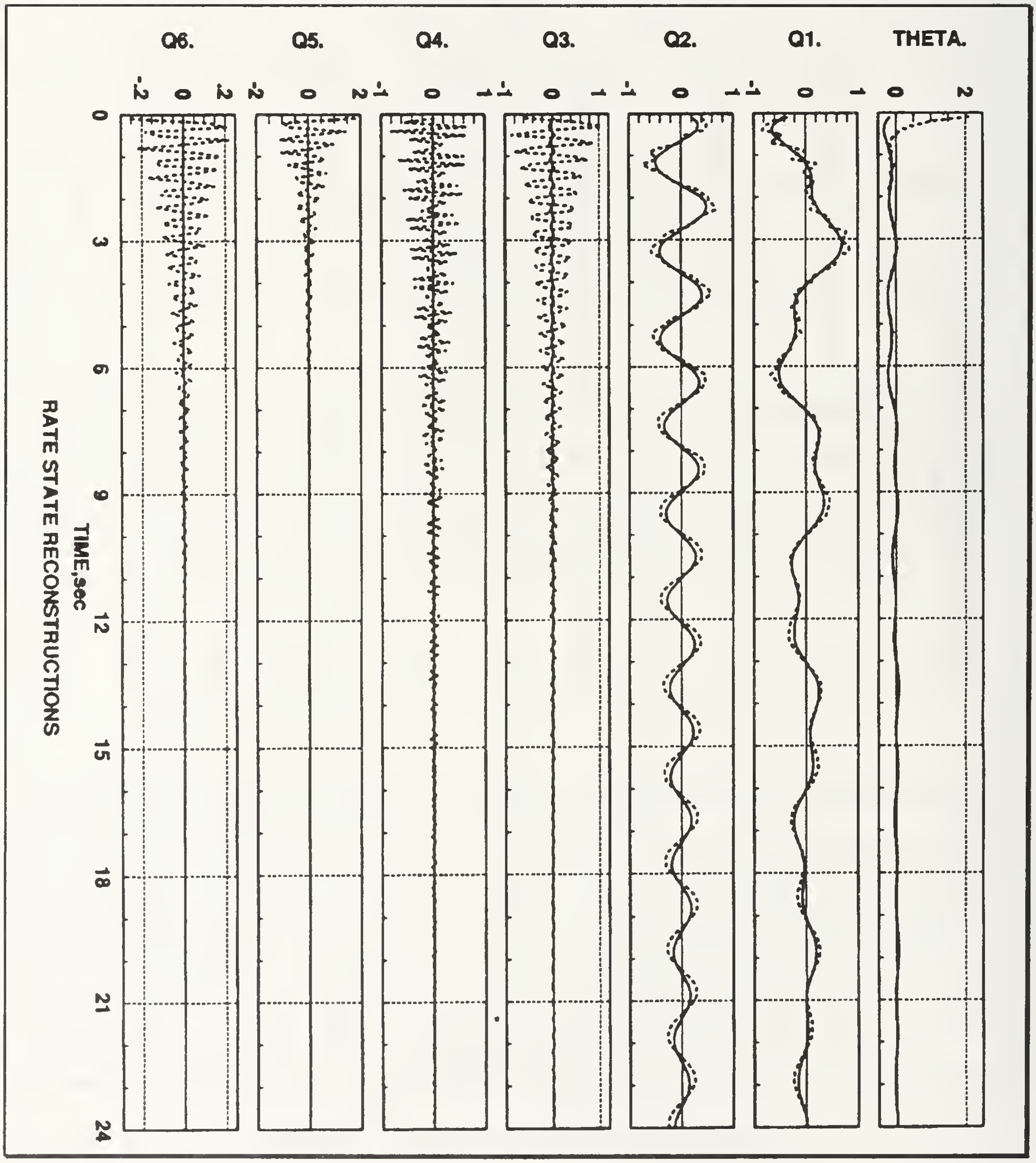

Figure 52. Reconstructed Rates

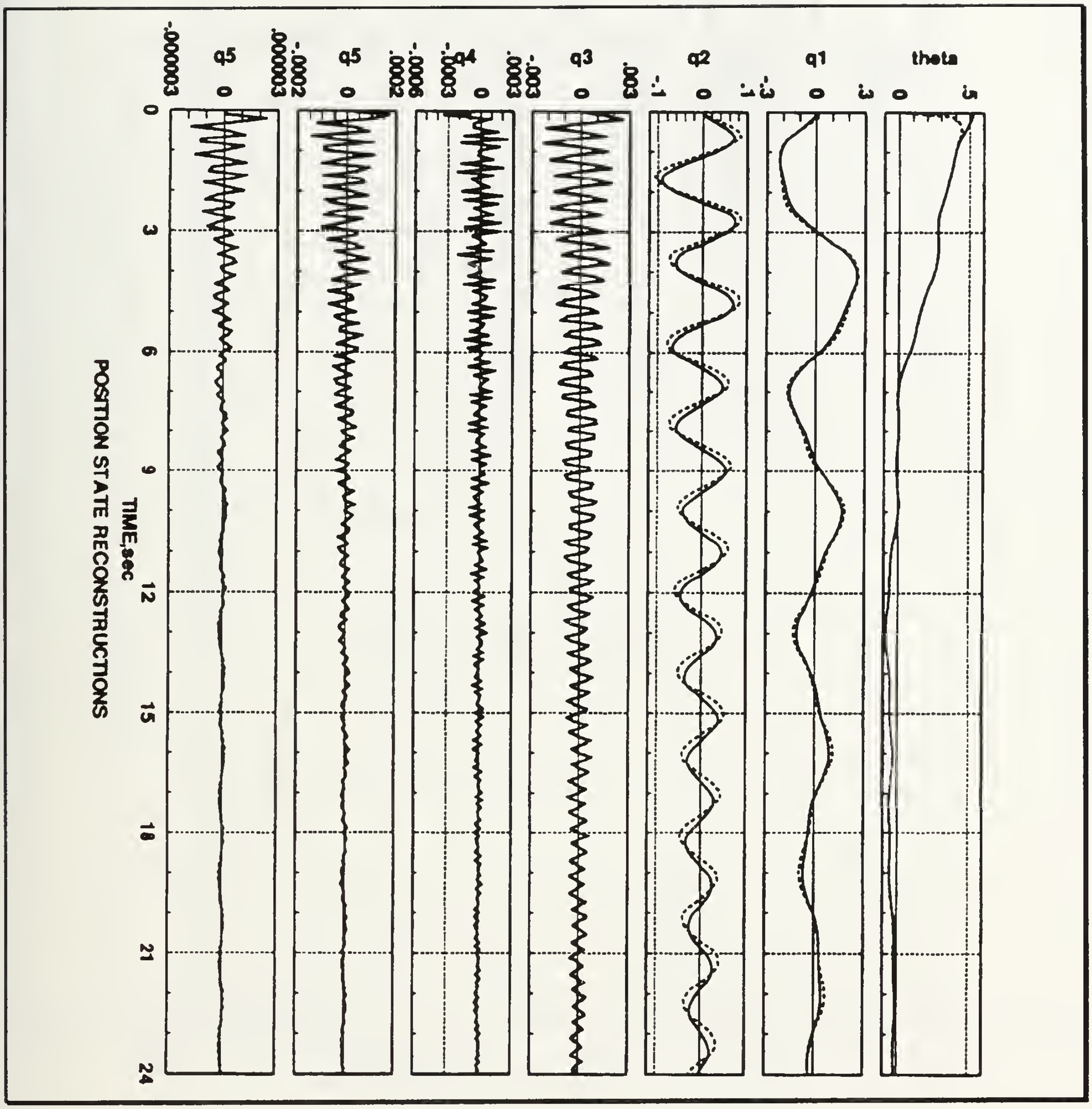

Figure 53. Reconstructed Positions

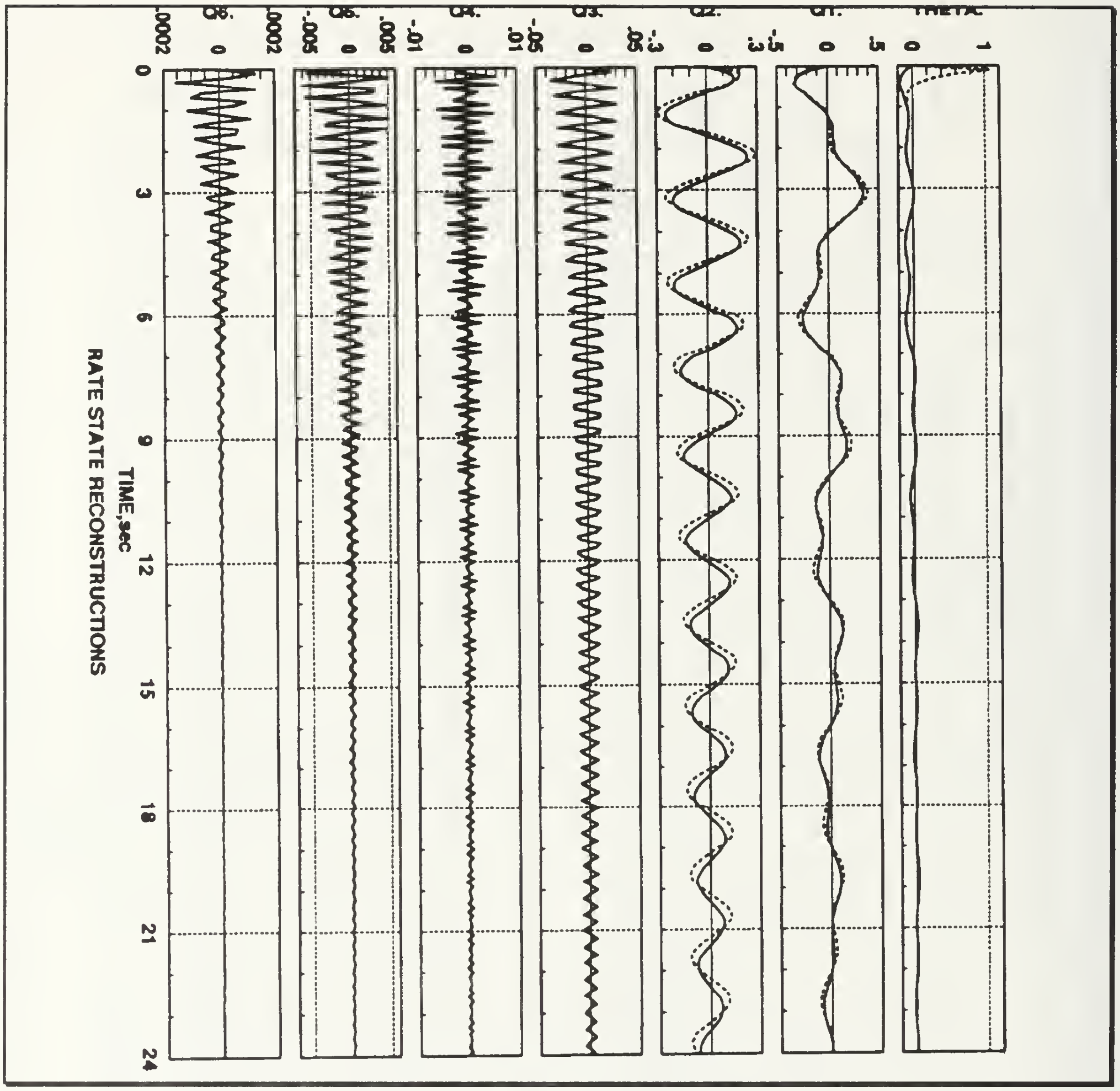

Figure 54. Reconstructed Rates

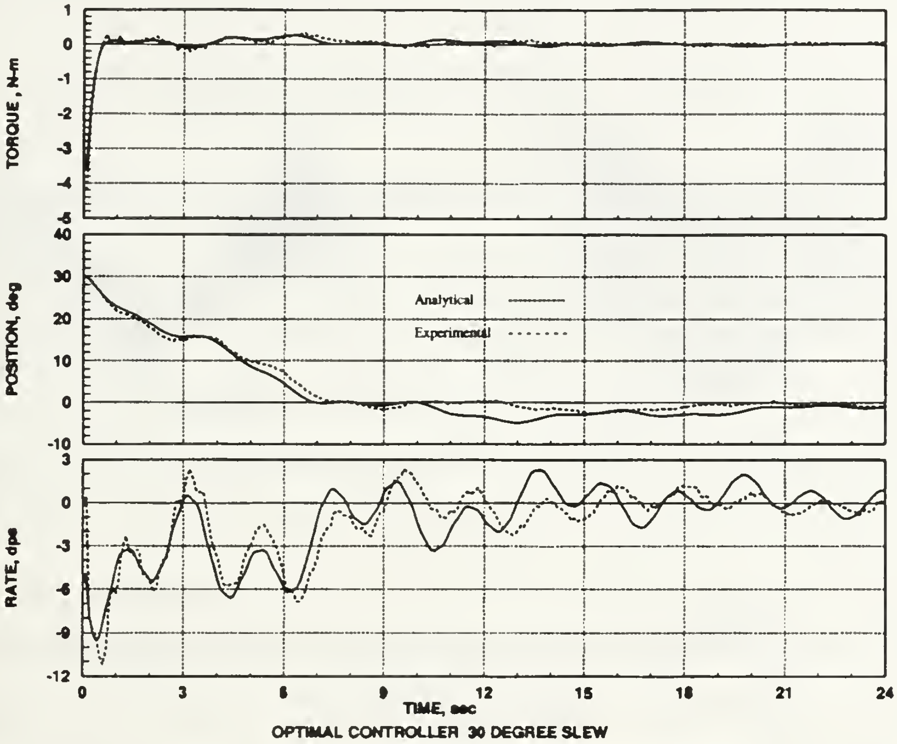

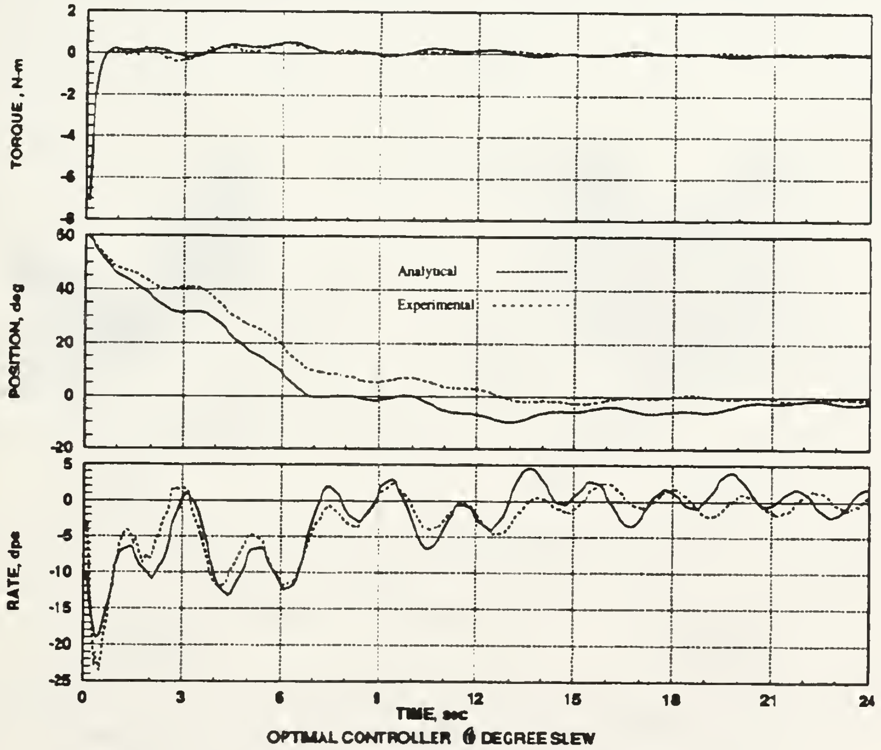

Figures 55 and 56. Optimal Response

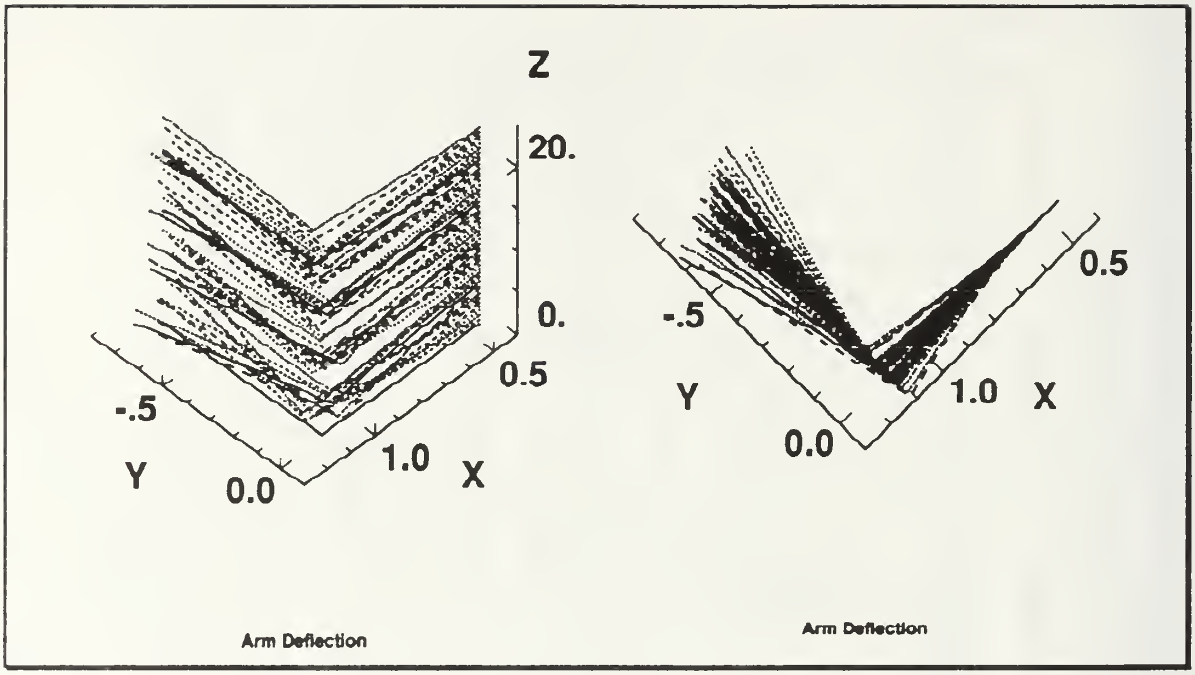

Figure 57. Arm Deflection for a 30° Slew

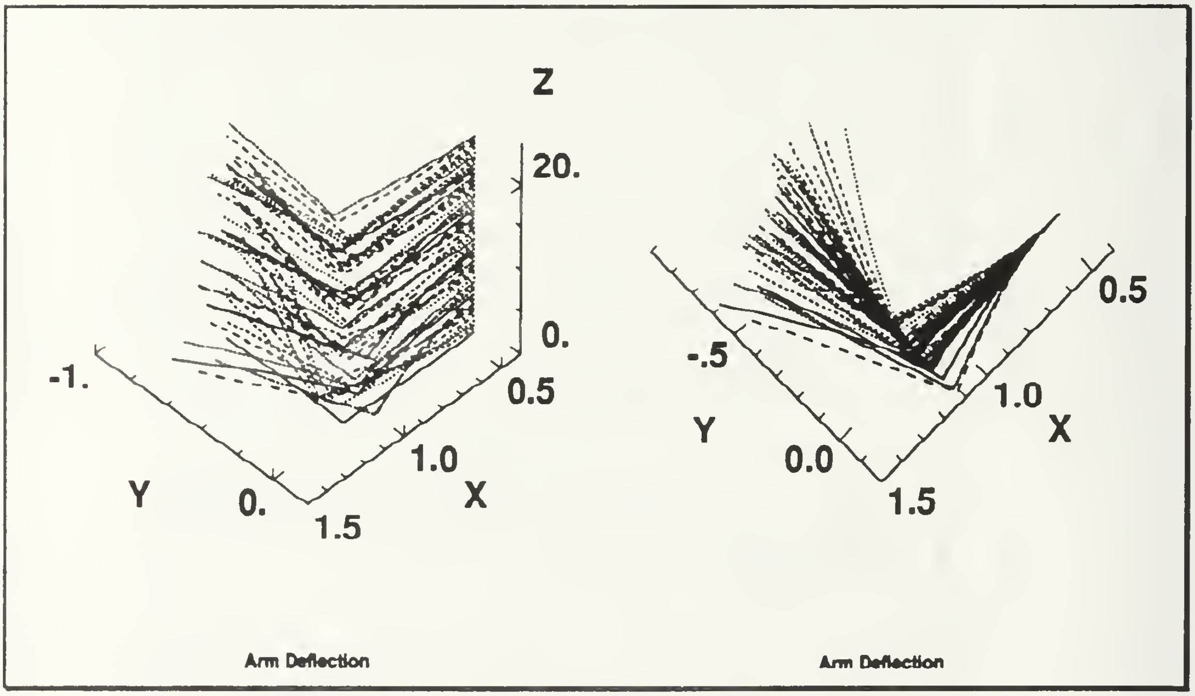

Figure 58. Arm Deflection for a 60° Slew

VI. SYSTEM MODEL SLEW MANEUVERS

A. EIGENSTRUCTURE ASSIGNMENT (REGULATOR)

The eigenstructure assignment method, developed by J.L. Junkins et al [Reference 8], allows the system designer to tune a controller by placing the poles of the system to add stiffness or adjust time constants. The idea behind the development of the eigenstructure assignment scheme is that the controller must be as benign as possible to reduce oscillations induced in the flexible appendage. If the system is forced to maintain its open loop eigenvectors through the control maneuver, the impact on the flexible portion would be minimized. This can be accomplished by adding a stabilty margin to the open loop eigenvalues and adjusting feedback gains. Assuming the solution of Equation (18) is of the form

$$X = \psi e^{\lambda t} \tag{72}$$

it becomes

$$\psi\lambda = A\psi + BH \tag{73}$$

where $U = GX = G\psi e^{\lambda t}$ and $H = G\psi$ (74)

Equation (73) is obtained by by substituting Equations (72) and (74) into Equation (18) and combining coefficients of $e^{\lambda t}$. Rearranging Equation (72) gives

$$\psi\lambda - A\psi = BH \tag{75}$$

which is the general Lyapunov equation for ψ. If λ is assumed to be

$$\widehat{\Lambda} = \Lambda_{open} - \text{stability margin} \tag{76}$$

then everything in Equation (75) is known except H and ψ. H is estimated by rearranging Equation (75) with the pseudo-inverse of B, using the open loop eigenvectors and assuming λ is defined by Equation (76). The stability margin is determined based on the desired characteristics of the control system. The estimation for H, $\widehat{H}$, is

$$\widehat{H} = \left(B^T B\right)^{-1} B^T \left(\psi_{open} \widehat{\Lambda} - A\psi_{open}\right) \tag{77}$$

Solving the Equation (75) for ψ gives an estimated modal matrix, $\widehat{\Psi}$, which can be used to find the gain matrix, G.

$$\widehat{H} = G\widehat{\psi} \tag{78}$$

B. EIGENSTRUCTURE ASSIGNMENT (ESTIMATOR)

One approach to estimation applies the eigenstructure assignment concept to find the estimator gains. A standard rule of thumb is to use poles that are five to ten times stronger than the regulator poles.

$$\lambda_{est} = \lambda_{reg} - 0.8 \tag{79}$$

Using the open loop eigenvectors as a starting point, the same method used for obtaining the regulator gains may be applied to find the estimator gains. Some difficulties arise when implementing this estimation scheme.

The estimated states are assumed to be of the same form as those of Equation (71). The eigenvalue problem is posed in the same manner as the regulator problem with one exception. Comparing Equation (67) with Equation (18), where U = GX, it is immediately apparent that the estimator gains, K, do not directly multiply the states as the regulator gains do. To obtain the same form as the regulator problem, the relationships of the right and left eigenvalue problems will be used. Equation (67) will form the basis of the right eigenvalue problem and the left eigenvalue problem will be derived from

$$\dot{\underline{f}} = (A^T + C^T K^T)\,\underline{f} \tag{80}$$

where $\underline{f} = \underline{l}\,e^{\lambda t}$ and $\underline{e} = \underline{r}\,e^{\lambda t}$ (81)

$\underline{l}$ = left eigenvector $\underline{r}$ = right eigenvector

Thus, the associated eigenvalue problems are

$$\begin{aligned} \lambda\underline{r} &= (A + KC)\,\underline{r} \\ \lambda\underline{l} &= (A^T + C^T K^T)\,\underline{l} \end{aligned} \tag{82}$$

with the properties that the eigenvalues for both equations are equal and the matrix of eigenvectors are related by [Reference 8],

$$L = R^{-T} \tag{83}$$

From this one can solve the gains for the right eigenvalue problem using the matrix of right eigenvectors and their associated eigenvalues. Once these gains are found, simply transposing them gives the gains for the esitmator problem of interest.

Unfortunately, eigenstructure assignment of the estimator poles requires more state feedback than is currently available from the FSS. The acheived eigenvalues are not the same as the target eigenvalues for all the modes. Specifically, for the FSS only the rigid body modes achieved their target eigenvalues.

VII. THRUSTER ACTUATION

A. THRUSTER SYSTEM OVERVIEW

An air thruster system will be used to study the effects of momentum wheel desaturation on flexible spacecraft. It will then be used to actuate slew maneuvers in place of the momentum wheel. A schematic of the system is shown in Figure 59. The air tank will be mounted on top of the momentum wheel assembly. Flexible air hose will run to a gauge-regulator-manifold assembly mounted radially from the central body center of rotation. Solenoid valves will be mounted on the manifold in opposing positions to provide positive and negative slewing with tangential forces. A part by part explanation of the thruster system follows. The numbers refer to those in Figure 59.

1. The air tank is a 13.3 cubic foot, 3000 psi tank manufactured by Sherwood Industries. Its mounting is similar to that of a fire extinguisher which facilitates ease of replacement without tools. Three tanks were obtained so that a full replacement is always on hand.

2. The tank valve is a standard scuba valve and was delivered with the tank.

3. A DIN connector is attached to the tank valve. The DIN connector is easily detached and attached to the tank valve by hand which enables the user to replace the tank without tools.

4. This adaptor is required to reduce the DIN connector diameter to the diameter of the flexible hose.

5. A connector attaches the adaptor to the flexible hose.

6. Flexible hose is used for adaptability of the system placement on the central body. Since space is limited, future modifications may require the

movement of some or all of the thruster system parts. Flexible hose allows the system to be moved without difficulty or redesign.

7. The flexible hose is connected to a filter tee to protect the pressure regulator from harm. It also allows the placement of the high pressure gauge to monitor regulator inlet pressure.

8. The snubber protects the pressure gauge from possible pressure surges.

9. This 0-3000 psi pressure gauge is used to monitor the pressure regulator inlet. It is also used to determine the replacement of the air tank.

10. The pressure regulator was obtained from Hydracon Corporation and is used to regulate the pressure from 3000 psi to 200 psi.

11. A connector is needed to attach the outlet of the pressure regulator to the manifold.

12. The manifold distributes the 200 psi air to each solenoid valve. Also coming from the manifold is the low pressure gauge.

13. The low pressure gauge is also protected by a snubber.

14. This 0-250 psi pressure gauge monitors the inlet pressure to the solenoid valves which determines the thrust provided.

15. The thruster valves are solenoids obtained from the Naval Research Laboratory. They are rated at 0.0224 lbm/sec with a 10 msec cycle time.

16. Since the solenoid outlet diameter is one-sixteenth of an inch, no nozzle is required. This results in an insignificant loss of thrust. Thrust calculations are done in Appendix B.

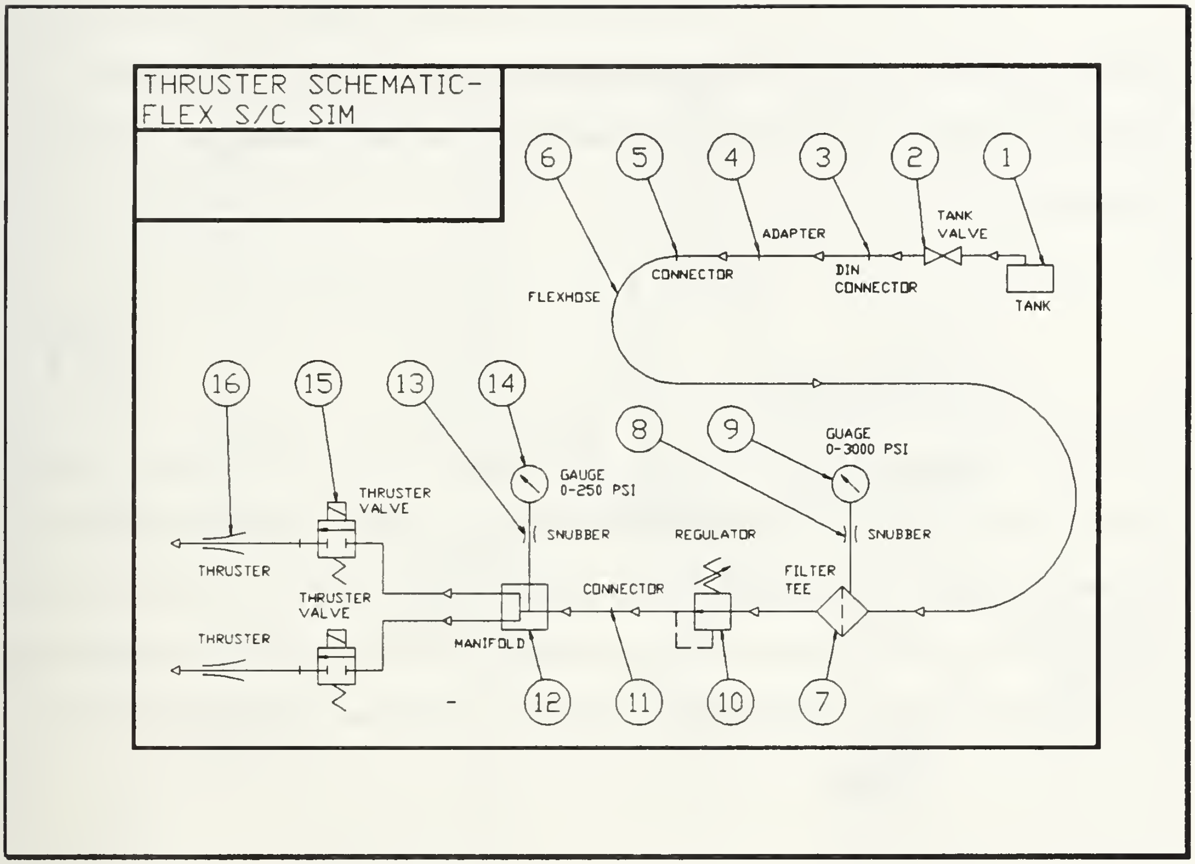
THRUSTER SCHEMATIC-
FLEX S/C SIM
6
5
4
3
2
1
TANK
VALVE
ADAPTER
CONNECTOR
DIN
CONNECTOR
TANK
FLEXHOSE
16
15
13
14
8
9
GUAGE
0-3000 PSI
GAUGE
0-250 PSI
THRUSTER
VALVE
SNUBBER
REGULATOR
SNUBBER
THRUSTER
FILTER
TEE
CONNECTOR
THRUSTER
VALVE
THRUSTER
MANIFOLD
12
11
10
7

Figure 59. Thruster System Schematic

Appendix B contains the thrust calculations for the air system based on chamber pressure for air.

B. MOMENTUM WHEEL DESATURATION

As mentioned in Chapter IV the cabling to the momentum wheel assembly creates a spring torque which acts in a negative sense on the central body. When a slew maneuver is completed, the controller continues to hold the body in position. Consequently, the momentum wheel gains angular momentum by counteracting the disturbance torque from the cabling.

Momentum wheel desaturation is accomplished by firing a thruster so that it creates a torque which acts in a positive sense on the body. The controller will respond by slowing down the wheel to counteract this new torque in order to maintain position. Since the wheel angular momentum is proportional to its speed of rotation, a decrease in wheel speed means a decrease in angular momentum.

$$h_w = I_w \Omega \tag{84}$$

Thrust calculations are given in Appendix B. For a 200 psig chamber pressure, the thrust achieved is 0.6 N-m without a nozzle. Unfortunately, when the solenoid valve is fully open, the chamber pressure drops to 130 psig which yields a thrust of 0.35 N-m. The momentum of the thruster pulse is determined by the pulse magnitude and the pulse duration. Therefore, from Equation (84)

$$T\,\Delta t = I_w\,\Delta\Omega \tag{85}$$

Rearranging Equation (85), the thruster pulse time is

$$\Delta t = \frac{I_w}{T}\,\Delta\Omega \tag{86}$$

Figure 60 is the block diagram for the momentum dumping routine. It is designed to desaturate the wheel when it reaches 1100 rpm. The pulse duration is 4.25 seconds which will dump 180 rpm by Equation (86). Figure 61 illustrates a 30° slew maneuver followed by a wheel desaturation thruster pulse. Experimental results compare favorably with the analytical prediction. An eight degree position offset is induced which the controller corrects within ten seconds. Figure 62 shows the reduction in wheel speed for the same maneuver. The tachometer data (dashed line) is digitally filtered to reduce noise resulting in the two second time lag between experimental and analytical data.

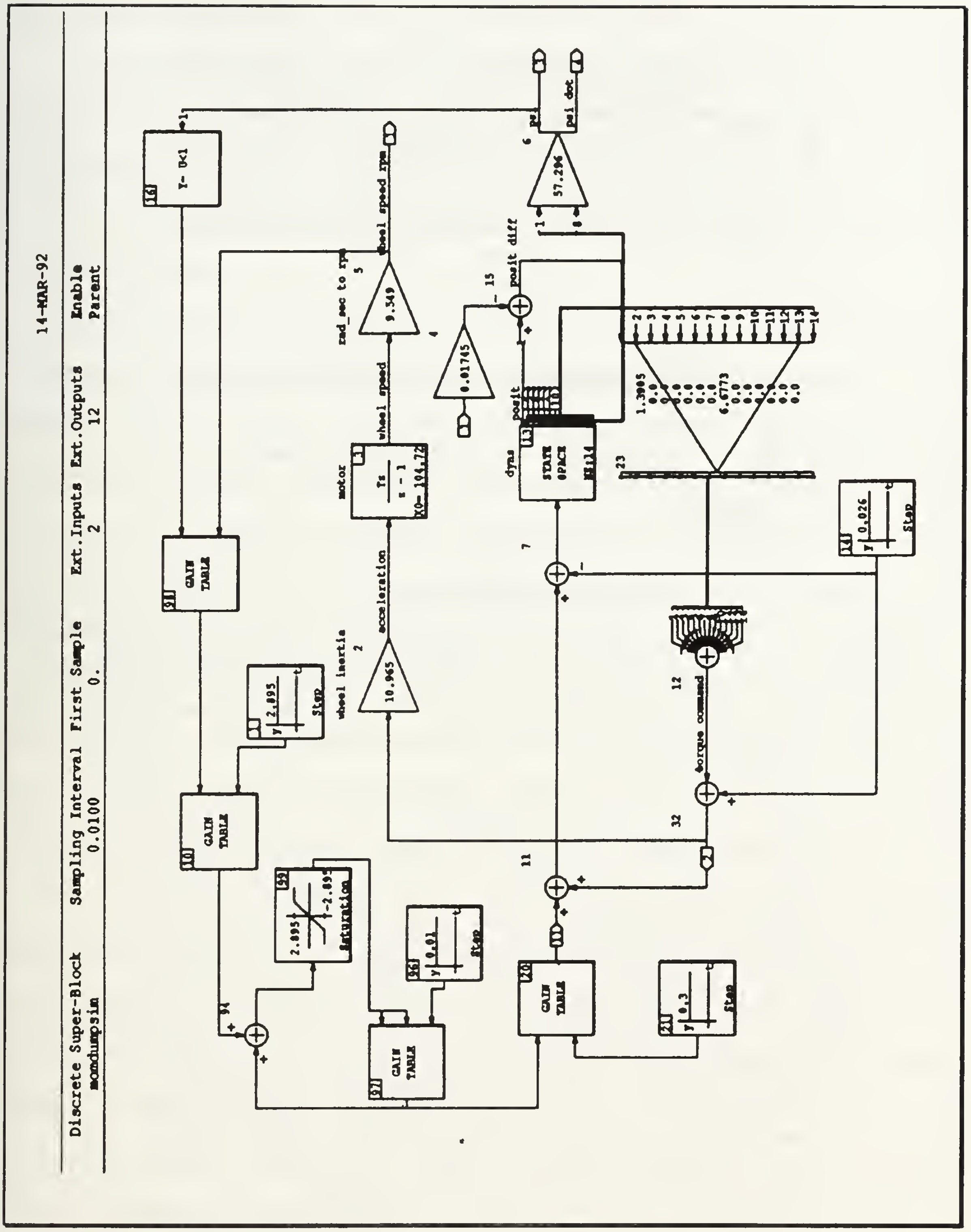
Discrete Super-Block
momdumpsim
Sampling Interval
0.0100
First Sample
0.
Ext.Inputs
2
Ext.Outputs
12
Enable
Parent
14-MAR-92
Y= U<1
GAIN TABLE
GAIN TABLE
GAIN TABLE
GAIN TABLE
Step
2.895
0.01
0.3
0.026
Saturation
-2.895
wheel inertia
10.965
acceleration
motor
Ts
z - 1
wheel speed
9.549
rad_sec to rpm
wheel speed rpm
0.01745
posit diff
57.296
psi
psi dot
dyns
STATE SPACE
posit
1.3905
6.6773
torque command

Figure 60. Momentum Dumping Block Diagram

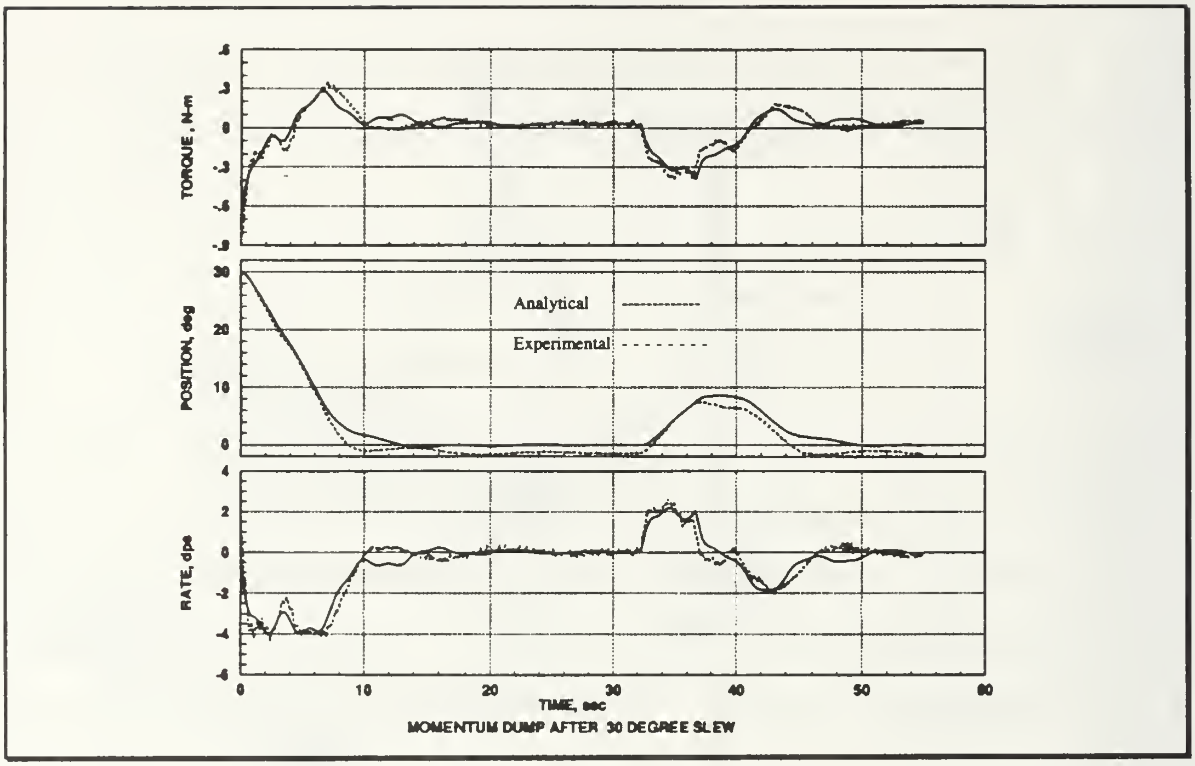

Figure 61. 30° Slew Maneuver Followed by Momentum Dumping

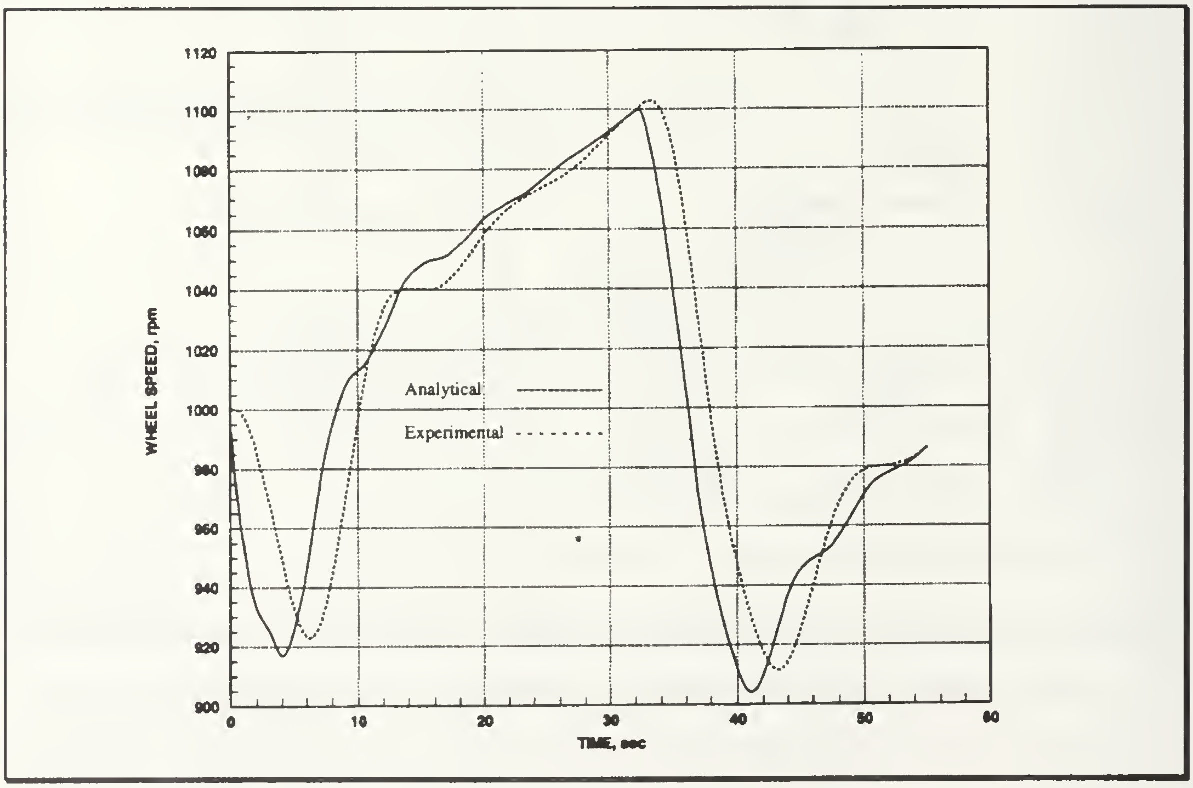

Figure 62. Wheel Speed During Desaturation

C. SLEW CONTROL

Thruster slew maneuvers are accomplished using the Bang-Bang control technique because the thrusters deliver on/off pulses. The same control law developed in Chapter IVc (Equation (50)) is implemented for slewing. Instead of timing the pulses, the firing sequence is determined through position and velocity feedback.

Figure 63 is the block diagram for the system. It contains the same algorithm except that it orders thruster firings instead of momentum wheel speeds. Figures 64 and 65 show the experimental results compared with the analytical predictions. The system performance is much improved over the previous results (Figures 29 and 30) implemented with a momentum wheel. The thruster torque level is 0.35 N-m. Initial control switching is more frequent than predicted but the amount of chattering after completing the slew is much less. The increased switching at the beginning is caused by noise in the rate sensor. From Equation (50) it is apparent that as the position difference decreases, the slew rate dominates the switching law. This becomes critical about halfway through the maneuver when the argument of the SGN function is close to zero.

The slew time is slightly faster than the momentum wheel bang-bang maneuver. During the slew, the flexible appendage deforms (Figures 66 and 67) as it did with the momentum wheel actuator. However, when the central body reaches the desired position, the thruster actuation acts to dampen the flexible motion. Momentum wheel actuation acted to resonate the flexible motion of the arm which caused excessive chattering to maintain position. For this reason alone the thruster actuated bang-bang maneuver is vastly superior to momentum wheel actuation.

As stated earlier, the thrusters provide on/off control torques. However, the significant difference between the full flow (on) operating pressure and the static (off) operating pressure indicates that thrust levels are not constant. There must be an associated rise and set time in which the pressure adjusts between full flow and static states. The 0.35 N-m torque presented here is only the average value over a typical thruster pulse. Efforts to minimize this pressure difference are discussed in the conclusions.

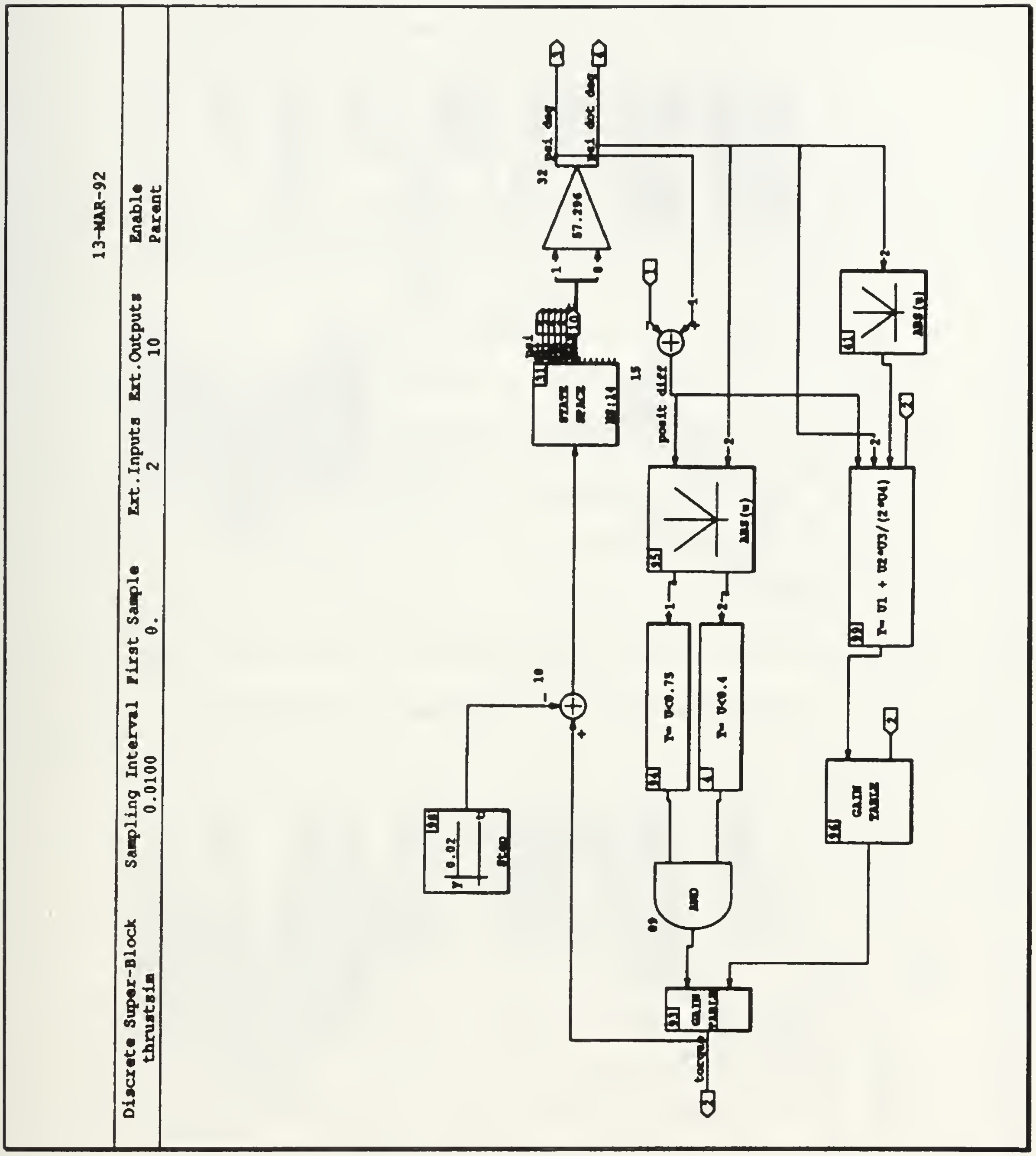
Discrete Super-Block
thrustsim
Sampling Interval
0.0100
First Sample
0.
Ext.Inputs
2
Ext.Outputs
10
Enable
Parent
13-MAR-92
step
0.02
10
STATE SPACE
psi deg
psi dot deg
57.296
32
15
posit diff
ABS(u)
Y= U<0.75
Y= U<0.4
AND
89
Y= U1 + U2*U3/(2*U4)
GAIN TABLE
torque

Figure 63. Thruster Slew Block Diagram

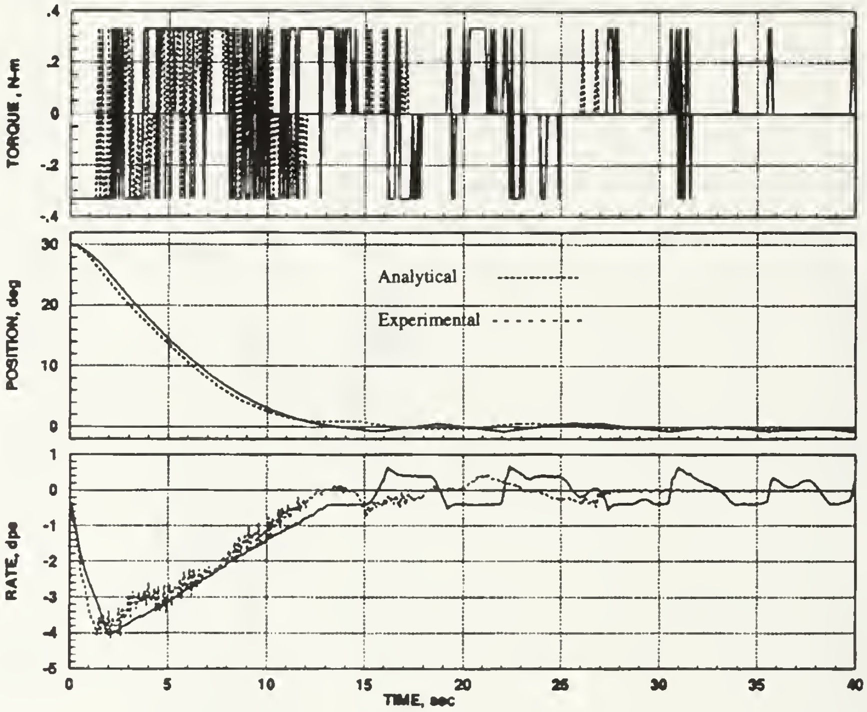

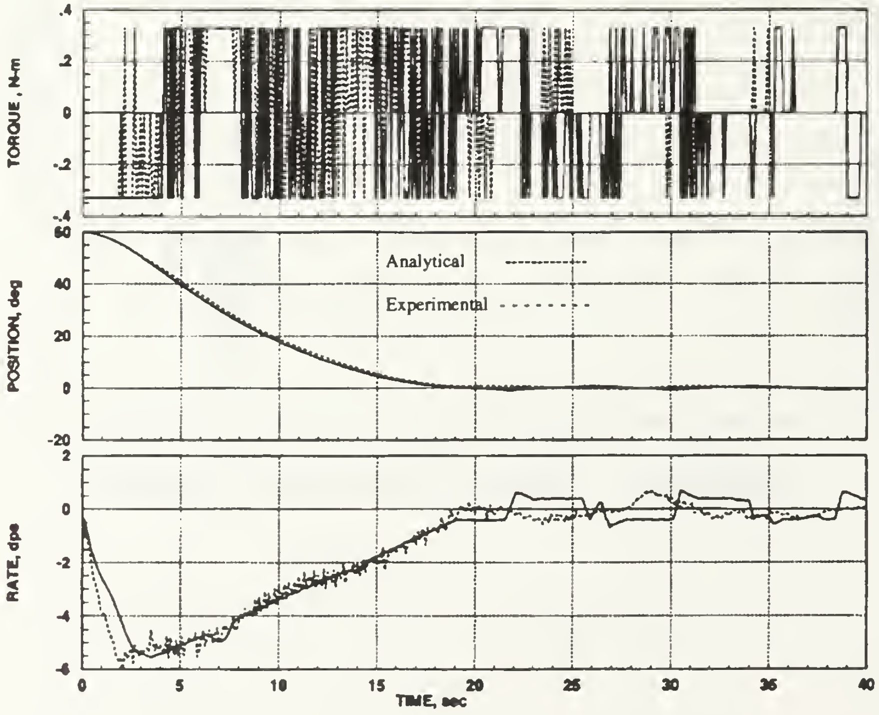

Figures 64 and 65. Thruster Slew Response

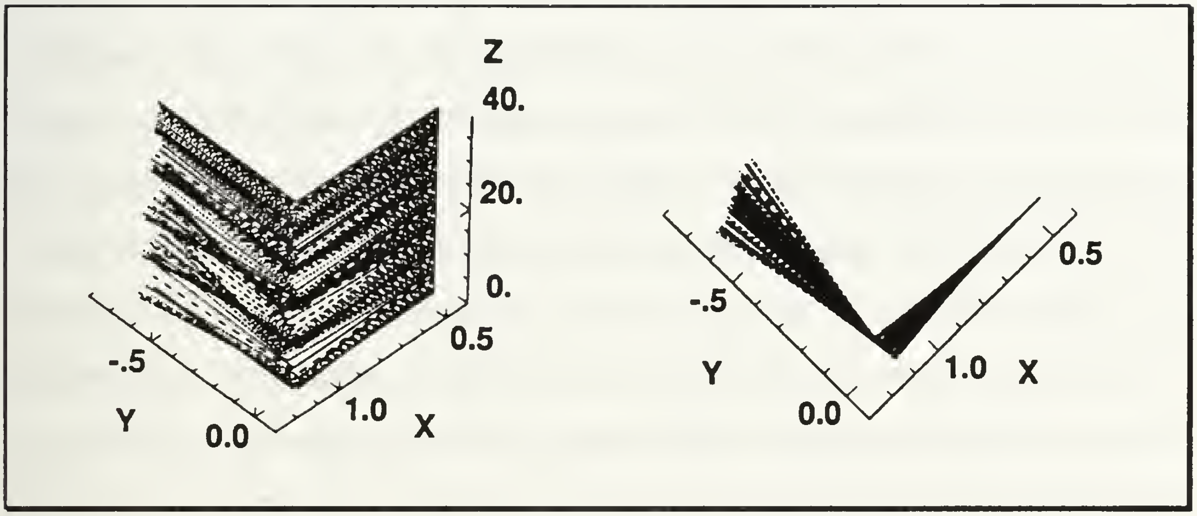

Figure 66. Arm Deflection for a 30° Slew

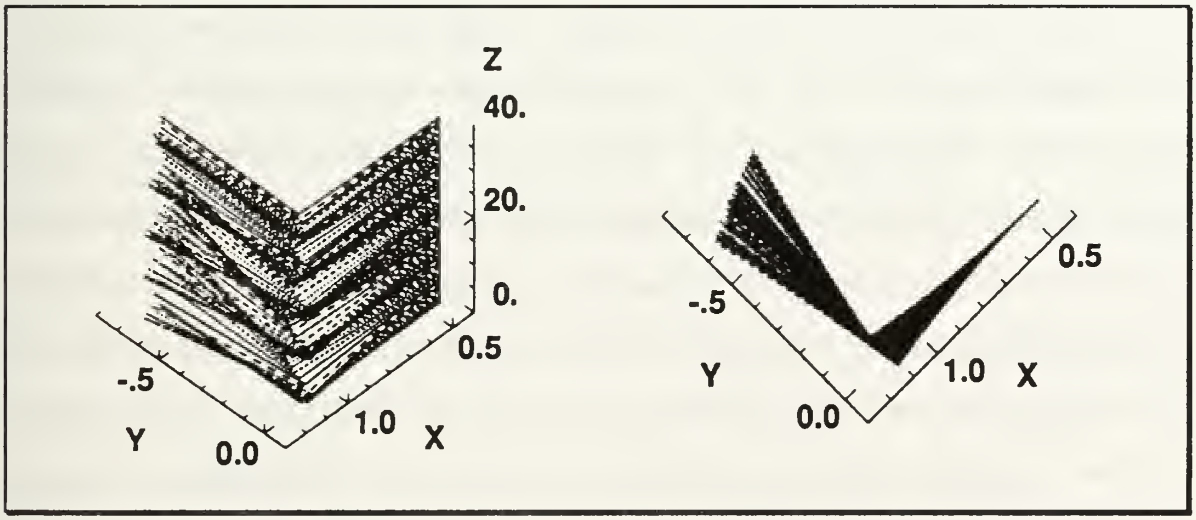

Figure 67. Arm Deflection for a 60° Slew

VIII. CONCLUSIONS

Experiments conducted using the Flexible Spacecraft Simulator have proven to be very successful. In all cases, experimental data is in close agreement with analytical predictions. This result alone implies that the linearized models developed are adequate for all of the controllers discussed in this thesis even though flexible deformations are *not* small enough to be considered negligible.

The parameters by which the control schemes are compared are control effort, slew time and flexible interaction. The goal for each slew maneuver is to rotate in the shortest time possible while minimizing oscillations in the flexible appendage. From this point of view, the controller of choice is the sinusoidal torque-shaping. It ranks the highest in all three areas of interest. The PD controller and the pseudo-square torque shaping scheme have advantages in different areas. The PD is a few seconds faster but it requires almost eight times the control effort for the same maneuver. The flexible interactions are not significant in either scheme. The updated optimal controller could be useful if the control effort were not very important. It has the advantage over all of the others in slew time but the torque used is relatively high. As a result, the oscillations induced in the flexible appendage are significant. The standard optimal controller cannot be used until more states are available to the estimator. Finally, the bang-bang controller is not acceptable because of the chatter it causes when trying to maintain a certain position. It may be possible to combine the bang-bang with one of the smoother controllers in a switching algorithm that slews using the bang-bang and maintains position with the other.

The two analytical models are derived from the same linearized equations of motion. The first model builds a state-space representation from rigid body motion and the cantilever flexible modes. Consequently, the system matrices are derived from *cantilever* mass normalized equations of motion. In contrast, the system modal model forms system matrices which are derived from the *system* mass normalized equations of motion. The system modal model has been developed mostly to provide the matrices necessary for using the eigenstructure assignment techniques which require system mass normalized matrices. The drawbacks of this model are the complexity of transforming from physical coordinates to modal coordinates, the difficulty in connecting the placement of the poles with system performance and the necessity for full state feedback. The advantages include simplified system matrices and ease of system verification.

The difficulty of reconstructing 14 states from two inputs has been the major source of setbacks in developing a full state feedback controller. The standard method of forming Q_{xx} completely failed in this application. The "updated" solution developed in Chapter V yields favorable results but it still has drawbacks. The major one is that it reduces the 14th order feedback system to a 6th order feedback system. Obviously, one can only consider this a "full state feedback" controller if only six states are important. Otherwise, if more states need to be controlled, the original model may be expanded to include 20 modes which will then be reduced through the same procedure discussed in Chapter V. Whatever the case, when fewer states are fed back than those modeled, the question of robustness of the optimal controller becomes very important.

Momentum wheel desaturation using thrusters proved to be attainable without significant flexible interaction. The position offset can be reduced by several methods. These will be discussed in the next section. Again, the experimental and analytical results are in close agreement.

Thruster slew maneuvers also proved to be beneficial. The same control law implemented with thrusters gave faster slew times and almost no flexible interaction around the nominal position. Pressure differentials between full flow and static conditions required the use of an average torque level. These pressure variations can be reduced by inserting a reserve tank on the low pressure side of the regulator to provide a buffer area where pressure fluctuations could be absorbed. A pressure transducer could be added to the system to provide pressure reading feedback to the controller which would continuously update the thruster torque.

A. RECOMMENDATIONS FOR FURTHER STUDY

Recently, the FSS lab has received the System/Observer/Controller Identification (SOCI) Toolbox for Matlab developed by Dr. Jer-Nan Juang, Dr. Lucas G. Horta and Dr. Minh Phan. This toolbox allows one to obtain minimum order system matrices, observer and controller gains, and natural frequencies and damping based on input and output data obtained from an experimental run. The programs in the toolbox give results in the system modal model form. When the data is converted from Matrix$_X$ data files on the VAX to Matlab data files, system verification can be accomplished and analytical values for damping and observer/controller gains will be available.

The system modal model seems very attractive at first. However, as stated previously, it was developed to implement the eigenstructure assignment routines which require full state feedback. Without an accurate, estimator the feedback control is poor. Unfortunately, the estimator solution obtained in Chapter V does not translate well to the system modal model. The additional matrix transformation of the states does not allow raw position and velocity data to be fed back. As a result, the estimator is much slower in reconstructing the states which significantly degrades the feedback controller. When the overhead Vision

Server system is installed, more states will be available and the eigenstructure estimator should be reevaluated.

Chapter V outlined a different approach to establishing the estimator state weighting matrix. This is only a preliminary investigation and deserves more study. One possibility is to perform a Singular Value Decomposition to discover its minimum value. A study of the robustness of the reduced order estimator should be conducted to determine the stability limits.

Research of momentum dumping using thrusters has just begun. Different algorithms are available and should be implemented. The position offset could be reduced by pre-positioning the central body so that it would return to its nominal position as a result of the desaturation firing. Also, the momentum dump could be accomplished by a series of shorter pulses. This would increase the overall desaturation period but would decrease the maximum position offset. Care should be taken to ensure the frequency of the pulses does not resonate the flexible appendage. Thruster slew maneuvers are also in their infancy on the FSS. The bang-bang firing scheme can be modified to include nominal position control with the momentum wheel, and slewing with the thrusters. Again, robustness investigations should be made to determine stability margins.

The connection of the hub to the overhead I-Beam should be redesigned to provide a more stable base. Presently, it is too flimsy causing the center of rotation to change slightly during a slew. Also, all electrical connections should be accomplished through a commutator on the spin axis to eliminate the influenced of cabling on the central body. The air needed to float the experiment and to support the air bearing may be provided from the thruster air system by regulating down to 60 psi.

Future research is planned to include robotic control of a rigid arm. Motors will be mounted on the shoulder, elbow and wrist of the arm to manipulate it. This research will expand into robotic manipulation of a flexible arm.

APPENDIX A

An overriding concern in the implementation of the actual slew maneuvers has been the action of the momentum wheel motor assembly. Since the motor is able to spin the momentum wheel at very high speeds before it burns itself out and since the accelerations on the wheel can also be very high, great care was taken to ensure that the motor would not spin out of control. The wheel was manufactured at the Naval Postgraduate School and was statically balanced. However, the school has no facilities for dynamic balancing. Consequently, it was not known whether there would be significant wobbling at high rotation rates from some dynamic imbalance. Additionally, the PMI motor controller has no function for gradual speed changes. It simply responds to a commanded voltage and orders the motor to the corresponding speed with maximum acceleration. Obviously, this situation was unacceptable.

As a result, a method was required to implement a gradual acceleration and deceleration of the momentum wheel which would act as both a safeguard against over-torquing the motor and a means of reducing the disturbance to the system during spin-up/spin-down periods. A nominal wheel speed was set at 1000 rpm to establish a pitch-bias momentum control system. The nominal wheel speed was selected because it was a mid-range speed on the motor controller and because the motor operated smoothest in the region around 1000 rpm.

Another concern which motivated a start-up safeguard was related to the AC-100. When a session with the AC-100 was ended, it would store whatever voltage was last commanded on its Digital-to-Analogue converters. Consequently, when the next session was started, the last voltage (speed) command to the motor controller from the previous session would be sent to the wheel as an initial state. A method for zeroing out the actuator command was needed to ensure the momentum wheel would not be torqued before the user could stop it.

Fortunately, the System Build utility in Matrix$_X$ was capable of implementing these requirements. Figure A1 is the System Build block diagram of the safety control scheme used in every actual slew maneuver performed on the table. This scheme is the underlying controller that remains in effect except when an active controller is selected. It has four modes of operation. The first is the "spin-up" mode which orders the wheel to 1000 rpm at an acceleration of 10 rpm/sec. The "spin-down" modes orders the wheel to 0 rpm at the same acceleration as the spin-up modes. These accelerations can be changed using a manual increment switch which will be explained later. The third mode is the "control" mode which bypasses all of the limiters on the wheel acceleration so that the feedback control system has maximum response. The fourth mode is the "no effect" mode which maintains the current wheel speed. This is the default mode at start-up and allows the user to "do nothing" if events get out of control.

The following is a block-by-block description of the safety control scheme. Refer to Figure A1 for block numbers. They are located in the upper right corner of each block in the figure.

1. Blocks 1, 6, 13, 28, 33 and 43

Theses blocks filter and convert the tach, rvdt and rate gyro voltages to rpm, degrees and radians/sec respectively. The filters for the rate gyro and rvdt are stored in the variable RFILTC and the filter for the tach is in TFILTC.

2. Blocks 35 and 99

These blocks take the derivative of the rvdt signal and convert it to degrees/second to give analytical body rate.

3. Blocks 18 and 19

These blocks form the tolerance section. If the tach speed is less than or equal to two rpm, the controller will order zero wheel speed. Otherwise, it sends the rpm command from block 11.

4. Block 27

This is the wheel enable block. If the wheel is enabled, it will pass the rpm command from block 11. If not, it will pass the rpm command from block 18. Consequently, if the wheel is disabled and within two rpm of zero, it will remain at zero until the wheel is enabled. Conversely, if the wheel is disabled while spinning , it will not go to zero unless it is within two rpm of zero.

5. Block 8

If "control" mode is selected in block 10, the rpm command from block 21 will be sent to block 2. Otherwise, the rpm from block 27 will pass. This allows unincremented speed commands to be sent to the wheel during slew maneuvers for the fastest response. When not in "control" mode, wheel commands will be incremented for safety purposes.

6. Block 2

Converts rpm to voltage for commanding the motor.

7. Blocks 9, 11, 21, 31, 90, 91 and 92

These blocks are the guts of the safety control system.

a. Block 21

This block orders speed and increment commands depending on which mode the user chooses.

"Spin-up" mode

Sends a wheel speed command of 1000 rpm to block 9 and an increment of 10 rpm/sec to block 92.

"Control" mode

Sends the wheel speed command from the feedback control system to block 88.

"Spin-down" mode

Sends commanded wheel speed of 0 rpm to block 9 and an increment of 10 rpm/sec to block 92.

"No effect" mode

Sends 0 increment to block 9 which acts to hold the commanded wheel speed where it is.

b. Block 91

Sends the absolute value of the rpm error from block 9 to block 92.

c. Block 92

This block sets a fine increment of 1 rpm/sec if the wheel speed is within 20 rpm of commanded wheel speed.

d. Block 31

This is the automatic/manual speed increment selection block. It allows the user to change the increment while the simulation is running. When in manual mode, it multiplies the 0.1 set in block 21 by the number selected. For current operation, the sample interval is 0.01 which means there are 100 samples per second. If the speed is incremented at every sample time, there will be 100 times 0.1 rpm increase every second. It is important to remember that a change in the sample interval will change the numerical value of the speed increment. This block is initially set to automatic and must be actively changed to manual if desired.

e. Block 9

Subtracts the tach speed from the commanded speed and outputs rpm error to block 91 and block 11.

f. Blocks 11 and 90

This block performs the incrementation. If the rpm error is negative (spin-down), the increment is the negative of the value from block 31. Therefore, it is subtracted from the current tach speed and set as a command to the motor. The block11-block90 combination acts as a storage register which saves the current wheel speed. This allows the increment to be added or subtracted (depending on block 9 output) to the current wheel speed and sent out as a wheel command. The higher the increment, the faster the wheel responds. When the "control" mode is on, the wheel speed is fed back with no increment so that it tracks the commanded speed. This makes for smooth transitions between the "control" mode and other modes.

g. Block 10

This block is connected to the interactive animator. When a mode is selected, it is represented by a -1, 0, 1 or 2. This is the number that the other blocks read when a mode is selected.

8. Block 8

Converts the torque command from the feedback controller to acceleration by dividing out the wheel inertia.

9. Block 3

Integrates the command acceleration to give wheel speed in radians/second.

10. Block 16

Converts radians/second to rpm.

11. Blocks 83 and 84

These blocks force the controller to set as a wheel command the current tach speed when "control" mode is off. This allows for smooth switching to "control" mode so that no spikes are artificially created. These blocks also allow the user to reset the control wheel command to tach speed when the wheel speed gets high.

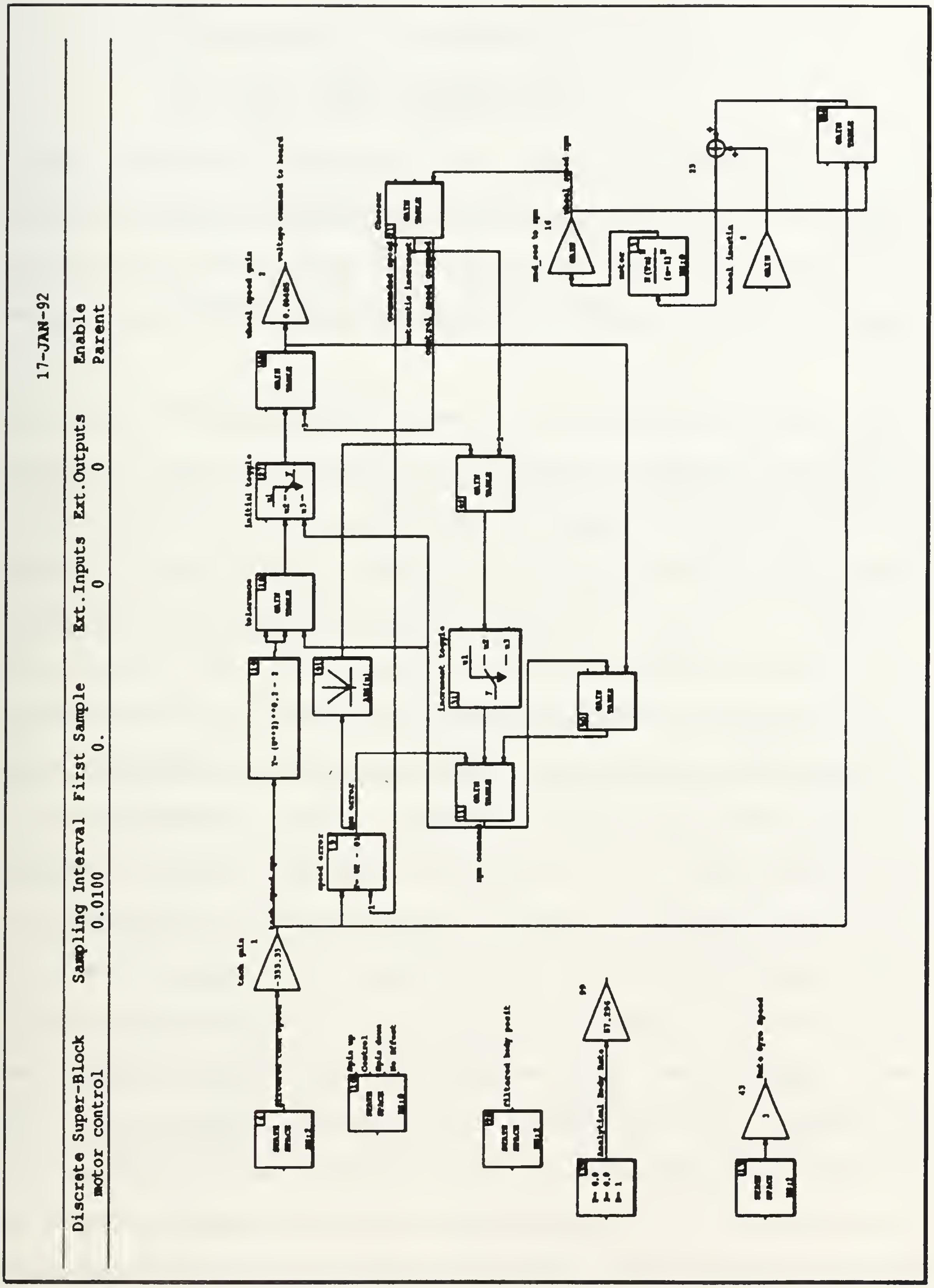
Discrete Super-Block
motor control
Sampling Interval
0.0100
First Sample
0.
Ext.Inputs
0
Ext.Outputs
0
Enable
Parent
17-JAN-92
tach gain
-333.33
wheel speed gain
0.00488
voltage command to board
initial toggle
tolerance
increment toggle
speed error
ABS(u)
GAIN
GAIN
GAIN
57.296

Figure A1. Motor Controller Block Diagram

APPENDIX B

Several decisions must be made in designing the thruster system. Considerations such as minimum and maximum thrust levels and the length of the moment arm are key to determining the operating pressure of the system. Table B1 contains the physical parameters around which the system must be built.

For simplicity, isentropic flow is assumed. The operating fluid is either N_2 or air, both with a polytropic constant of 1.4. The mass flow rate for hydrazine of 0.0224 lbm/sec is assumed for air and N_2. For an initial try, perfect expansion is assumed so that the exit pressure, P_e, is the same as ambient pressure, P_a, 14.7 psig. The problem is to find the exit area, A_e, and the thrust, F, for chamber pressures, P_c, ranging from zero to 250 psig. The results are shown in Table B2. The torque produced by each thruster should be less than 0.7 N-m. This is an approximation based on the Bang-Bang results where a 0.6 N-m thrust caused unacceptable oscillations. If the solenoid placement is restricted so that no piece is allowed to protrude from the hub, the longest moment arm achievable is 14 inches. Using these numbers and converting to MKS units yields 0.6609 N-m torque at 200 psig chamber pressure. To achieve perfect expansion, a nozzle is required to increase the exit diameter from 0.045 inches to 0.0683 inches. Since building this nozzle seems hardly worthwhile, an investigation of the thrust obtained without a nozzle is reasonable. The exit diameter is now 0.045 inches (the same as the throat diameter) which gives a torque of 0.6010 N-m. If a larger torque is required the chamber pressure can be raised. For now, 0.6 N-m is acceptable as an upper limit so that a nozzle need not be built.

The governing equations for determining the thrust are

$$\frac{A_e}{A_{th}} = \frac{1}{M}\left[\left(1 + \frac{(\gamma - 1)}{2}M^2\right)\frac{2}{\gamma + 1}\right]^{\frac{\gamma + 1}{2(\gamma - 1)}} \tag{B1}$$

$$P_e = P_c\left[1 + \frac{\gamma - 1}{2}M^2\right]^{\frac{\gamma}{\gamma - 1}} \tag{B2}$$

$$F = \Gamma P_c A_{th}\left[\frac{2\gamma}{\gamma - 1}\left(1 - \left(\frac{P_e}{P_c}\right)^{\frac{\gamma - 1}{\gamma}}\right)\right]^{\frac{1}{2}} + (P_e - P_a)A_{ex} \tag{B3}$$

$$\Gamma = \gamma^{\frac{1}{2}}\left(\frac{2}{\gamma + 1}\right)^{\frac{\gamma + 1}{2(\gamma - 1)}} \tag{B4}$$

where F is thrust. First the Mach number, M, is determined by iterating Equation (B1). Then the exit pressure is calculated through Equation (B2). Finally, the thrust is given by Equation (B3) where Γ is a function of the polytropic constant in the form of Equation (B4).

Table B1. Physical Parameters

Description	Symbol	Value
Hub Radius	R_h	15 inches
Throat Diameter	D_{th}	0.045 inches
Exit Diameter	D_{ex}	0.045 inches
Solenoid Length	L	1.627 inches
Polytropic Constant	γ	1.4
Ambient Pressure	P_a	14.7 psig
Mass Flow Rate	ρ	0.0224 lbm/sec

Table B2. Thrust Values for Various Chamber Pressures

Chamber Pressure (psig)	Thrust (lbf)
155	0.2967
160	0.3047
165	0.3133
170	0.3221
175	0.3313
180	0.3407
185	0.3502
190	0.3600
195	0.3699
200	0.3799
205	0.3901
210	0.4003
215	0.4106
220	0.4210
225	0.4315
230	0.4420
235	0.4526
240	0.4633
245	0.4740
250	0.4847

APPENDIX C

This program is provided to show the numerical results of the Eigenstructure assignment method and the formation of the system modal model.

Program Matrix Formations

THIS PROGRAM SOLVES THE SYSTEM EIGENVALUE PROBLEM FOR THE FLEXIBLE SPACECRAFT SIMULATOR. IT RETURNS THE SYSTEM EIGENVALUES AND MODAL MATRIX. PHI REPRESENTS THE MODAL MATRIX SO THAT

$$PHI'*M*PHI = I$$

AND

$$PHI'*K*PHI = [\omega^2]$$

THE EIGENVALUE PROBLEM IS STATED SO THAT

$$\omega_i^2*M*PHI_i = K*PHI_i$$

THE SYSTEM NATURAL FREQUENCIES ARE GIVEN IN THE MATRIX NF WITH THE FREQUENCIES LYING ALONG THE DIAGONAL IN ASCENDING ORDER.

```
phi2=[];natfreqs=[];
coupl=[-1.9891 1.2269 0.4363 -0.1395 0.2193 0.0106]';
freqs=[0.8756 2.6375 15.4758 26.9839 43.0998 80.5634]';
I=eye(7);zs=0*I;zr=0*[1:7];zc=0*[1:6]';
D=coupl'*coupl;Izzo1=10.49;Izzo2=Izzo1-D;
DS=coupl*coupl';zeta=0.004;
omega=diag([freqs]);omega2=omega*omega;
omegac=2*zeta*DS*(-omega);omega2c=DS*(-omega2);
DW=2*zeta*coupl'*omega;DW2=coupl'*omega2;
A=[zs I;zr zr;zc -omega2 zc -2*zeta*omega];
A1=[zs zs;0 DW2 0 DW;zc omega2c zc omegac]/Izzo2;
B=[zr';1;zc]/Izzo2;
B1=[zr';0;-coupl]/Izzo2;
Asys=A+A1;
Bsys=B+B1;
M=[Izzo1 coupl';coupl eye(6)];
K=[0 zc';zc omega2];
C=[0 zc';zc 2*zeta*omega];
[phi1,lambda]=eig(K,M);
F=phi1'*M*phi1;
[m,m]=size(F);
for i=1:m,
  for j=1:m,
    F1(i,j)=0;
  end
  F1(i,i)=F(i,i);
end
```

```
F=F1;
phi=phi1*inv(sqrt(F));
phit=[];;
lam=diag(lambda);
for i=1:m,
 k=i+1;
  for j=k:m,
   if lam(i)>lam(j)
      lam1=lam(i);
      phit=phi(:,i);
      lam(i)=lam(j);
      phi(:,i)=phi(:,j);
      lam(j)=lam1;
      phi(:,j)=phit;
   else
   end
 end
end
lambda=diag([lam]);
natfreqs=sqrt(lambda)/(2*pi);
checkM=phi'*M*phi;checkK=phi'*K*phi;
disp('phi = ')
disp(phi)
disp('eigenvalues = ')
disp(lambda)
disp('natural frequencies = ')
disp(natfreqs)
```

Program Target Eigenvalues and Eigenvectors

THIS PROGRAM FORMS TARGET EIGENVALUES BY SETTING THE REAL PART EQUAL TO -1 AND THE IMAGINARY PART EQUAL TO ω^2. IT THEN FORMS THE SYSTEM A AND B MATRICES AND FORMS THE TARGET EIGENVECTORS FROM THE OPEN-LOOP EIGENVECTORS. IT RETURNS THE CONDITION OF THE TARGET EIGENVECTORS, THE GAINS REQUIRED TO ACHEIVE THE TARGET EIGENVALUES, AND THE REALIZED EIGENVECTORS AND EIGENVALUES.

```
k=0;
tgtev=[];T=[];
i=sqrt(-1);
for k=1:m,
  tgtev(k)= -0.1 + i*sqrt(lam(k));
  tgtev(1)= -0.1 + i*0.000001;
  tgtev(k+m)=conj(tgtev(k));
end
disp('target eigenvalues')
disp(tgtev')
TGTEV=diag([tgtev(1:m)]);
T=[eye(m) eye(m);TGTEV conj(TGTEV)];
ct=cond(T);
disp('condition of target eigenvectors')
disp(ct)
Asys1=[0*eye(m) eye(m);-lambda -2*zeta*sqrt(lambda)];
Bs1=phi'*[1 zeros(1,m-1)]';
```

```
Bsys1=[zeros(m,1);Bs1];
assign
[V1,e1]=eig(Asys1+Bsys1*G);
disp('Gains')
G1=real(G);
disp(G1)
disp('condition of new eigenvectors')
cv1=cond(V1);
disp(cv1)
disp('check eigenvalues')
e1=diag(e1);
disp(e1)
```

Program Assign

THIS PROGRAM IS CALLED BY TARGETEIG TO CALCULATE THE GAINS

```
[n,n]=size(Asys1); L=eye(n);
for k=1:n,
  L(k,k)=tgtev(k);
end;
Binv=pinv(Bsys1);
H=Binv*(T*L-Asys1*T);
psi=lyap(Asys1,-L,Bsys1*H);
G=H*inv(psi);
```

Results

```
phi =

    0.3088    0.2288   -0.2258   -0.0891   -0.0294    0.0462    0.0022
         0    1.2433   -0.4901   -0.1778   -0.0585    0.0919    0.0044
         0    0.0591    1.1379    0.1125    0.0364   -0.0569   -0.0027
         0    0.0005   -0.0039    1.0193    0.0191   -0.0231   -0.0010
         0   -0.0001    0.0004    0.0065   -1.0020    0.0105    0.0004
         0    0.0000   -0.0002   -0.0030   -0.0042   -1.0050   -0.0007
         0    0.0000   -0.0000   -0.0000   -0.0000    0.0002   -1.0000


eigenvalues =

   1.0e+03 *


         0         0         0         0         0         0         0
         0    0.0012         0         0         0         0         0
         0         0    0.0092         0         0         0         0
         0         0         0    0.2490         0         0         0
         0         0         0         0    0.7311         0         0
         0         0         0         0         0    1.8765         0
         0         0         0         0         0         0    6.4906
```

```
natural frequencies =

        0        0        0        0        0        0        0

        0   0.1750        0        0        0        0        0

        0        0   0.4826        0        0        0        0

        0        0        0   2.5114        0        0        0

        0        0        0        0   4.3034        0        0

        0        0        0        0        0   6.8944        0

        0        0        0        0        0        0  12.8222


target eigenvalues

  -0.1000 - 0.0000i

  -0.1000 - 1.0997i

  -0.1000 - 3.0324i

  -0.1000 -15.7797i

  -0.1000 -27.0393i

  -0.1000 -43.3187i

  -0.1000 -80.5644i

  -0.1000 + 0.0000i

  -0.1000 + 1.0997i

  -0.1000 + 3.0324i

  -0.1000 +15.7797i

  -0.1000 +27.0393i

  -0.1000 +43.3187i

  -0.1000 +80.5644i
```

```
condition of target eigenvectors

   8.0966e+07




Gains

  Columns 1 through 7

   -0.0327   -0.1886    0.3694    0.6278   -0.1214    2.3436   78.8764

  Columns 8 through 14

   -0.6596   -0.8271    0.7708    0.8269   -0.5555    3.1720  198.7334

condition of new eigenvectors

   6.2282e+07
```

```
check eigenvalues
  -0.1000 -80.5644i
  -0.1000 +80.5644i
  -0.1000 -43.3187i
  -0.1000 +43.3187i
  -0.1000 -27.0393i
  -0.1000 +27.0393i
  -0.1000 -15.7797i
  -0.1000 +15.7797i
  -0.1000 - 3.0324i
  -0.1000 + 3.0324i
  -0.1000 - 1.0997i
  -0.1000 - 0.0000i
  -0.1000 + 0.0000i
  -0.1000 + 1.0997i
```

```
Asys1 =


  1.0e+03 *


 Columns 1 through 7


        0         0         0         0         0         0         0
        0         0         0         0         0         0         0
        0         0         0         0         0         0         0
        0         0         0         0         0         0         0
        0         0         0         0         0         0         0
        0         0         0         0         0         0         0
        0         0         0         0         0         0         0
        0         0         0         0         0         0         0
        0   -0.0012         0         0         0         0         0
        0         0   -0.0092         0         0         0         0
        0         0         0   -0.2490         0         0         0
        0         0         0         0   -0.7311         0         0
        0         0         0         0         0   -1.8765         0
        0         0         0         0         0         0   -6.4906
```

```
Columns 8 through 14

   0.0010        0         0         0         0         0         0
        0   0.0010         0         0         0         0         0
        0        0    0.0010         0         0         0         0
        0        0         0    0.0010         0         0         0
        0        0         0         0    0.0010         0         0
        0        0         0         0         0    0.0010         0
        0        0         0         0         0         0    0.0010
        0        0         0         0         0         0         0
        0  -0.0000         0         0         0         0         0
        0        0   -0.0000         0         0         0         0
        0        0         0   -0.0001         0         0         0
        0        0         0         0   -0.0002         0         0
        0        0         0         0         0   -0.0003         0
        0        0         0         0         0         0   -0.0006
```

```
Bsys1 =

         0
         0
         0
         0
         0
         0
         0
    0.3088
    0.2288
   -0.2258
   -0.0891
   -0.0294
    0.0462
    0.0022
```

APPENDIX D

Verification of the modal frequencies for the system modal model is easily accomplished by randomly perturbing the rigid-flexible system and analyzing the spectrum of the acquired data. Figure C1 is the autocorrelation spectrum of the RVDT position information obtained from such a method. The peaks represent the modal frequencies. Notice the peak at zero representing the rigid body frequency.

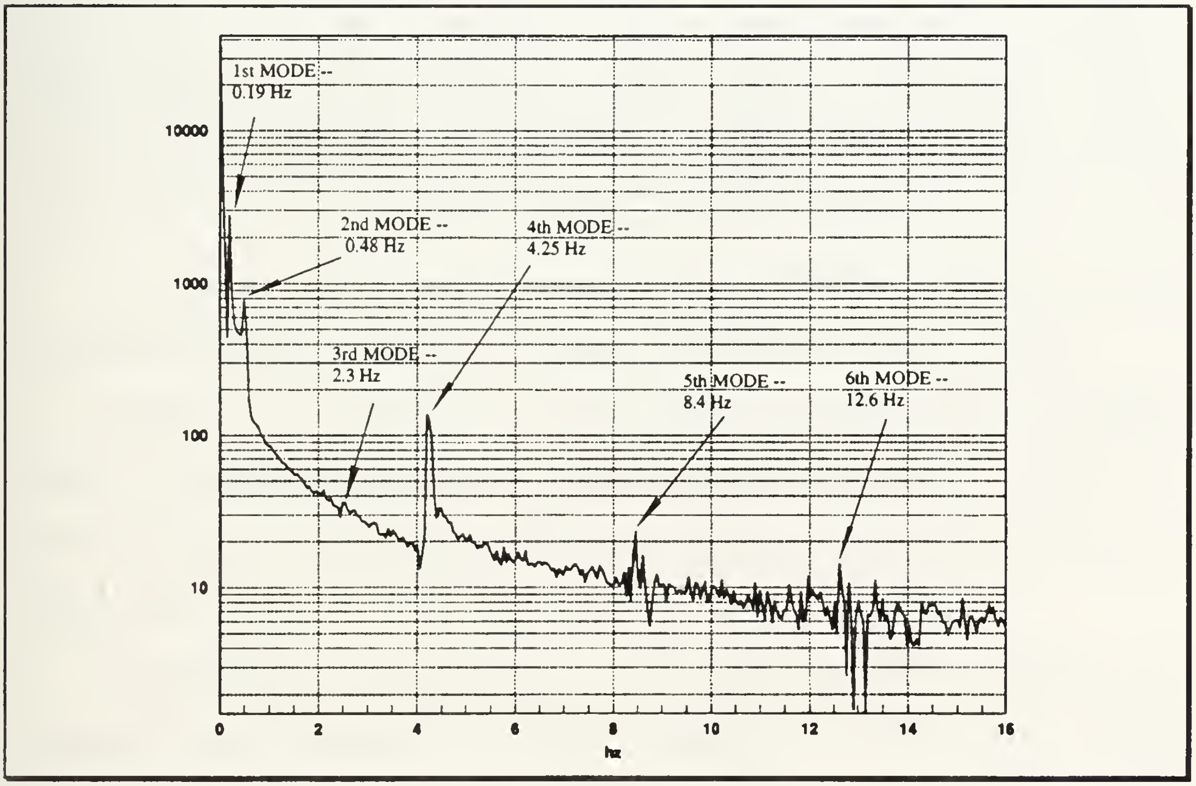

Figure C1. Modal Frequency Verification

The analytical and experimental frequencies are given in Table C1 for comparison.

Table C1. System Modal Frequencies

Mode	Analytical (Hz)	Experimental (Hz)	Percent Error (%)
1	0.175	0.19	8.6
2	0.483	0.480	0.6
3	2.51	2.30	8.4
4	4.30	4.25	1.2
5	6.89	8.40	21.9
6	12.89	12.6	2.3

REFERENCES

1. Juang, Jer-Nan, Horta, L.G., and Robert Shaw, H.H., "A Slewing Control Experiment for Flexible Structures," Journal of Guidance, Control and Dynamics, Vol. 9, NO. 5, Sept.-Oct., 1986, PP. 599-607.

2. Junkins, J., Rahman, Z., and Bang, H., "Near-Minimum-Time Maneuvers of Flexible Vehicles: A Liapunov Control Law Design Method," Mechanics and Control of Large Flexible Structures, Progress in Astronautics and Aeronautics, Vol. 129, 1990, PP. 565-593.

3. Oakley, C.M. and Canon, R.H., "Theory and Experiments in Selecting Mode Shapes for Two-Link Flexible Manipulators," Proceedings of First International Symposium on Experimental Robotics, Montreal, Canada, June 1989.

4. Watkins Jr., R.J., "The Attitude Control of Flexible Spacecraft," Naval Postgraduate School Thesis, B.N. Agrawal, Advisor, June, 1991, PP 6-10.

5. Singh, S.K., Gran, R., and Agrawal, B.N., "Comparison of Different Attitude Control Schemes for Large Communications Satellites," Proceedings of AIAA Guidance, Navigation, and Control Conference, Monterey, California, August 1987.

6. Agrawal, B.N., and Watkins Jr., R.J., "Experimental Verification of Attitude Control Techniques for Flexible Spacecraft," 42nd Congress of the International Astronautical Federation, Montreal, Canada, October 5-11, 1991.

7. Kwakernaak, H., Sivan, R., "Linear Optimal Control Systems," Wiley-Interscience, New York, 1972.

8. Junkins, J., Turner, J., "Optimal Spacecraft Rotational Maneuvers," Elsevier Science Publishers B.V., Amsterdam, 1986.

INITIAL DISTRIBUTION LIST

1.	Defense Technical Information Center Cameron Station Alexandria, Virginia 22304-6145	2
2.	Library, Code 52 Naval Postgraduate School Monterey, California 93943-5002	2
3.	Chairman, Code AA Department of Aeronautics and Astronautics Naval Postgraduate School Monterey, California 93943	1
4.	Chairman, Code SP Department of Aeronautics and Astronautics Naval Postgraduate School Monterey, California 93943	1
5.	Professor Brij N. Agrawal, Code AA/Ag Department of Aeronautics and Astronautics Naval Postgraduate School Monterey, California 93943	2
6.	Professor I. Michael Ross, Code AA/Ro Department of Aeronautics and Astronautics Naval Postgraduate School Monterey, California 93943	1
7.	LT Jeffrey A. Hailey 1296 Mayfield Circle Suisun City, California 94585	2

816-655

DUDLEY KNOX LIBRARY
NAVAL POSTGRADUATE SCHOOL
MONTEREY CA 93943-5101

GAYLORD S

AMERICAN BINDERY
2
4-94

DUDLEY KNOX LIBRARY
3 2768 00018960 9